Final work : Computational study of the unsteady pressure around a 3D circular cylinder undergoing forced motion

Auteur : Lomele, Martina
Promoteur(s) : Dimitriadis, Grigorios
Faculté : Faculté des Sciences appliquées
Diplôme : Master en ingénieur civil en aérospatiale, à finalité spécialisée en "turbomachinery aeromechanics (THRUST)"
Année académique : 2019-2020
URI/URL : http://hdl.handle.net/2268.2/10375

University of Liège
Faculty of Applied Sciences

Computational study of the unsteady pressure around a 3D circular cylinder undergoing forced motion

Master thesis submitted in partial fulfillment of the requirements for the degree of Master in Aerospace Engineering, professional focus in Turbomachinery Aeromechanics (THRUST)

By Martina Lomele

Advisors: Prof. R. E. Kielb (Duke University)
Prof. G. Dimitriadis (ULiège)
Jury: Prof. T. Andrianne (ULiège)

Academic year 2019-2020

Acknowledgements

I would first like to express my deep thankfulness to Dr. Robert Kielb, who offered me the possibility to pursue this thesis, welcoming me in the Aeroelasticity Department of Duke University. He patiently guided me during this project, stimulating me with his suggestions and his wide knowledge.

Moreover, this project would not have been realizable without the help and the supervision of Dr. Grigorios Dimitriadis and Dr. Thomas Andrianne from the University of Liège, who, even if remotely, followed my work and who I would like to thank.

I further extend my personal gratitude to all the people with whom I had the pleasure to work at Duke University: Dr. Kenneth Hall, Dr. Earl Dowell and Dr. Lawrence Virgin, who supported the experimental part of this project, as well as my group-members, Bas, Oier, Jason and Ricky. Among them, Bas and Oier deserve a special mention, being not only my fellow students, who helped me in several occasions, but primarily my friends and companions in adventure.

I would then like to thank all my friends and professors from the THRUST program, as well as my friends from all over the world; this goal would not have been reached without them.

Finally, my thoughts go to the pillars of my life: my parents, Flaviano and Caterina, my siblings, Giovanni and Cristina, my aunt, Grazia, and my best friend, Simonetta. I would not be here without them and without their support, and there are no words capable to express the love and the gratitude I feel for them. Even if physically far from each other, I know they will always be with me.

Then, my last words go to one special person, my dear friend Yann. Since I met him, he has shown to me his constant help during both my studies and my private life. He has always encouraged me to go beyond my limits, deeply trying to make me stronger. I could not have made it without him and there is not a better way to express what I feel because of that than two simple words: thank you.

Abstract

The study of viscous flows around bluff bodies is one of the main and more classical topic in the engineering fields. It represents a challenging research area in constant development over the years.
Nowadays, thanks to the improvement of numerical techniques capable to correctly capture the dynamic of the flow reaching a solid body, CFD simulations have become a widely used tool to study the flow around circular cylinders at both low and high Reynolds numbers. However, a validation of the numerical codes based on experimental data is necessary.

The aim of this project is to provide a first analysis of the unsteady pressure evolution around a circular cylinder forced to oscillate with certain frequencies and amplitudes, which allow the body to reach the lock-in condition.

In the first place, it was supposed to be conducted as a fully experimental project, based at Duke University. However, due to the impact of the COVID-19 pandemic, the ongoing experimental work had to prematurely end and a computational project was preferred instead.

Both the experimental and the computational results are presented throughout this thesis. Nevertheless, while, in the experimental part, only the test rig design could be completed, the computational part reached the prefixed target.
After a first analysis of the best numerical model able to accurately describe the flow around a 3D circular cylinder at high Reynolds numbers, validated using some empirical data obtained during a VIV experiment conducted in the University of Liège wind tunnel, the study of the unsteady pressure around the modeled body is performed.

Main focus is given to the variation of the unsteady lift and pressure coefficient while the cylinder is forced to oscillate at different frequencies and amplitudes transversely to the flow at $Re = 2.9 \cdot 10^4$. The effects of the variation in the imposed motion characteristics (frequency and amplitude) are discussed showing the region where the lock-in condition is reached, as well as its impact on the time-varying lift and pressure coefficient.

Finally, a comparison between the 3D results of this study and the 2D ones, obtained by Oier Jauntsarats Sacedo [37], is presented and the main similarities highlighted.

All the computational experiments are conducted in Ansys Fluent 2019 R2 by means of the Duke University Scientific Linux 6.7 Cluster, using 60 cores.

Contents

List of Figures

List of Tables

Nomenclature

Acronyms

(U)RANS	(Unsteady) Reynolds-Averaged Navier-Stokes Equations
CAD	Computer-Aided Design
CFD	Computational Fluid Dynamics
DAQ	Data Acquisition System
DC	Direct Current
DDES	Delayed Detached Eddy Simulation
DES	Detached Eddy Simulation
DNS	Direct Numerical Solution
FDM	Finite Difference Method
FEM	Finite Element Method
FFT	Fast Fourier Transform
FS	Full Scale
FVM	Finite Volume Method
LES	Large Eddy Simulation
OD	Outer Diameter
PISO	Pressure-Implicit with Splitting of Operators
PVC	Polyvinyl Chloride
RPS	Rotations per second
SAS	Scale-Adaptive Simulation
SIMPLEC	Semi-Implicit Method for Pressure Linked Equations-Consistent
SIMPLER	Semi-Implicit Method for Pressure Linked Equations-Revised
SIMPLE	Semi-Implicit Method for Pressure Linked Equations
SRS	Scale-Resolving Simulation
SST	Shear Stress Transport
UDF	User Defined Function
VIV	Vortex Induced Vibrations

Symbols

$\bar{\tau}_{ij}$	Mean viscous stress tensor	[N/m^2]
$\bar{C}_D$	Mean drag coefficient	[-]
$\bar{U}_i$	Time-average velocity in the i-direction	[m/s]
β	Constant used in the $k-\omega$ SST turbulence model	[-]
β^*	Constant used in the $k-\omega$ SST turbulence model	[-]
β_1	Constant used in the $k-\omega$ SST turbulence model	[-]
β_2	Constant used in the $k-\omega$ SST turbulence model	[-]
$\Delta_{\max}$	Grid spacing	[m]
δ_{ij}	Kronecker delta	[-]
γ	Intermittency coefficient	[-]
κ	Von Kármán constant	[-]
λ_2	Second negative eigenvalue of the velocity-gradient tensor	[1/s]
μ	Dynamic viscosity	[Pa·s]
ν	Kinematic viscosity	[m^2/s]
ν_t	Turbulent eddy viscosity	[m^2/s]
Ω	Antisymmetric part of the velocity gradient tensor	[1/s]
ω	Dissipation of the turbulent kinetic energy into thermal energy	[m^2/s^3]
Ω_{ij}	Vorticity magnitude	[1/s]
ϕ	Scalar quantity	[-]
ϕ_L	Phase difference between the cylinder's motion and the lift coefficient	[^{o}]
Ψ	Symmetric part of the velocity gradient tensor	[1/s]
ρ	Flow density	[kg/m^3]
ρ_∞	Flow density in the free-stream	[kg/m^3]
$\sigma_{\theta t}$	Constant used in the Transition SST turbulence model	[-]
σ_k	Constant used in the $k-\omega$ SST turbulence model	[-]
τ_{ij}	Viscous stress tensor	[N/m^2]
θ	Angular coordinate over the mid-span section of the cylinder	[^{o}]
θ_{sep}	Angle of separation	[^{o}]
$\tilde{Re}_{\theta t}$	Transition momentum thickness Reynolds number	[-]

ε	Correction factor	[-]
ζ	Structural damping	[-]
A	Amplitude of vibrations	[m]
A_x	Amplitude of oscillations in the in-flow direction	[m]
A_y	Amplitude of oscillations in the cross-flow direction	[m]
c	Speed of sound	[m/s]
C_D	Drag coefficient	[-]
C_L	Lift coefficient	[-]
C_p	Pressure coefficient	[-]
$c_{\theta t}$	Constant used in the Transition SST turbulence model	[-]
C_{a1}	Constant used in the Transition SST turbulence model	[-]
C_{a2}	Constant used in the Transition SST turbulence model	[-]
C_{e1}	Constant used in the Transition SST turbulence model	[-]
C_{e2}	Constant used in the Transition SST turbulence model	[-]
$C_{L_{rms}}$	Root-mean-square value of the lift coefficient	[-]
C_{pb}	Base pressure coefficient	[-]
D	Cylinder diameter	[m]
dt	Time-step size	[s]
f	Forcing frequency	[Hz]
F_D	Drag force	[N]
F_L	Lift force	[N]
f_n	Natural frequency	[Hz]
f_s	Vortex shedding frequency	[Hz]
f_x	Frequency of oscillation in the in-flow direction	[Hz]
f_y	Frequency of oscillation in the cross-flow direction	[Hz]
F_{length}	Empirical correlation controlling the transition region length	[-]
f_{osc}	Frequency of forced oscillations of the cylinder	[Hz]
f_{vs}^0	Frequency of vortex shedding	[Hz]
k	Turbulent kinetic energy	[m^2/s^2]
L_t	Turbulent length scale	[m]

L_z	Spanwise cylinder length	[m]
L_{VK}	Von Kármán scale length	[m]
M	Mach number	[-]
m	Mass of the oscillating body	[kg]
n	Time level	[-]
N_T	Number of stable vortex shedding periods	[-]
N_z	Number of elements in the z-direction	[-]
P	Motor power	[W]
p	Static pressure	[Pa]
p_∞	Flow static pressure in the free-stream	[Pa]
R_{ij}	Reynolds stress tensor	[N/m^2]
Re	Reynolds number	[-]
$Re_{\theta c}$	Critical Reynolds number at which the intermittency increases	[-]
S	Strain rate magnitude	[1/s]
S_G	Skop-Griffin number	[-]
St	Strouhal number	[-]
T	Torque	[N·m]
T_e	Period of oscillation of the cylinder	[s]
T_v	Period of vortex shedding	[s]
U_∞	Free-stream velocity	[m/s]
u_i'	Fluctuation of the velocity around its mean value	[m/s]
U_r	Reduced velocity	[-]
U_x	Velocity component in the x-direction	[m/s]
U_y	Velocity component in the y-direction	[m/s]
V	Voltage	[V]
y	Wall distance	[m]
$y(t)$	Time signal of the motion of the cylinder	[m]
y^+	y-plus value	[-]
$(\sigma_\omega)_1$	Constant used in the $k-\omega$ SST turbulence model	[-]
$(\sigma_\omega)_2$	Constant used in the $k-\omega$ SST turbulence model	[-]

$(\sigma_k)_1$	Constant used in the $k-\omega$ SST turbulence model	[-]
$(\sigma_k)_2$	Constant used in the $k-\omega$ SST turbulence model	[-]
u_i	Velocity in the i-direction of a Cartesian coordinate system	[m/s]
u_j	Velocity in the j-direction of a Cartesian coordinate system	[m/s]
u_k	Velocity in the k-direction of a Cartesian coordinate system	[m/s]
x	Coordinate in the streamwise direction	[m]
y	Coordinate perpendicular to the streamwise and spanwise direction	[m]
z	Coordinate in the spanwise direction	[m]

Chapter 1

Introduction

The study of the flow around bluff bodies has always been one of the main interests in the engineering field. If, on the one hand, the aerodynamics of a flow past a bluff body is now fully known, on the other hand, some interesting aeroleastic phenomena still under study appear when the body is subjected to in incoming airflow.
Cables, wires, chimneys, towers are just few examples of bluff bodies generally subjected to an incoming wind flow. Their particular cylindrical shape makes them unsuitable to deal with the flow around them and their flexibility, due to their large dimensions, plays certainly an important role in the life of these structures when subjected to a wind flow.

The main goal of this thesis will be to simulate the flow around a cylindrical body focusing on one particular aeroelastic phenomenon, the Vortex Induced Vibration phenomenon, as well as on the cylinder's forced response.

In this chapter, firstly, an overview regarding the bluff bodies aerodynamics for static cylinders will be presented as an introduction to the complex topic of a cylinder oscillating aeroelastically or following forced vibrations, discussed in section 1.2 and section 1.3, respectively.
Finally, the main objectives of the present study and the contents of the various chapters of this thesis will be summarized in section 1.4.

1.1 Bluff bodies aerodynamics

In aerodynamics, a bluff body is defined as a body with the length in the direction of the flow close or equal to the one in the direction perpendicular to the flow. The main example of bluff body is the circular cylinder, the object of this project. A streamlined body, such as an airfoil, can also behave as a bluff body at high angles of attack.

Several studies have been conducted by previous researchers with the purpose of analyzing the flow past a bluff body. The main contributes are certainly given by the works of Strouhal [59], Williamson [63] and Roshko [55], whose key results will be summarized in the following sections. Principal focus was given to case of static cylinders, deeply studied by several researchers. In particular, the experimental results obtained by Norberg [49] are often used as a benchmark to validate computational models. Moreover, the aeroelastic phenomena to which the body invested by a fluid flow is subjected are fundamental in this field. Anagnostopoulos [1] deeply analyzed this case both experimentally and computationally, as well as Blevins [9] and Feng [24].

The main feature of the flow over a bluff body is the separation of the flow at a certain location around the body, which leads to the creation of a region of disturbed flow called the wake, where two- and three-dimensional unsteady flow structures progressively increase. The flow separation occurs in the *boundary layer*, a region very close to the body characterized by high velocity gradients due to the impact of the viscous effects,

which assume primary importance in this area. Indeed, the velocity goes gradually from the condition of rest, due to the presence of the body's wall, to the free-stream value at the boundary layer upper edge.
The separation point on the cylinder is not located always at the same position, but it depends on the type of *boundary layer* and, consequentially, on the Reynolds number of the case studied. The latter is one of the key parameters regulating the flow separation and the formation of the wake of a flow reaching a bluff body.

1.1.1 The Reynold number

The Reynolds number [54] is defined as

$$Re = \frac{U_\infty \cdot L}{\nu} \tag{1.1}$$

where ν[1] is the kinematic viscosity of the fluid reaching the solid body, U_∞ is the free-stream velocity and L is the reference length of the system (the cylinder's diameter, in this study).
It represents a key parameter in fluid dynamics as it is a measure of the ratio between inertial and viscous terms.
For the case of a cylinder at very low Reynolds numbers ($Re < 5$), no separation of the flow occurs; afterwards, increasing the value of Re up to 40, a first pair of two counter-rotating vortices appears, the so-called Von Kármán vortices. At $Re > 40$, these vortices are shed at a regular frequency forming the Von Kármán vortex street; they are indeed gradually formed and then transported downstream, defining the wake region, as shown in Figure 1.1. In this Reynolds range, the flow is defined as laminar.

Figure 1.1: Example of a flow past a circular cylinder: formation of the Von Kármán vortex street at $Re = 140$ [61]

[1]The kinematic viscosity can be found as $\nu = \frac{\mu}{\rho}$, with μ being the dynamic viscosity of the considered fluid and ρ its density.

When reaching $Re \simeq [150, 300]$, the transition to turbulence occurs and the inertia forces start taking control of the system; then, in the range $300 < Re < 10^7$, the vortex shedding phenomenon is altered by small scale turbulent structures. In particular, the transition from laminar to turbulent regime is completed for $3 \cdot 10^5 < Re < 3.5 \cdot 10^6$; indeed, a very disorganized and narrow wake appears.
Finally, for higher values of the Reynolds number, the turbulent vortex shedding is re-established.

Figure 1.2 summarizes the different flow regimes encountered in the case of a flow reaching a circular cylinder when varying the Reynolds number. In this study, a Reynolds number of $\simeq 10^4$ is considered, hence a laminar boundary layer and a fully turbulent vortex street are expected.

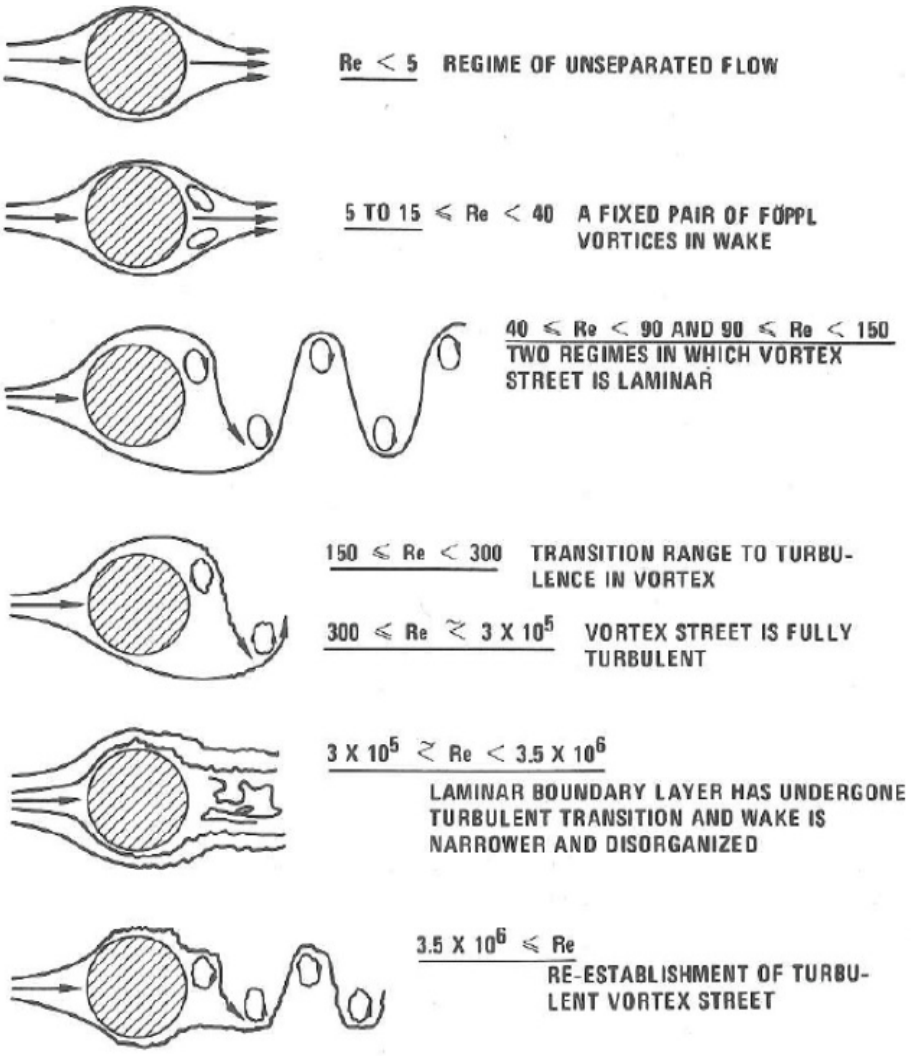

Figure 1.2: Variation of the flow around a circular cylinder with Re [9]

As shown in Figure 1.3, in this regime of interest, called sub-critical, due to the fact that the transition to turbulent boundary layer has not occurred yet, the boundary layer is attached to the cylinder until the separation point, located at around 70^o-80^o from the stagnation point.

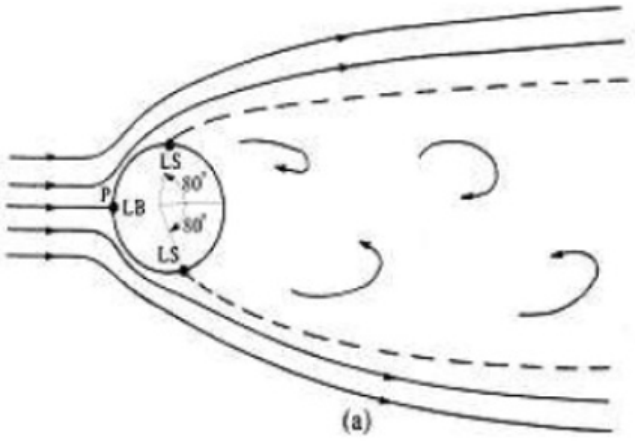

Figure 1.3: Separation of the flow around a cylinder in the sub-critical regime [46]

Vortex shedding modes

For increasing values of the Reynolds number, the vortex shedding mechanism is altered; if a two-dimensional wake characterizes the region downstream of the cylinder up to $Re \simeq 190$, three-dimensional effects appear at higher Re.
In particular, at $Re \simeq 190$, the transition from 2D to 3D wake occurs; in this regime, Williamson [63] observed three types of wake instability:

- Mode A: The primary spanwise vortices become unstable, thus large-scale streamwise vortex loops are generated at a wavelength of 3-4 cylinder's diamater.
- Mode B: It is characterized by the formation of small-scale streamwise vortex structures having a wavelength of 1 cylinder's diameter.
- Vortex dislocations: they are generated between spanwise cells of different frequencies, hence they naturally evolve along the span.

In the range $Re = [190, 300]$, the transition from Mode A to Mode B takes place. Mode B indeed occurs at $Re > 300$ and it is caused by an instability that scales on the thickness of the vorticity layer lying in the braid region [63]. It is then possible to conclude that a Mode B instability is expected in this project.

It was proven that Mode A and B have different symmetries; while Mode A is characterized by streamwise vortices of one sign in an alternate arrangement from one braid region to the next one, Mode B presents streamwise vortices of the same sign in-line arranged. A visualization of the two modes is available in Figure 1.4.

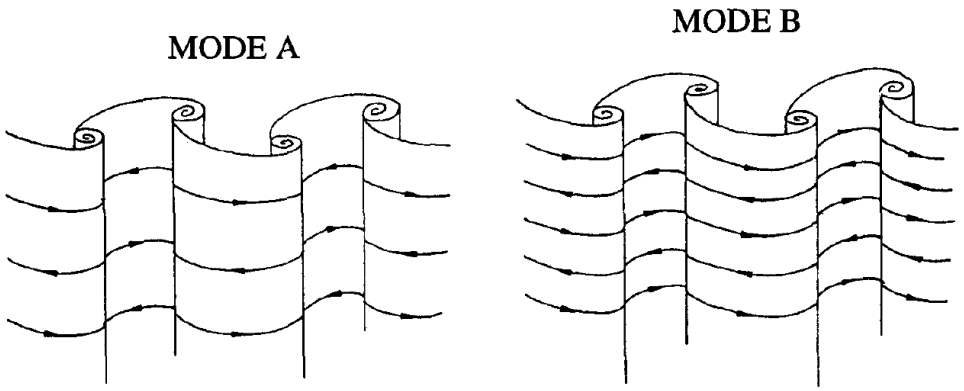

Figure 1.4: Example of Mode A (left) and Mode B (right) vortex instabilities [63]

At $Re = 5 \cdot 10^3$, small changes of shedding modes are observed; in particular, some dislocations of the vortex strictures along the span occur. Thus, vortex dislocations in the spanwise direction are also awaited in this study.

Furthermore, Williamson [63] demonstrated that the vortex structures do not always shed parallel to the cylinder's axis. They can indeed shed tilted by a certain angle to the axis, leading to the so-called *oblique shedding*. The angle of shedding results around 15^o-20^o.
This phenomenon is mainly due to the end conditions in the wind/water tunnel where the cylinder is tested, as they can affect and disturb the vortex shedding mechanism. In this project, where no-slip conditions will be assumed at the walls in order to simulate the cylinder being in the wind tunnel, the oblique shedding phenomenon is then expected.

1.1.2 The Strouhal number

At the end of the 19^{th} century, Strouhal [59] observed that the sound emitted from a cable subjected to the wind flow was a function of the velocity of the wind and of the cable's diameter. Furthermore, he was able to show an existing proportionality between the free-stream velocity, U_∞, the dimension of the body perpendicular to the oncoming flow-field (the body's diameter, in this study), D, and the frequency of the vortex shedding process, f_s. This proportionality is summarized in Equation 1.2, where St is known as the Strouhal number.

$$St = \frac{f_s \cdot D}{U_\infty} \tag{1.2}$$

Figure 1.5 displays the variation of the Strouahl number with the Reynolds number for a circular cylinder, where it is possible to notice an influence in the curve due to the surface roughness. Indeed, the roughness of the surface tends to increase the level of turbulence in the boundary level and, consequentially, to delay the boundary layer separation as the separation point moves downstream[2].

[2]In this study, the surface roughness of the cylinder will be neglected and a smooth cylinder will be assumed.

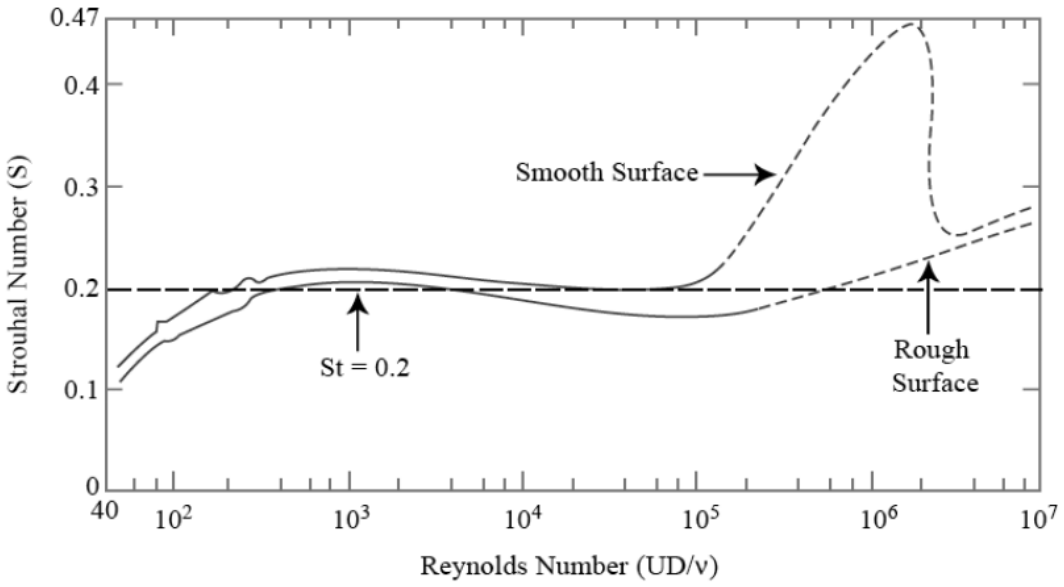

Figure 1.5: Variation of St with Re for a circular cylinder [60]

In the regime of interest (the sub-critical one), the Strouhal number approaches the value of 0.2. An empirical relation has been found by Fay et al. [21], described in Equation 1.3, where St^* and m are tabulated as functions of Re.

$$St = St^* + \frac{m}{\sqrt{Re}} \tag{1.3}$$

1.1.3 Drag and Lift Forces

One of the main challenges of the fluid-structure interaction in fluid mechanics is the determination of the forces done by the fluid on the structure. As a result of the flow reaching the solid body, the pressure distribution around the cylinder varies; the forces acting on the body are due to the pressure difference occurring between two sides of the cylinder. In particular, the so-called Drag Force, F_D, is defined as the force parallel to the incoming flow and it plays an important role in the bluff bodies aerodynamics (it tends to be negligible in the case of streamlined bodies, such as airfoil profiles). It can be written as:

$$F_D = \frac{1}{2} C_D \, \rho \, U_\infty \, A \tag{1.4}$$

where ρ and U_∞ are the density of the fluid and the free-stream velocity, respectively, A is the planform area of the body and C_D is the non-dimensional drag coefficient.
On the other hand, the force acting in the cross-flow direction, well known as Lift Force, F_L, given by the pressure difference between the top and the bottom part of the body, can be calculated as:

$$F_L = \frac{1}{2} C_L \, \rho \, U_\infty \, A \tag{1.5}$$

where ρ, U_∞ and A re the aforementioned density, velocity and area, respectively, and C_L is the non-dimensional lift coefficient.
For high Reynolds number, when a periodic change of vortex shedding leads to the

formation of the vortex street in the wake region downstream of the body, a periodic change in the pressure distribution around the cylinder is also observed. When the vortex shedding phenomenon occurs, non-zero lift and drag forces appear and they start fluctuating at a certain frequency, as Equation 1.6 and Equation 1.7 show.

$$F_L = \hat{F}_L \cdot \sin(\omega_s t) \tag{1.6}$$

$$F_D = \bar{F}_D + \hat{F}_D \cdot \sin(2\omega_s t) \tag{1.7}$$

$\hat{F}_L$ and $\hat{F}_D$ are the amplitudes of the oscillating lift and drag, respectively, while $\bar{F}_D$ is the mean drag.
From Equation 1.6 and Equation 1.7, it is possible to notice that the lift fluctuates with a frequency equal to $\omega_s = \frac{2\pi}{f_s}$, where f_s is the vortex shedding frequency, while the fluctuations of the drag force occur at a frequency double to the vortex shedding one.

A representation of the oscillating lift and drag coefficients is presented in Figure 1.6, where the dependency on the frequency of vortex shedding is clearly shown. It represents the time-varying lift and drag coefficient obtained by experimental results conducted at $Re = 1.1 \cdot 10^5$ by Sumer et al. [26]. The two unsteady aerodynamic coefficients appear far from being purely sinusoidal and their amplitude seems increasing with time, meaning that the stability of the vortex shedding mechanism has not been reached yet in the time range displayed in Figure 1.6. However, the different periods of oscillation and their proportionality to the vortex shedding period is observed.

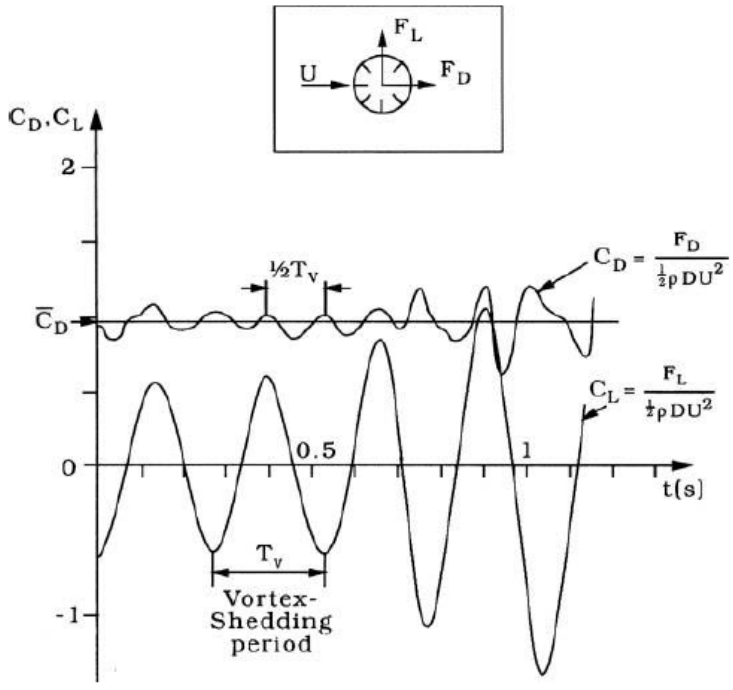

Figure 1.6: Oscillating lift and drag coefficients of a circular cylinder during the vortex shedding phenomenon [26]

1.1.4 Pressure Coefficient

The pressure coefficient, C_p, is a non-dimensional number describing the relative pressure throughout a flow field. It can be calculated at each location around the body using the following formula:

$$C_p = \frac{p - p_\infty}{\frac{1}{2}\rho_\infty U_\infty^2} \tag{1.8}$$

where p is the static pressure at the point at which the coefficient is evaluated, p_∞ is the flow static pressure in the free-stream, ρ_∞ is the flow density and U_∞ is the free-stream velocity of the fluid.
For incompressible fluids, where the variations in the density of the fluid are negligible due to very small variations in speed and pressure[3], the typical pressure coefficient distribution around a cylinder's section looks like the one displayed in Figure 1.7.
The angle θ, lying in a range of $[0^o, 180^o]$, characterizes the location around the cylinder's section at which the pressure coefficient is estimated; $\theta = 0^o$ represents the leading edge of the section, thus the first point reached by the incoming flow. Ascending values of θ are found moving clockwise starting from the leading edge of the circle. Hence, the trailing edge of the section occurs at $\theta = 180^o$.

There are three key aspects characterizing the pressure coefficient around a circular cylinder in Figure 1.7:

1. $C_p = 1$ corresponds to $\theta = 0^o$: this indicates the *stagnation point*, the location in a flow field at which the local velocity of the fluid is zero. Due to the presence of the cylinder, the flow is indeed brought to rest at the body's surface. Combining Equation 1.8 with the Bernoulli's equation ($p + \rho\, g\, z + \frac{1}{2}\rho u^2 = \text{const.}$), $C_p = 1$ is found exactly at the stagnation point.

2. After the stagnation point, the pressure coefficient decreases until reaching a minimum; this represents the point at which the boundary layer separation occurs, characterized by an adverse pressure gradient (increase in pressure moving along the cylinder's wall). The location of the minimum is know as θ_{sep}, the angle of separation.

3. The static pressure is replenished after θ_{sep} and a constant C_p value is reached, the so-called *base pressure coefficient*, C_{pb}. Indeed, after the point of separation, the wake region is encountered, which is dominated by a fairly constant wake pressure.

Given the symmetrical shape of the considered body, the pressure coefficient distribution in the bottom half of the cylinder's section ($\theta = [180^o, 360^o]$) is symmetric with respect to the one in the top half. For this reason, only the results obtained in the range $\theta = [0^o, 180^o]$ are usually presented.

[3]Assumptions valid for $M = u/c < 0.3$, where M is the Mach number, u is the local flow velocity and c is the speed of sound.

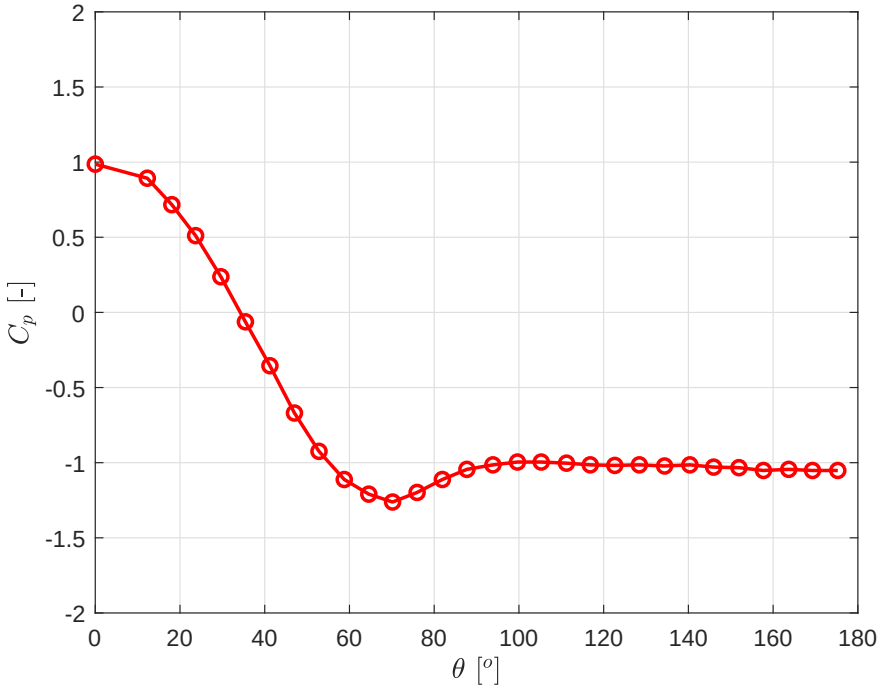

Figure 1.7: Pressure coefficient distribution around a circular cylinder at $Re = 8 \cdot 10^3$ from Norberg (adapted from [49])

Variations in the wind velocity can have a non-negligible effect on the pressure coefficient, in particular on the angle of separation and on the value of the base pressure coefficient. Hence, the C_p curve can change for different Reynolds numbers.

1.2 Vortex Induced Vibrations (VIV)

The presented analysis of the aerodynamics of bluff bodies is valid for the case of a static cylinder; further complications occur when the body is subjected to forced or free oscillations. While the forced motion of a body can be experimentally obtained by means of an external servo-motor, the free vibrations are generated by the effect of the flow reaching the body .

One of the most important phenomena occurring in the case of cylinders undergoing free vibrations is the Vortex Induced Vibrations (VIV) phenomenon. The latter, also known as Non-Synchronous Vibrations phenomenon, can be defined as the onset of vibrations induced on the body interacting with an external fluid flow, produced by periodical instabilities present in the flow. These oscillations occur transversely to the main fluid flow and are caused by the unsteady vortex shedding mechanism in the wake downstream of the body. They can be experimentally recreated in the wind tunnel by attaching the body to springs, varying the value of the incoming flow velocity.

For the analysis of this phenomenon, a further non-dimensional parameter is introduced: the *reduced velocity*. It is defined as in Equation 1.9,

$$U_r = \frac{U_\infty}{f\,D} \tag{1.9}$$

where D is the cylinder's diameter, U_∞ is the free-stream velocity and f denotes the frequency of oscillation of the body.

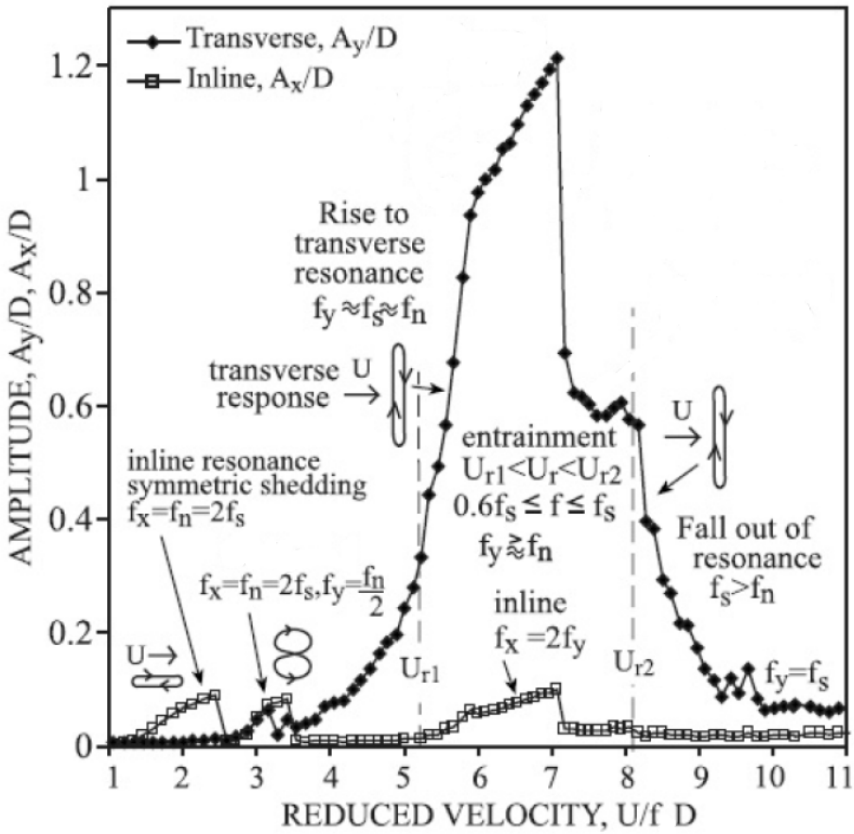

Figure 1.8: Variation of cylinder's oscillations amplitude for different reduced velocities in the sub-critical regime (adapted from [10])

Figure 1.8 proposes an interesting plot of the variation of the cross-flow and in-flow oscillations amplitude of a cylinder subjected to different airspeeds in the sub-critical regime. In particular, the transverse (A_y/D) and the in-line (A_x/D) amplitudes are presented as a function of the reduced velocity; four different cases are visible in Figure 1.8:

- $U_r < 1.25$: very low vibrations in both cross-flow and in-flow direction.
- $1.25 < U_r < 2.7$: only in-line oscillations occur at a frequency f_x equal to the natural frequency of the system, f_n. They are both equal to the double of the vortex shedding frequency, f_s.
- $2.7 < U_r < 5$: low amplitude oscillations with frequency $f_y = f_n/2$ in the cross-flow direction and $f_x = f_n = 2f_s$ in the in-line direction are observed. There is an alternated shedding of vortices.
- $5 < U_r < 8$: high amplitude oscillations in the cross-flow direction (the maximum peak reaches the value of $A_y/D \simeq 1.2D$) with $f_y \geq f_n$, and low amplitude oscillations in the in-line direction having $f_x = 2f_y$ occur.
- $8 < U_r < 11$: low amplitude oscillations only in the cross-flow direction where $f_y = f_s$.

As shown in the graph above, in the most critical area, where the oscillations amplitude approaches high values, the vortex shedding frequency, f_s, is close to the frequency of the oscillations of the body, f ($0.6f_s < f < f_s$). In particular, the cylinder's fluctuations appear to have a frequency of $f_y \geq f_n$ in the cross-flow direction and of $f_x = 2f_y$ in the in-line direction. Thus, the body's oscillations reached the natural frequency of the system, which undergoes resonance conditions.
It is possible to notice that the starting point of the critical area occurs at $U_r \simeq 5$; this is in line with the Strouhal relation expressed in Equation 1.2. Indeed, being $St \simeq 0.2$ in the sub-critical range of Reynolds, as shown in Figure 1.5, when f approaches f_s, $U_r = \frac{1}{St} = \frac{1}{0.2} = 5$.

For a cylinder free to vibrate, the aeroelastic resonance phenomenon (in the transverse and in the in-line direction) generated by the vortex shedding mechanism is the Vortex Induced Vibrations (VIV) phenomenon.
As shown in subsection 1.1.2, a proportionality between the vortex shedding frequency and the free-stream velocity is observed, according to the Strouhal relation, however, when the vortex shedding frequency, f_s, matches the natural frequency of the body, f_n, the Strouhal relation is not valid anymore and the instability occurs. In particular, in the critical range of U_r, the structural frequency and the vortex shedding frequency are synchronized even when varying the free-stream velocity. In this case, the cylinder's oscillation takes control of the vortex shedding process; this is known as *lock-in* or *synchronization* phenomenon.
In the case of a body forced to vibrate, the *lock-in* condition is achieved when the frequency of vortex shedding approaches the frequency of the imposed motion; a one-frequency system is created.

The key parameters acting during the VIV phenomenon are the airspeed, U_∞, the mass of the oscillating body, m, and the structural damping of the system, ζ. In order to estimate when a structure is likely to undergo VIV, Skop and Griffin [30] introduced a non-dimensional number combining the aforementioned parameters. The Skop-Griffin number unites both dynamic and aerodynamic parameters and it is calculated as follows:

$$S_G = 4\,\pi\,St^2\,\frac{m\,\zeta}{\rho\,D^2} \tag{1.10}$$

The ratio $\frac{m\,\zeta}{\rho\,D^2}$ is also known as the Scruton number, with ρ and D being the flow density and the reference length of the body, respectively. Skop and Griffin estimated that if $S_G > 5$, the structure will not undergo VIV.

Summarizing, a bluff body free to vibrate subjected to an incident flow will start to oscillate due to the interaction between the fluid and the structure. At low values of the reduced velocity, a proportionality between U_r and the frequency at which the vortices shed has been observed, hence, as shown in Figure 1.9, the ratio between the vortex shedding frequency and the structural frequency of the body follows the Strouhal relation described in Equation 1.2. However, starting from $U_r \simeq 5$ until $U_r \simeq 8$, the oscillation of the body takes control of the vortex shedding process and the aforementioned ratio keeps a value of 1 even for higher values of the reduced velocity. This region is called the *lock-in* region and it is characterized by an increase in the amplitude of the body's fluctuations.

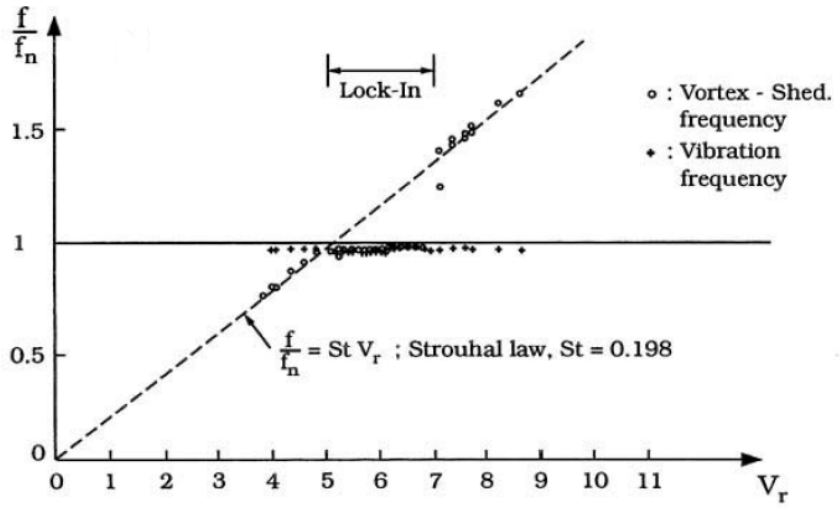

Figure 1.9: Variation of ratio between the vortex shedding frequency and the structural frequency of the body for different reduced velocities [24]

1.3 Cylinder undergoing forced motion

As mentioned, when the cylinder is forced to oscillate transverse to the flow, the *lock-in* condition is reached if the vortex shedding frequency approaches the frequency of the imposed motion; a one-frequency system is created. This can happen at different forcing frequencies and amplitudes; certain combinations of the two can indeed lead to lock-in even if the forcing frequency is relatively lower or higher than the vortex shedding one. Figure 1.10 shows the region of lock-in of a cylinder forced to oscillate transverse to the flow at $Re = 150$, where the frequency of vibration has been non-dimensionalized using the frequency of vortex shedding measured in the corresponding static case, and the vibration's amplitude through the cylinder's diameter.

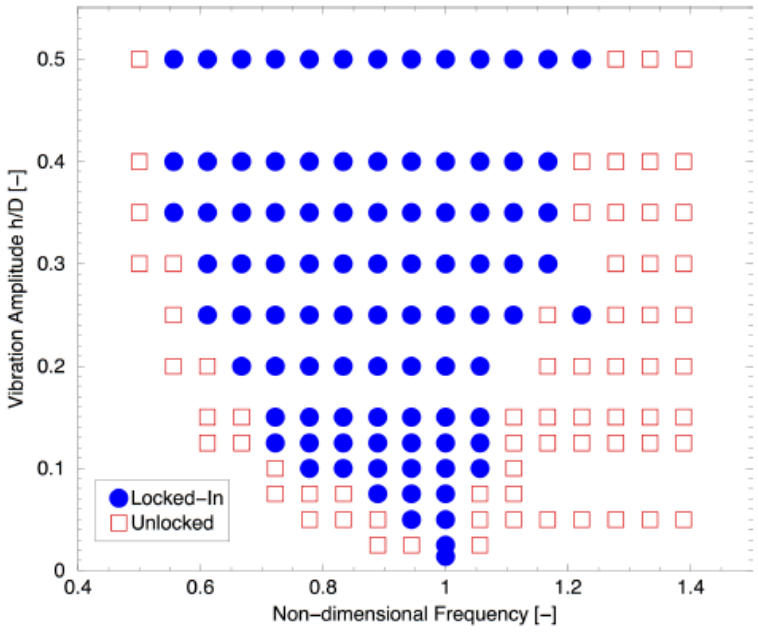

Figure 1.10: Lock-in region for the cylinder oscillating transverse to the flow at $Re = 150$ [7]

The region of lock-in appears roughly as a V-shape.
Intuitively, the static case corresponds to a vibration's amplitude of zero, where only the frequency of vortex shedding appears. On the other hand, for high oscillation amplitudes, the cylinder can more easily entrain the flow and the lock-in condition occurs over a larger range of non-dimensional frequencies.

A very interesting feature of the wake region appears during the motion of the cylinder, studied by Williamson and Roshko [56]; repeatable vortex patterns indeed occur within a certain rage of amplitudes. Two modes named P, meaning a pair of vortices, and S, indicating the shedding of a single vortex, appear, as well mode P+S, a combination of the two, where a vortex pair and a single vortex are shed in each cycle. Moreover, an evolution of modes S and P exists, namely mode 2S, when, in each half cycle, a vortex is fed into the downstream wake, like in the Von Kármán vortex street, and mode 2P, meaning that vortex pairs convecting laterally outwards from the wake centerline are formed.

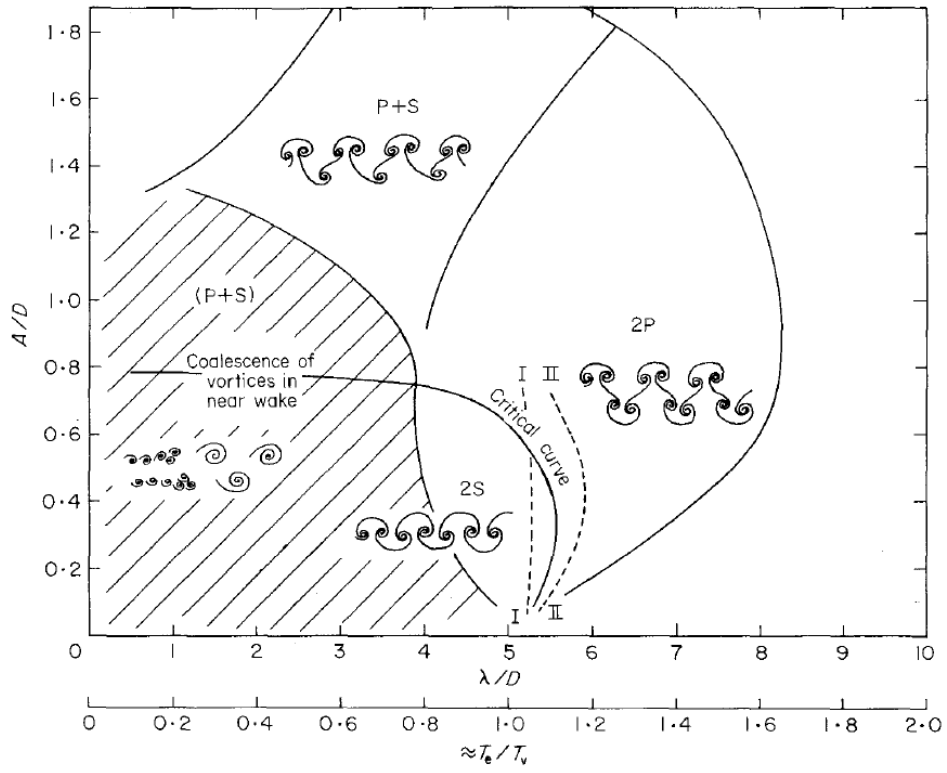

Figure 1.11: Visualization of the wake vortex patterns appearing downstream of a cylinder with imposed motion [56]

The lock-in region is usually characterized by modes 2S, 2P and P+S, as visible in Figure 1.11, which shows a map of the vortex synchronization patterns near the lock-in region obtained from experiments in the range $Re = [300, 1000]$. The axes represent the non-dimensional vibrations amplitude and λ/D, equal to reduced velocity U_r. On the other hand, T_e/T_v is the ratio between the period of the imposed oscillations and the period of vortex shedding of the static cylinder.
The critical curve in Figure 1.11 indicates the transition from one mode of vortex shedding to another, occurring close to $T_e/T_v = 1$, hence in the lock-in region neighborhood. Moreover, the dash curves labeled I and II represent the curves where the forces on the

body experience a sharp increase.

Mode P+S usually characterizes the cylinder forced to vibrate at oscillations amplitudes $A/D > 1$, while the mode 2S only appears at low amplitudes ($A/D < 0.8$). The region in Figure 1.11 marked by oblique lines indicates that, in the near wake, vortices organized following mode 2S or P+S are observed, but smaller vortices coalesce into larger scale structures. This can happen immediately behind the body or within about 15 diameters.

In this project, a cylinder forced to vibrate transverse to the flow will be simulated, thus the aforementioned vortex patterns are expected in the wake region downstream of the body.

1.4 Objectives of the thesis

Despite the high number of researches focused on the bluff bodies aerodynamics, a lack of informations regarding the behavior of the unsteady pressure around a cylinder within the lock-in range occurs.
The main objective of this thesis will be the analysis of the time-varying pressure around a circular cylinder forced to oscillate at certain frequencies and amplitudes. The aeroelastic response of the cylinder will be only introduced, but not further investigated.
Relevant importance will be given to the range of forcing frequencies and amplitudes allowing the cylinder to reach the lock-in condition. The variation in the unsteady pressure around the cylinder inside and outside of the lock-in range will be then analyzed, as well as the evolution of the lift coefficient, with the purpose of understanding how the switch from unlocked to locked cylinder occurs.

1.4.1 Summary by chapter

In this section, each chapter present in this thesis will be shortly summarized to have a general overview of the contents of this work.

Chapter 1

In the first chapter, an introduction to the topic of the thesis is given, while some useful informations regarding the bluff bodies aerodynamics and, hence, the flow parameters used in the project are discussed. The Vortex Induced Vibrations phenomenon is then presented, as well as the cylinder forced response.

Chapter 2

An experimental approach to the study of the unsteady pressure around a cylinder is described in chapter 2. A cylinder rig being designed for use in the Duke University wind tunnel is introduced. In particular, after a discussion regarding the flow parameters characterizing the experiment, the design of possible test rigs and cylinders is analyzed. Being the experiment meant to study both the aeroelastic and the forced response of the cylinder, the stepper motor to be used in the latter case is introduced and, finally, a short overview of possible pressure measurement systems is given.

Chapter 3

Due to the impossibility of proceeding with the experimental project, the Computational Fluid Dynamics (CFD) is used instead. The third chapter discusses the main CFD concepts, introducing the mathematical and numerical problem.
A deep discussion of the turbulence models needed to resolve the flow impacting the cylinder is also presented.

Chapter 4

The aim of chapter 4 is the design of a reliable and accurate computational model able to reproduce the flow around and downstream of the cylinder at high Reynolds numbers. Some experimental results previously obtained during a VIV experiment conducted in the University of Liège wind tunnel are used as benchmark to validate the numerical model. In particular, different mesh refinements, turbulence models and time-step sizes are investigated to build the best model for the present case.
The cylinder is simulated as static as well as undergoing forced motion through 3D simulations in Ansys Fluent 2019 R2.

Chapter 5

In this chapter, the analysis of the unsteady pressure around the cylinder is presented. In particular, the validated computational model is first used to simulate the forced motion of the body at different frequencies and amplitudes with the purpose of reaching the lock-in condition. Then, the evolution of the unsteady lift coefficient and pressure coefficient around the cylinder in the locked and unlocked cases is analyzed by studying the Fast Fourier Transform of the two coefficients. The pressure coefficient is evaluated at the different points around the mid-span section of the body.

Chapter 6

Chapter 6 aims to provide a comparison between the results obtained in the previous chapter with the results from the 2D study conducted by Oier Jauntsarats Sacedo [37]. For this purpose, the time-varying lift and pressure coefficients are analyzed and compared in both cases by means of their Fast Fourier Transform.

Chapter 7

Finally, a brief summary of the main concepts introduced and results obtained in this thesis is presented.

Chapter 2

Experimental test rig design

One of the main techniques used to study the flow impacting a solid body is certainly the wind and water tunnel experiment. The body is inserted in the tunnel, able to recreate the desired conditions of the flow (e.g. free-stream velocity, oncoming turbulence level). The principle advantage is that, once the experiment is correctly set up, the measurements can be acquired in a quite low amount of time. However, several parameters and possible sources of error must be taken into account during the measurements and a proper calibration of the experimental tools should be first conducted. Moreover, quite often a model rescaling is needed to allow the body to fit in the tunnel.

The aim of this chapter is to provide an overview of a possible experimental cylinder rig being designed for use in the Duke University wind tunnel. In particular, the final goal of the experiment would be the analysis of the unsteady pressure around the locked and unlocked cylinder. For this purpose, both the aeroelastic and the forced response of the cylinder should be tested.

2.1 Flow and cylinder parameters analysis

Several parameters must be considered during the test plan design, as they can lead to undesirable effects during the experiment.
First, the boundary conditions defining the air flowing in the wind tunnel must be clearly defined. Due to the Duke University wind tunnel settings, a laminar flow around the cylinder is impossible to be obtained, as a too high viscosity would be necessary. Hence, the flow will certainly be turbulent.
As explained in subsection 1.1.1, in the Reynolds range of $[3 \cdot 10^5, 3.5 \cdot 10^6]$, the flow in the boundary layer undergoes turbulent transition and the wake region downstream of the cylinder appears narrow and disorganized, which makes this range the one to be avoided. Furthermore, due to limitations of the flow speed in the wind tunnel, the Reynolds number should not exceed $3 \cdot 10^5$ during the test. Consequentially, as mentioned in chapter 1, the Strouhal number will be close to 0.2 for a smooth cylinder at the desired Reynolds numbers.

2.1.1 Flow speed

The range of available flow speeds is limited by the Duke University wind tunnel, which can perform between [5, 60] m/s. However, due to some flow instabilities in the tunnel, it is recommended to use a minimum speed of 10 m/s, reaching a maximum at 45 m/s. Moreover, it must be considered that, during wind tunnel testing, the flow speed experienced by the cylinder is higher than the imposed one, as the tunnel's boundaries force the flow to rest at their walls, slightly varying the flow streamlines. Therefore, the solid blockage effect must be taken into account; it can be calculated using the following correction factor [53]:

$$\varepsilon = \frac{0.96 \cdot V}{C^{3/2}} \tag{2.1}$$

with V and C the cylinder's volume and the wind tunnel cross section, respectively. The velocity seen by the body is then:

$$U = U_\infty(1 + \varepsilon) \tag{2.2}$$

2.1.2 Frequency and amplitude of the enforced harmonic motion

During the forced response test, an harmonic motion will be imposed to the cylinder transversely to the flow direction. While the amplitude of the oscillation can be controlled by changing the transmission settings explained in subsection 2.2.5, the frequency is controlled by the stepper motor used to force the cylinder's motion. In order to test the cylinder in both locked and unlocked conditions, the forcing frequency must be able to at least approach the vortex shedding frequency. Thus, the cylinder's diameter can be calculated by adapting the vortex shedding frequency to the desired forcing frequency given by the motor's characteristics and, then, using Equation 1.2. A small enough diameter is required in this project due to the dimensions of the wind tunnel test section. In particular, the diameter-to-length ratio of the cylinder must be kept as low as possible to avoid non-negligible end effects, which can alter the unsteady pressure measurements.

Two options are available in the forced response test; varying the frequency and the amplitude of the forced motion by altering the stepper motor settings accordingly, or varying the flow speed, changing the frequency of shedding but keeping the forcing frequency constant. A MATLAB script has then been used to find the optimal parameters given the flow limitations; the latters are listed in Table 2.1. The code aimed to minimize the forcing frequency when the lock-in condition is reached to reduce the motor's power.

Table 2.1: Optimal parameters to force the cylinder reaching the lock-in condition

Parameters	**Values**
Cylinder diameter [m]	0.1016
Wind tunnel speed [m/s]	11.25
Reynolds number [-]	$7.6 \cdot 10^4$
Forcing frequency [Hz]	22.15

The flow speed should then be gradually incremented, while the amplitude of oscillations can vary in the range [10%, 50%] of one cylinder's diameter.

2.2 Test rig design

Once the conditions of the flow are set, the test rig to be used during the experiments can be designed.
One of the key points to be considered during the design is obviously the limitation given by the size of the tunnel where the experiments will take place. In this study, they are thought to be conducted in the wind tunnel of Duke University, where the following requirements must be fulfilled:

- The test rig shall be able to fit in the tunnel test section (50in x 28in x 20in (LxWxH)).
- The rig shall be able to be easily disassembled and removed from test section.
- The rig shall be able to test both the aeroelastic and the forced response of a shedding cylinder.

A wide range of experimental rigs could be designed to meet the aforementioned requirements; in this study, 3 main designs were carried out, among which only one has been chosen. For this purpose, the CAD software used is SOLIDWORKS.
In the following subsections the supporting structures designed to hold the cylinder will be presented. Moreover, the transmission system, needed in the forced response setup to translate the rotational motion of the motor to a linear motion of the cylinder, will be introduced.

2.2.1 Design 1 - Horizontal cylinder with linear bearing

The first idea was to position the cylinder horizontally, with its motion then happening along the vertical direction (always transverse to the flow).
Figure 2.1 shows the flow direction, indicated by the black arrow, and the first rig designed, which would see the edges of the cylinder fixed to the sliders, the two black objects attached to the vertical beams. The presence of sliders at both sides of the structure is necessary to enforce the motion of the cylinder, which would then have its edges mounted on them. They can move along a linear bearing pushed by a rod from the transmission system. The cylinder's edges can be then attached to springs, lying parallel to the vertical bearings, for the simulation of the aeroelastic case.
Due to the presence of a sloped face on both sides of the wind tunnel at both the top and bottom, the vertical beams are designed in such a way to rest on this sloped face.

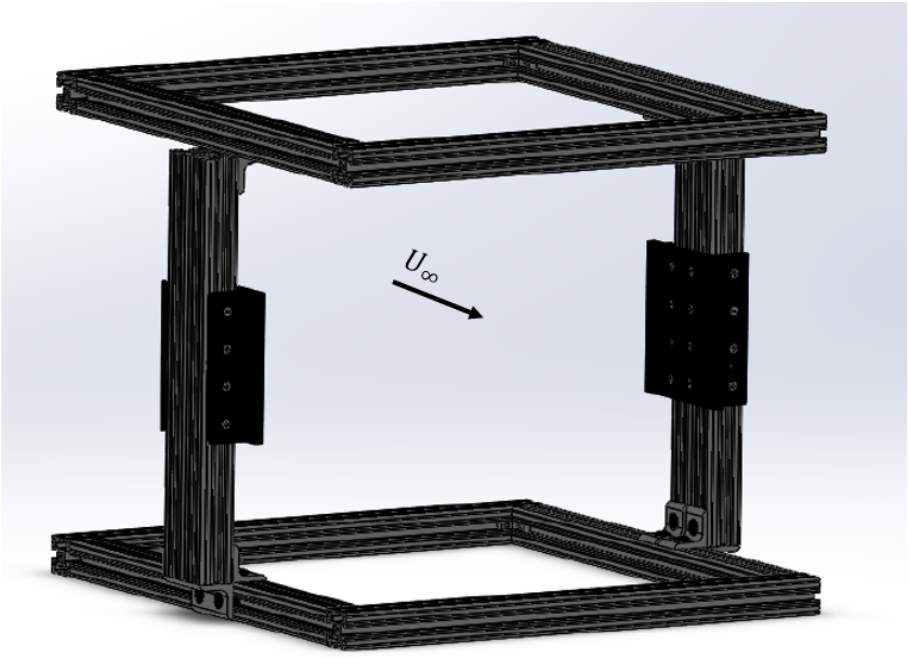

Figure 2.1: First test rig design

2.2.2 Design 2 - Horizontal cylinder with cable system

In the second design, an horizontal cylinder is again conceived. However, the sliders are here substituted by a cable on which the cylinder can slide or be forced from.
Indeed, clamping the cylinder's edges to the cable, the imposed motion of the cable would lead to the oscillation of the cylinder. Furthermore, for the aeroelastic setup, the cylinder would be attached to springs using hooks on its edges and the cable would only guide the cylinder without forcing its motion.
Figure 2.2 displays the second test rig design in both the aeroelastic and forced response setup.

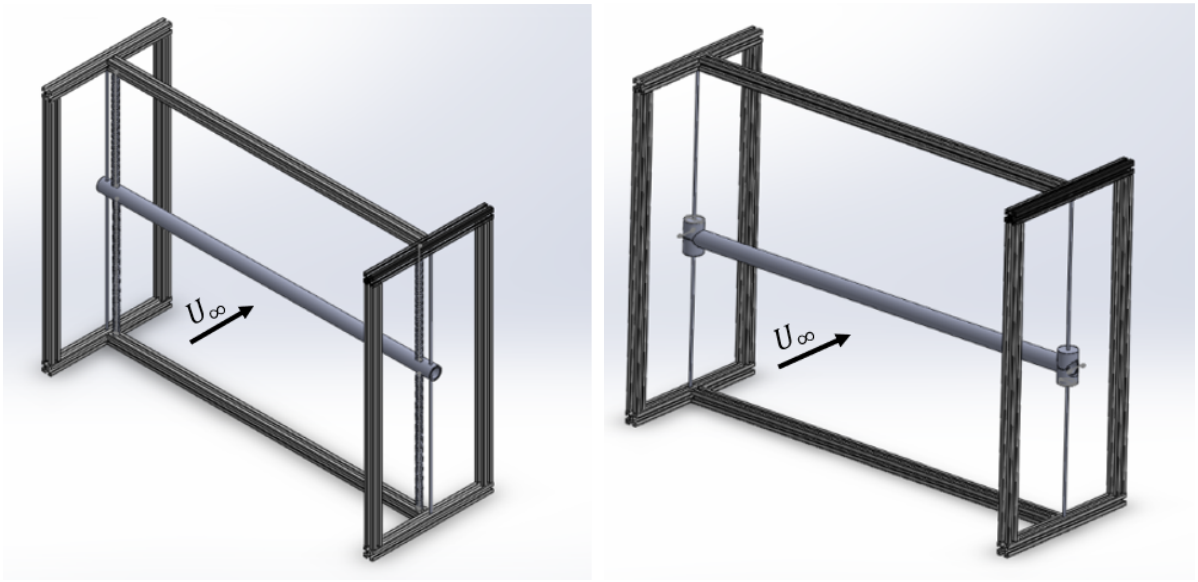

(a) Aeroelastic setup (b) Forced response setup

Figure 2.2: Second test rig design

2.2.3 Design 3 - Vertical cylinder

In the third model, presented in Figure 2.3 the cylinder is designed in a vertical orientation, while its movement follows the horizontal beams.
This design results very similar to the one in Figure 2.1, but oriented in a different direction. The cylinder's edges are indeed attached to sliders to allow the movement along the horizontal direction. Moreover, springs are inserted to study the aeroelastic response of the body.

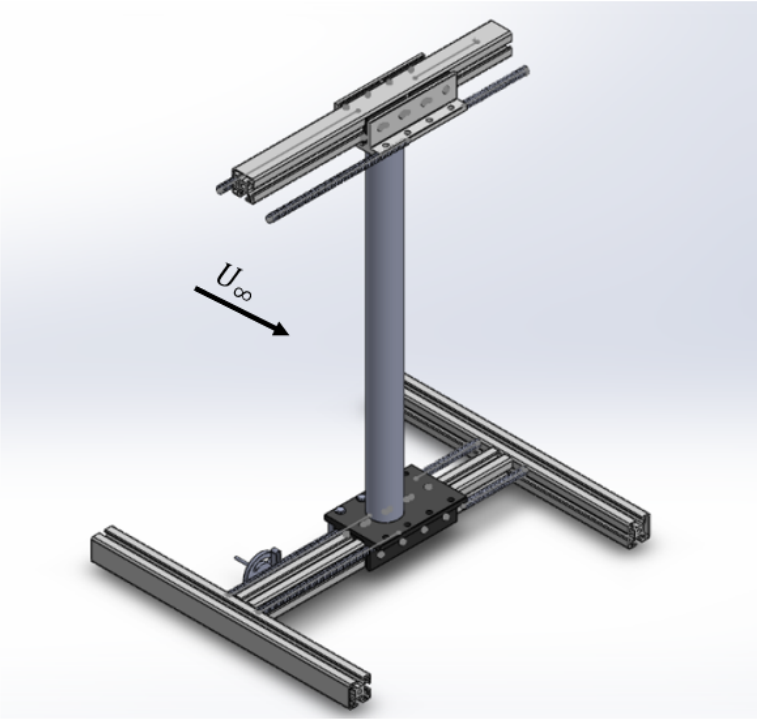

Figure 2.3: Third test rig design

Due to the presence of holes at the top and at the bottom of the test section, the majority of the rig could be easily placed outside the wind tunnel, automatically removing any possible effect that the test rig may have on the airflow impacting the cylinder.
A sketch of how this design would look like when inserted in the Duke University wind tunnel is available in Figure 2.4.

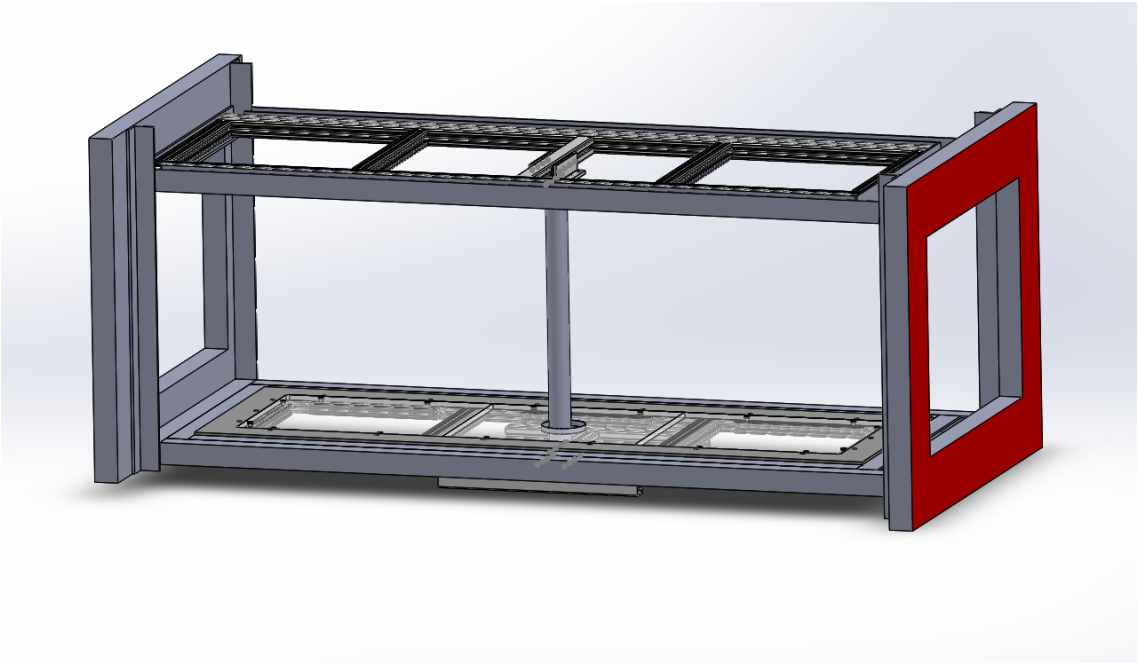

Figure 2.4: Third test rig design inserted in the wind tunnel of Duke University

2.2.4 Comparison between the three rig designs

The first test rig design is very suitable for the present experiment, as the sliders attached to the stiff bearings are able to ensure the vertical motion of the cylinder avoiding possible problems related to the flexibility and the bending of the cable in the second design. Moreover, the latter presents the difficulty in the clampers positioning, as they should be slid on from one side of the cable and then fixed in place, hence the setup must be partially disassembled to mount the aeroelastic setup.
For this reason, the first design is preferred over the second one.

On the other hand, to compare the first and the third design, the advantages and disadvantages of the choosing the vertical test rig in subsection 2.2.3 with respect to the horizontal test rig in subsection 2.2.1 are listed below.

- In the vertical rig, the transmission system could be located outside the test section, avoiding possible problems of interference with the measurements.
- The pressure tubes in the third design would run directly outside the tunnel.
- Due to the tunnel's dimension, a shorter cylinder is necessary in the design 3. Thus, the diameter-to-length ratio of the cylinder results higher, leading to bigger undesirable end effects.
- Using the vertical design, the hole present in the bottom part of the test section should be modified to allow the cylinder to be mounted.
- As the cylinder's oscillations must be enforced at both edges of the body, the whole transmission system in the third design must be built all around the wind tunnel.

These reasons make the first test rig design the best one to be used in both the aeroelastic and the forced response experiments, as more difficulties would be encountered using the thirst test rig design, especially when mounting the transmission system around the wind tunnel.

Even though the rig could be fixed to the top and the bottom areas of the test section, an investigation into the stiffness and natural frequency of the rig must be performed to ensure that it does not deform nor interfere with the measurements.
The locations that are most likely to vibrate are the cantilevered sections and the sections with few support, such as the long horizontal beams across the width of the wind tunnel. Hence, a ping test of the structure should be conducted before proceeding with the experiment.

2.2.5 Transmission systems

The three different transmission systems designed are presented in this section and the best one will be chosen among the them.

Scotch yoke driven from axle

The most common mechanism to translate rotational motion into linear motion is the scotch yoke, which will be used in this project.
The transmission system is designed to be placed at the bottom part of the rig, as shown in Figure 2.5 by the scotch yoke mechanism on the left side of the rig.

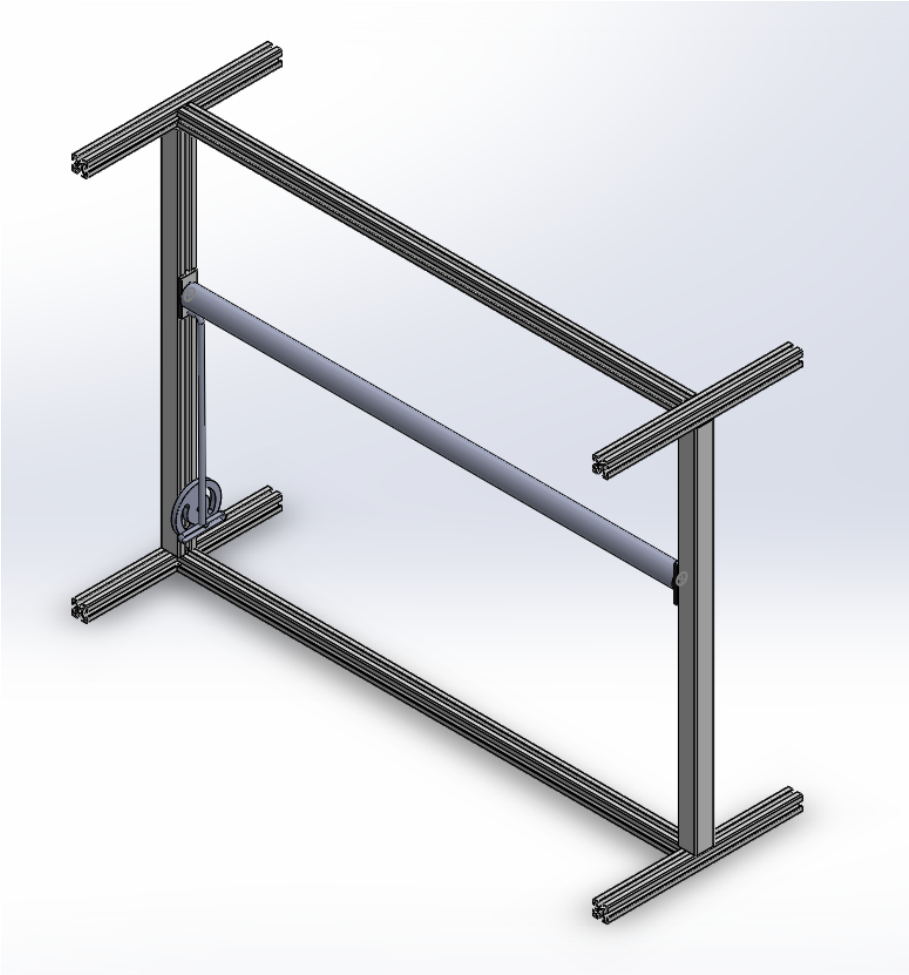

Figure 2.5: Representation of the test rig and the transmission system

In the first design, visible in two zooms available in Figure 2.6 and Figure 2.7, a long rod over the bottom horizontal beam works as a shaft driven by the motor. The rotation of the shaft induces the rotation of a gear which meshes another gear, allowing the rotation of the disk of the scotch yoke mechanism. The rotation of the disk then leads to the translation of the rods attached to the sliders and thus to the motion of the cylinder.
By 3D-printing gears with different sizes (not shown in Figure 2.6 and Figure 2.7), the gear ratios could be varied to increase the frequency of the rotation.

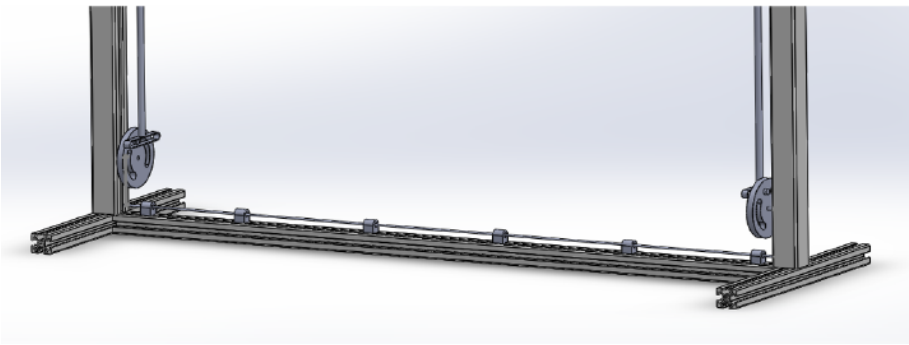

Figure 2.6: Transmission system: design 1

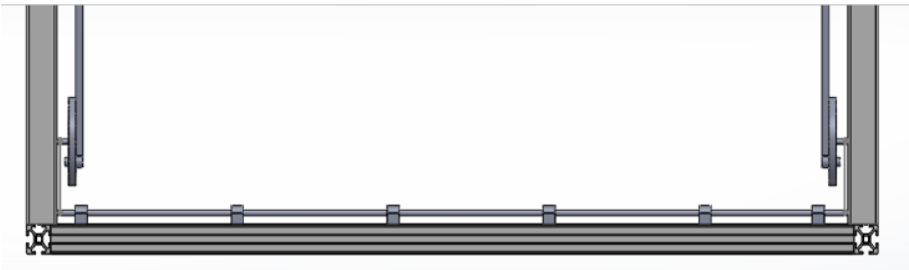

Figure 2.7: Transmission system: design 1 (side view)

Linked Scotch yoke

A rigid rod is positioned between the two disks of the scotch yoke mechanism present at both sides of the rig in the second design. The motor is then attached to one of the disks, being translated to the other disk thanks to the stiff rod.
However, in this design, the motor should be introduced in the wind tunnel and it could interact with the main flow leading to non-negligible effects.

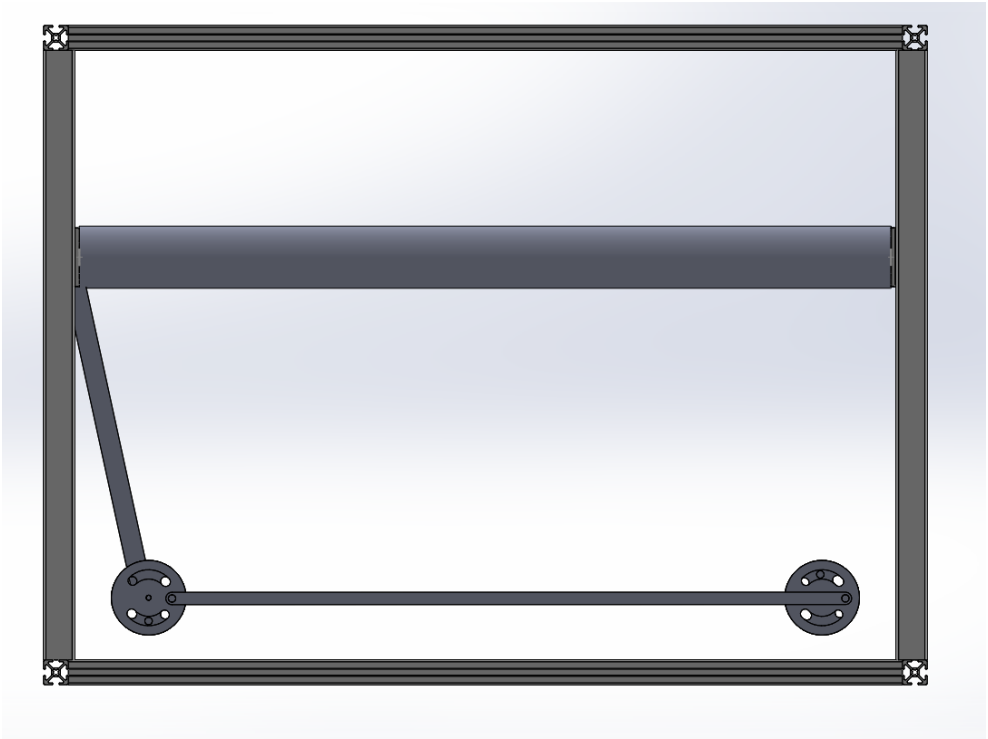

Figure 2.8: Transmission system: design 2

Cable driven Scotch yoke

In the third design, the two disks of the scotch yoke mechanisms are driven by a cable or a belt, as shown in Figure 2.9. Then, a small wheel attached to the motor should be positioned in the system to drive the cable's motion.
However, potential flex in the cable and cable slipping are two problems to be considered when implementing this system. Moreover, it appears difficult to vary the frequency and the amplitude of motion, since this could be done only by changing the position of the disks.

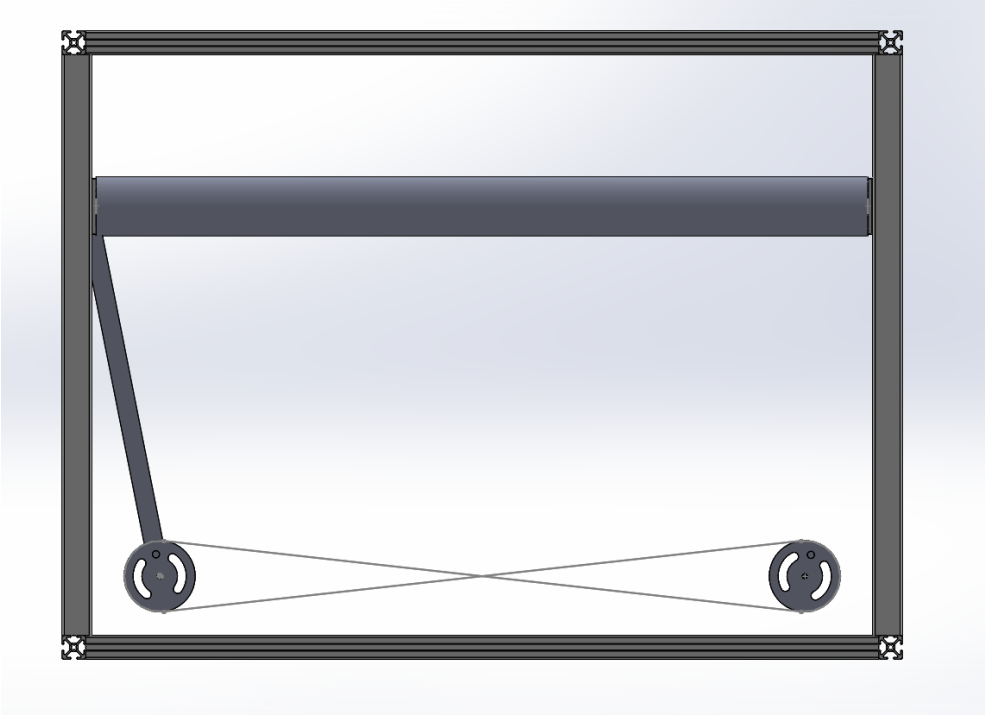

Figure 2.9: Transmission system: design 3

Comparison between the three transmission system designs

Due to possible problems related to the rigidity of the rod in the second design and the flexibility and slipping of the cable in the third design, the first design appears the most suitable for this project. Some details of the mechanism are available in Figure 2.10 and Figure 2.11, where the rod which pushes the sliders and its connection with the cylinder are presented.

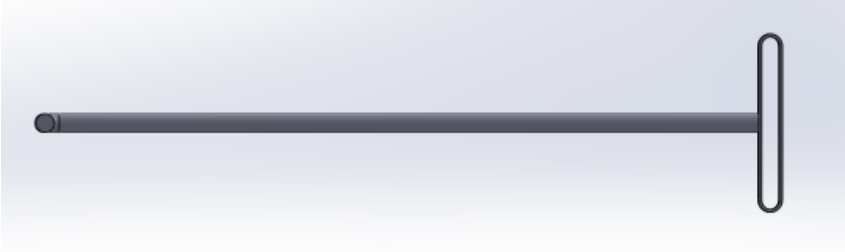

Figure 2.10: Pushing rod

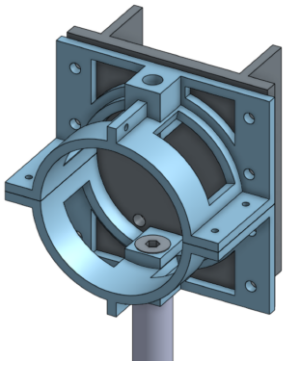

Figure 2.11: Rod-cylinder connection

Changing the size of the disk in the Scotch yoke to which the rod is attached, the amplitude of the motion can be varied. Disks of different diameters can be easily 3D-printed using plastic.
It was first decided to also 3D-print the rod in plastic, however this procedure produced an insufficiently strong rod, which is not able to sustain the motion. Hence, it should be strengthen by increasing its thickness or by adopting stiffer materials, like aluminum or steel.

Plastic was also assigned to the sliders by simply 3D-printing them using the CAD from the 80/20 company[1]. Figure 2.12 shows a picture of the plastic slider (left) and the regular 80/20 slider (right). The white pieces seen screwed onto the original piece would then be attached to the 3D-printed component. This decision was made in order to decrease the overall weight of the structure moved by motor. However, the tolerances of the piece must be considered during the printing process, as a non-perfect slider would then lead to friction during its motion. Hence, the component should also be sanded down and lubricant should be applied to its surface.

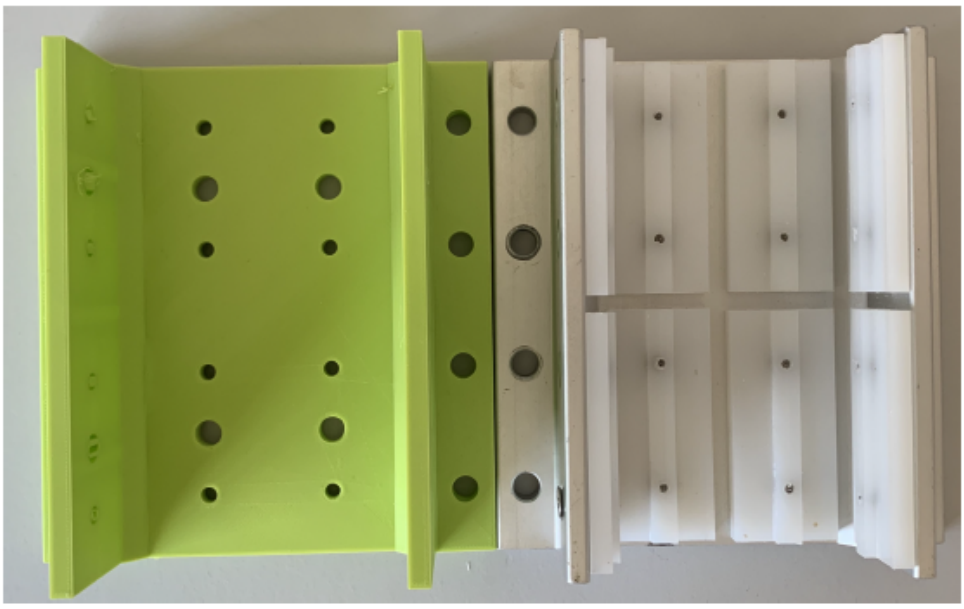

Figure 2.12: 3D printed slider (left) and regular 80/20 slider (right)

[1]Components from this company were used as 80/20 beams and sliders are available at Duke University.

2.3 Stepper motor

The available stepper motor to be used to force the cylinder's oscillation is the National Instruments NI-ISM-7411E pictured in Figure 2.13.
Once connected to the appropriate power supply, its rotation can be controlled using LabVIEW.

Figure 2.13: National Instruments NI-ISM-7411E stepper motor [47]

A key parameter to consider is the motor power output. For the present case, from previous experiments conducted in the University of Liège wind tunnel, a power of several hundreds watts was estimated to be necessary to impose the motion of the cylinder at the desired frequency and amplitude.
Looking at the manufacturer provided torque-speed curve in Figure 2.14 and knowing that the motor available is the 24 V DC variant, the power can be calculated.

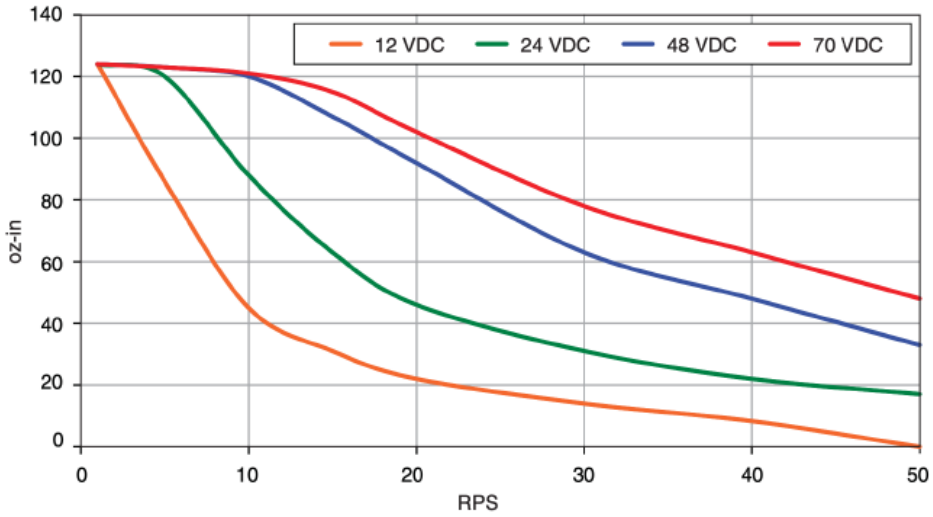

Figure 2.14: Torque-speed curve for the NI-ISM-7411 [47]

P being the power, T the torque and ω the angular velocity, the power is calculated as:

$$P = T \cdot \omega \tag{2.3}$$

The angular velocity is linked to the rotations-per-second, RPS, shown in the graph in Figure 2.14, via the following equation:

$$\omega = 2\pi \cdot RPS \tag{2.4}$$

Substituting Equation 2.4 into Equation 2.3 and collecting the data from the green curve in Figure 2.14, after converting the torque to SI units (i.e. [N·m]), the power can be found as a function of RPS, as shown in Figure 2.15.

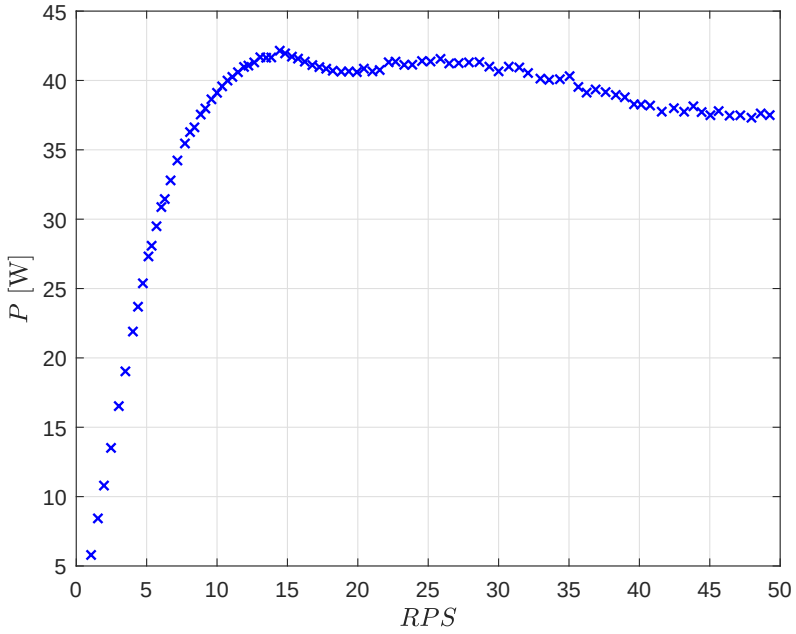

Figure 2.15: Estimated power-speed curve for the NI-ISM-7411

It can be noticed from Figure 2.15 that the maximum power of the motor is around 42 W, significantly lower than the expected one. Hence, the motor available at Duke University seems not powerful enough to work in the present experiment and another model should then be considered.

2.4 Cylinder design

In this section, the designs considered for the cylinder's creation will be shown. All the CAD models will present 10 pressure taps around the cylinder's mid-span section, however more taps are recommended for the acquisition of the unsteady pressure.

During the cylinder's design, the following requirements must be met:

- The cylinder shall have an outer diameter of 0.1016 m and a length of 0.65 m to meet the flow criteria described in section 2.1 and the wind tunnel's depth.
- The cylinder shall be light enough to decrease the needed motor's power.
- The cylinder shall be able to hold pressure taps inside or attach sealed tubes that run through the cylinder and connect to taps outside the wind tunnel.

- The cylinder shall attach securely to the rig in both the aeroelastic and forced response setups.
- The cylinder shall have room on the ends for the pressure tubes to exit the sides of the rig.
- The cylinder shall remain as smooth and as cylindrical as possible to ensure it matches theoretical analyses.

To simplify the cylinder's construction and the locations of tubes and probes in it, it was decided to divide it in multiple pieces which can be easily mounted and unmounted.

2.4.1 Design 1

In the first design, the cylinder is divided into three pieces; the center piece would house either the pressure taps or connect to tubing that would run outside of the cylinder through the opening cylinder edges. They would then connect to the Data Acquisition System (DAQ).
This piece would be custom, therefore an additive manufacturing technique must be used.

Cylinder side pieces

The creation of custom step-down tabs on the sides of the center piece is needed to assembly the three parts together. Then, the two side pieces would be made out of a stock pipe material due to its small tolerances for surface roughness and roundness compared with the ones occurring in the case of custom pieces.

Two materials were considered for the side pieces, PVC and aluminum.
For PVC pieces, the cylinder is specified to have an outer diameter (OD) of 4", which is the OD of a standard 3.5" Nominal Schedule 40 PVC pipe. PVC is relatively light, cheap, and smooth, with a linear density of 92.2 g/cm. On the other hand, for aluminum pieces, the thinnest 4.5" diameter pipe available online has a wall thickness of 1/4", and a linear density of 147.8 g/cm, almost twice that of the PVC. Despite the disadvantage of an higher density, the aluminum has a much bigger stiffness-to-density ratio with respect to the PVC, and therefore can provide the stiffness necessary for the experiment with a thinner and lighter cylinder.

Cylinder center piece - design 1a

In this design, there are inserts on the side of the center piece to directly attach the tubes connected to the pressure transducers.
As shown in Figure 2.16, holes of 1 mm diameter are designed for inserting the pressure taps; the holes then expand to 1.3 mm so the tubes can fit snugly in the insert.

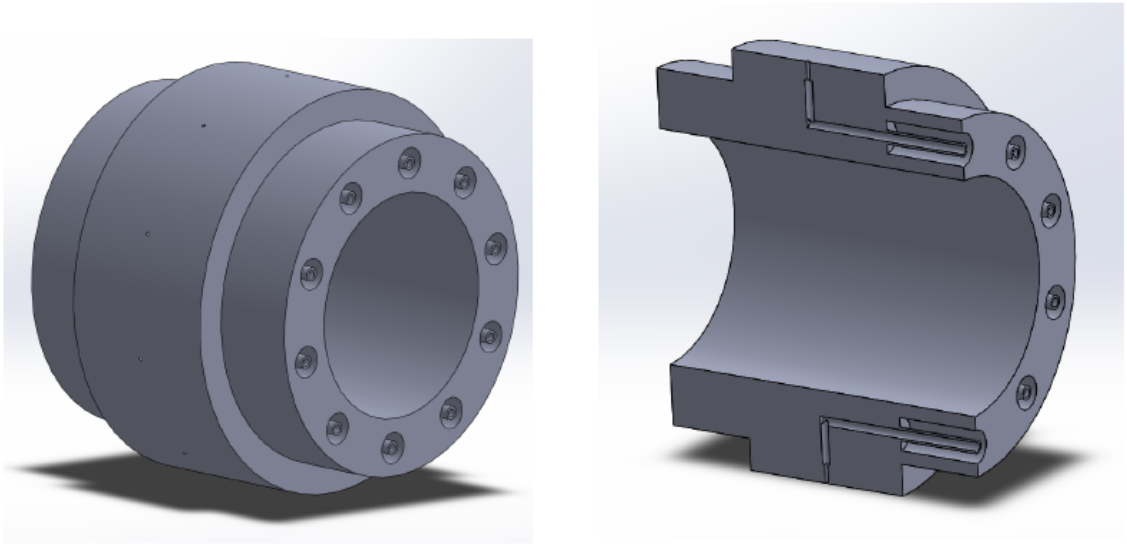

(a) Cylinder 1a: center piece (b) Cylinder 1a: center piece section

Figure 2.16: Cylinder design 1a

Due to the high resolution of pressure tap holes, the plastic 3D-printers cannot accurately perform the construction of the cylinder center piece, therefore titanium 3D-printers should be used instead, being the only printers with a high enough resolution. However, this would lead to a non-negligible increase in the cylinder's weight, introducing possible issues in the motor's performance during the forced response case.

Cylinder center piece - design 1b

The particularity of this design is the fact that the pressure transducers are flush-mounted on the cylinder center piece, as shown in Figure 2.17.

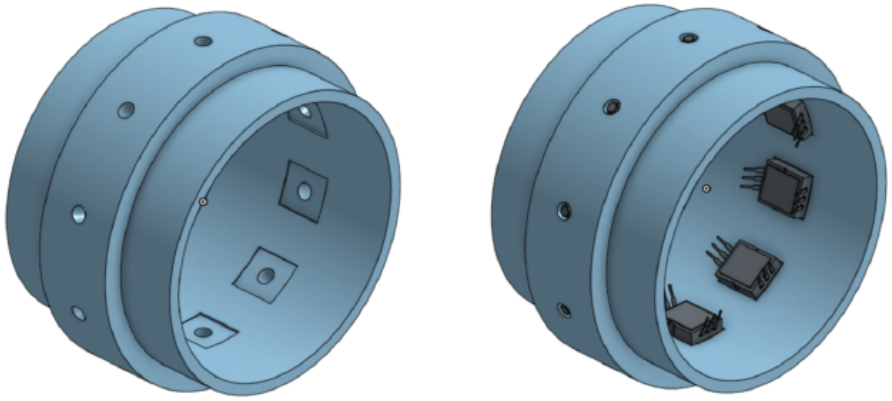

Figure 2.17: Cylinder design 1b: center piece with (right) and without (left) pressure transducers

A sectional view in available in Figure 2.18.

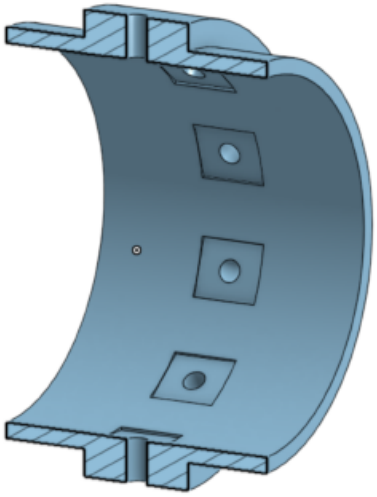

Figure 2.18: Cylinder design 1b: center piece section

The flat section under the tap hole visible in Figure 2.18 is the location where the pressure transducers can be glued or epoxied. Moreover, since the pressure tap is directly inserted into the tap hole, the latter can be larger and less precision in the manufacturing method is then needed. Thus, the piece could be 3D-printed using plastic, which would highly reduce its weight.

Furthermore, as the taps are directly connected to the cylinder, only the small wirings attached to the transducer will run through the cylinder instead of larger pressure tap tubes, which could simplify the overall assembly.

2.4.2 Design 2

In the second design, a square section is cut out of the center of the cylinder, allowing to position the pressure taps, flush-mounted inside the pipe, as visible in Figure 2.19.

Despite its simplicity, this design requires precise machinery to properly cut out the square slot exact enough that it can be placed back onto the cylinder after the taps are placed. Furthermore, a difficulty in creating the holes to connect the taps to the cylinder, due to the difference in shape between the cylinder and the flat transducers, is encountered.

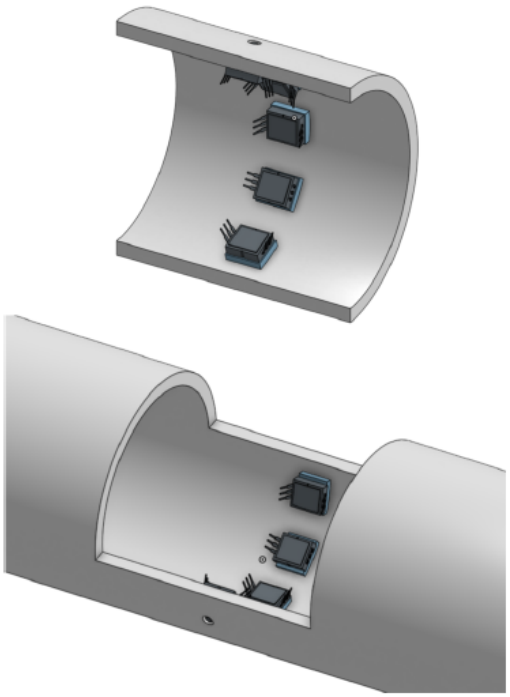

Figure 2.19: Cylinder design 2

A custom connecting piece, like the one shown in Figure 2.20, must be created so that the taps do not extend past the surface of the cylinder. It should be rounded on one side, to be flush with the cylinder, and flat on the other to provide a surface to glue or epoxy the tap to.

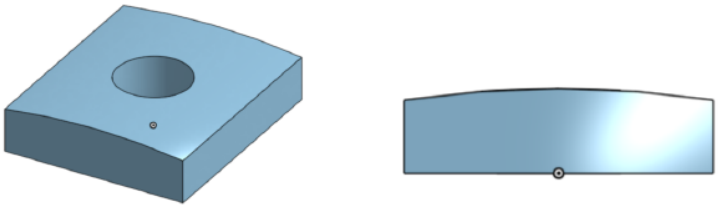

Figure 2.20: Cylinder design 2: connecting piece

Due to the aforementioned problems, the design 1b was considered as the best for the present experiment, as a cylinder divided in pieces seems easier to manufacture and requires less hand machining. Moreover, the design 1b allows to have less strict tolerances than the ones needed in the design 1a.
Then, due to its availability and its minimum post-processing, PVC is the recommended material for the side pieces of the cylinder.
Before wind tunnel testing, the cylinder should be first polished in order to refine its cylindricity, aligning the experimental results with the theoretical models.

2.4.3 Cylinder ends

Since the cylinder's edges must be attached to the sliders, a specific end piece must be used. This needs to have openings so wiring and tubing can be run through the inside of

the cylinder.

The design in Figure 2.21 shows half of the end part created, which would be 3D-printed and bolt onto the other half to create the whole piece. The flat section is then designed to be bolt onto the 80/20 slider (P/N 6524).
The horizontal hole on the top of the end piece is for hooking on springs in the aeroelastic case, while the vertical hole on the top is for attaching the push rod to the Scotch yoke for the forced response case. Clearly, the radius of the circular inner section of the end piece is the same as the cylinder's radius and the openings on the sides are to pass wires or tubes from the inside of the cylinder to the DAQ outside of the wind tunnel.

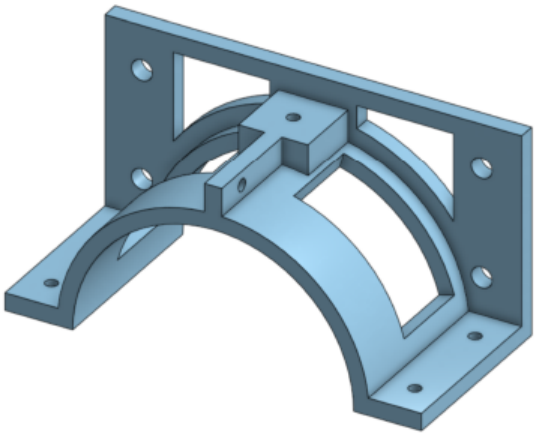

Figure 2.21: Cylinder end piece

2.5 Measurements system

After the test rig design, the measurement system used to get the pressure on the cylinder's surface must be considered. In this project, it was chosen to work at the mid-span section of the cylinder, in order to minimize the undesired end effects from the edges of the cylinder and the wind tunnel walls.
Two measurement systems have been taken into account in this study.

2.5.1 Pressure transducers system

The Fujikura APB2 pressure transducers were first considered, due to their very low cost (10 USD). They are made by a silicon piezoresistive pressure sensing chip, where the output signal is proportional to the applied pressure.
As shown in Figure 2.22, several variants are available, with an accuracy of the sensor of 1.5%FS or 2%FS. Only the 3 V DC variant was considered, as the highest accuracy is needed in this experiment. The transducer chosen was then the one labeled "025kg" in Figure 2.22, as the dynamic pressure that would be measured are very small (on the order of few 100 Pa).

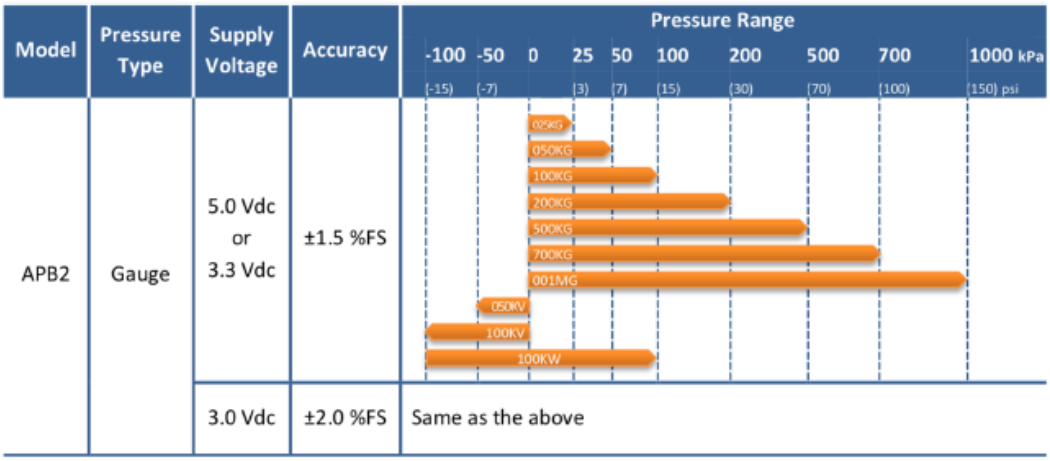

Figure 2.22: Fujikura APB2 device lineup [27]

There are two ways of mounting the pressure transducers:

1. The transducers are mounted directly into the surface of the cylinder (flush-mounted pressure transducers). Wirings would then run through the cylinder and transmit the signal to the DAQ available in the Duke University wind tunnel. This system has the big advantage of eliminating errors due to tubes transmitting the pressure to the transducers, which would then need a proper static and dynamic calibration. However, on the other hand, it leads to obvious problems derived by the difficulty of mounting the fragile transducers in the small space inside the cylinder.

2. The pressure transducers are positioned outside the wind tunnel and are connected to the cylinder by means of tubes. While it appears easy to mount and unmount the transducers, this system requires more extensive and complicated calibrations, due to the presence of the tubes.

2.5.2 Pressure scanner system

An alternative to the pressure transducers is the pressure scanner provided by the University of Liège (the nanoDAQ-32, made by Chell Instruments [17]). It is able to simultaneously measure pressure at 36 taps, performing up to 5000 measurements/channel/second to ensure that enough data can be collected over one time period.
The setup is small enough to be mounted inside the cylinder and requires only the design of a bracket on which the device can be mounted.

The system takes measurements from small holes drilled into the surface of the cylinder, hence plastic tubes must be fixed on the hole by gluing them and run them to the scanner. It was recommended to use tubes from Scanivalve, either the URTH-040 (a Urethane material) or VINL-040 (a Vinyl material). Consequentially, 36 holes should be drilled along the mid-span section of the cylinder, placing a tap every 10^o; this ensures an accurate measurement of the unsteady pressure all over the section.
Due to its accuracy and to its simple design, this method is preferred over the pressure transducers system.

Chapter 3

Computational Fluid Dynamics

Computational fluid dynamics is a branch of fluid mechanics; it is often abbreviated as CFD and its main purpose is to analyze and solve problems involving fluid flows, heat transfer and associated phenomena, such as chemical reactions, using numerical analysis and data structure. The problem can be simulated by the CFD software, which can model the free-stream flow of the fluid and its interaction with a certain body. In this way, CFD is used in a wide range of applications in many fields of industries and studies and it represents a very powerful technique to simulate fluid flows.
Its principle advantage consists in solving the problems without the need of big and/or expensive test facilities and laboratories. Moreover, a model rescaling is not required and several interesting quantities can be obtained by running only one simulation (velocity, pressure, temperature, etc).
However, a validation of the model used to simulate the problem needs to be done; in this study, the computational model of a 3D cylinder will be built and validated using some experimental results obtained in the wind tunnel of the University of Liège.

In this chapter, the mathematical problem will be first discussed and, afterwards, the main CFD tools will be presented.

3.1 The Navier-Stokes equations

Every CFD code is stated in a set of mathematical equations and solved numerically. In particular, the basic equations to be solved are the conservation laws of fluid motion, such as conservation of mass, momentum and energy, well know as the Navier-Stokes equations. They consists in a set of partial differential equations describing the motion of viscous fluids.
As CFD problems deal with fluid flows, the conservation laws of mass and momentum need to be satisfied.
In order to have a better understanding of these conservation laws, a closed control volume, such as the one represented in Figure 3.1, will be introduced. It represents a closed volume where the fluid flows through.

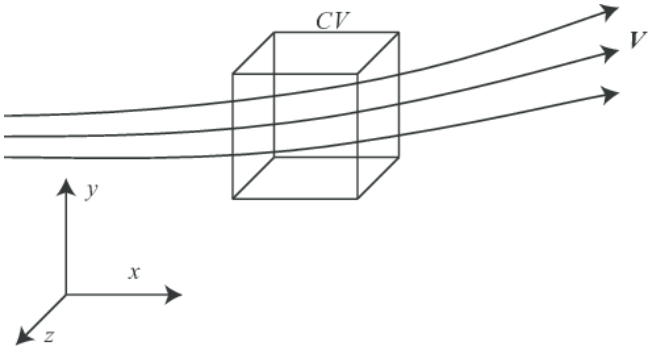

Figure 3.1: Example of a control volume [43]

3.1.1 Conservation of mass

Considering the closed control volume in Figure 3.1, according to the conservation of mass, the rate at which mass enters the system equals the rate at which mass leaves the system plus the accumulation of mass within the system. Being ρ and u_i the density and the velocity in the i-direction of a Cartesian coordinates system of the fluid, respectively, this law, also called the *continuity equation*, can be mathematically written as follows:

$$\frac{\partial \rho}{\partial t} + \frac{\partial (\rho u_i)}{\partial x_i} = 0 \tag{3.1}$$

Equation 3.1 represents a scalar equation in Cartesian coordinates valid for every fluid, both compressible and incompressible (it can be further simplified in the incompressible case).

3.1.2 Conservation of momentum

The conservation of momentum can be seen as the Newton's second law of motion for fluids and it expresses the conservation of the total momentum in the considered control volume if no external force is applied. In particular, it states that the rate of change of momentum of a fluid particle equals the sum of the forces on the particle. Mathematically, it is expressed as in Equation 3.2:

$$\frac{\partial (\rho u_i)}{\partial t} + \frac{\partial (\rho u_j u_i)}{\partial x_j} = -\frac{\partial p}{\partial x_i} + \frac{\partial \tau_{ij}}{\partial x_j} \tag{3.2}$$

where p indicates the pressure of the fluid and τ_{ij} the viscous stress tensor for Newtonian fluid, written as:

$$\tau_{ij} = 2\mu \left[\frac{1}{2} \left(\frac{\partial u_i}{\partial x_j} + \frac{\partial u_j}{\partial x_i} \right) - \frac{1}{3} \frac{\partial u_k}{\partial x_k} \delta_{ij} \right] \tag{3.3}$$

being μ the molecular viscosity and δ_{ij} the Kronecker delta.

3.2 Reynolds-Averaged Navier-Stokes equations (RANS)

As mentioned in subsection 1.1.1, the Reynolds number considered in this study is $Re \simeq 10^4$; in this range, the flow around the cylinder results turbulent.
In order to properly predict the evolution of turbulence, capturing its complexity and unsteadiness, an appropriate numerical model must be used. The first basic approach is to simplify the constitutive equations predicting only the statistical evolution of the turbulent flow. In particular, the *Reynolds Decomposition* is used; hence, each instantaneous quantity in Equation 3.1 and Equation 3.2 is written as a sum of two terms, as in Equation 3.4. The first one is the time-averaged value of the considered quantity, whereas the second term represents the fluctuation of the quantity around its mean value.

$$\phi(x_i, t) = \bar{\phi}(x_i) + \phi'(x_i, t) \tag{3.4}$$

where

$$\bar{\phi}(x_i) = \lim_{T \to +\infty} \frac{1}{T} \int_{t_0}^{t_0+T} \phi(x_i, t)\, dt \tag{3.5}$$

is the time-average term of the quantity $\phi(x_i, t)$, being t the time and T the averaging interval, whereas $\phi'(x_i, t)$ represents the fluctuation of $\phi(x_i, t)$ around $\bar{\phi}(x_i)$. In the case of unsteady flow, the time-average term is substituted by the ensemble average in Equation 3.6

$$\bar{\phi}(x_i) = \lim_{N \to +\infty} \sum_{n=1}^{N} \phi(x_i, t; n) \tag{3.6}$$

N being the number of terms of the ensemble.
Applying the Reynolds Decomposition to the quantities in Equation 3.1 and Equation 3.2 and averaging the equations in time, noting that the mean value of the fluctuation $\phi'(x_i, t)$ is zero, the Reynolds-Averaged Navier-Stokes (RANS) equations can be found.
Being $u_i(x_i, t) = \overline{U_i}(x_i, t) + \overline{u_i'}(x_i, t)$, the Navier-Stokes equations for an incompressible flow become:

$$\frac{\partial \bar{U}_i}{\partial x_i} = 0 \tag{3.7}$$

$$\rho \bar{u}_j \frac{\partial \bar{u}_i}{\partial x_j} = \frac{\partial}{\partial x_j} \left[-\bar{p}\delta_{ij} + \bar{\tau}_{ij} - \rho \overline{u_i' u_j'} \right] \tag{3.8}$$

where $\bar{\tau}_{ij}$ represents the mean viscous stress tensor calculated as:

$$\bar{\tau}_{ij} = 2\mu \left(\frac{\partial \bar{U}_i}{\partial x_j} + \frac{\partial \bar{U}_j}{\partial x_i} \right) \tag{3.9}$$

It is possible to notice a resemblance between the classic Navier-Stokes equations and the RANS equation; the only difference resides in the term $R_{ij} = -\rho \overline{u_i' u_j'}$, well known as the *Reynolds stress tensor*. It is a non-linear term containing the effect of the velocity fluctuations on the averaged equations; due to the presence of this symmetric tensor, 6 further terms are added to the system of equations. Hence, it is not possible to close the system and more equations need to be introduced in order to guarantee its closure and, consequentially, its solution.

3.2.1 Turbulence models

The problem of the closure of the system of equations mentioned in section 3.2 can be solved by introducing extra equations in the system.
The first approach of solution was given by Boussinesq [12] in 1877. His idea is based on the hypothesis that the Reynolds stresses are related to the mean velocity; R_{ij} can then be modeled introducing the proportionality constant $\nu_t > 0$, called turbulent eddy viscosity, as shown in Equation 3.10,

$$-\overline{u_i' u_j'} = \nu_t \left(\frac{\partial \bar{U}_i}{\partial x_j} + \frac{\partial \bar{U}_j}{\partial x_i} \right) - \frac{2}{3} k \delta_{ij} \tag{3.10}$$

where $k = \frac{1}{2} \overline{u_i' u_i'}$ is the turbulent kinetic energy and δ_{ij} is the Kronecker delta. This model assumes that the eddy viscosity is approximately isotropic, which may not be realistic for several flows.

Several turbulence models found their basis on the Boussinesq approximation with the purpose of predicting the evolution of turbulence flows; the one equation Spalart-Allmaras and the two equations $k - \varepsilon$ and $k - \omega$ models are typical examples of turbulence models implying the Boussinesq hypothesis mainly used in CFD. In this project, only the $k - \omega$ model will be presented, being one of the turbulence models analyzed in the present case, as it will be discussed in section 4.4.

$k-\omega$ turbulence model

The $k-\omega$ model aims to predict turbulent flows by means of two further partial differential equations for the turbulent kinetic energy, k, and the specific dissipation rate of turbulent kinetic energy into internal thermal energy, ω. In this model, the turbulent eddy viscosity is calculated as $\nu_t = k/\omega$.
For the incompressible flow case, the transport equations of k and ω are written as:

$$\begin{aligned} \frac{\partial k}{\partial t} + \overline{U_j}\frac{\partial k}{\partial x_j} &= P_k - \beta^* \omega k + \frac{\partial}{\partial x_j}\left[\left(\nu + \frac{\nu_t}{\sigma_k}\right)\frac{\partial k}{\partial x_j}\right] \\ \frac{\partial \omega}{\partial t} + \overline{U_j}\frac{\partial \omega}{\partial x_j} &= \frac{\gamma}{\nu_t}P_\omega - \beta\omega^2 + \frac{\partial}{\partial x_j}\left[\left(\nu + \frac{\nu_t}{\sigma_\omega}\right)\frac{\partial \omega}{\partial x_j}\right] + F_\omega \frac{1}{\omega}\frac{\partial k}{\partial x_j}\frac{\partial \omega}{\partial x_j} \end{aligned} \tag{3.11}$$

being

$$\begin{aligned} P_k &= \frac{\partial \overline{U_i}}{\partial x_j}\left[\nu_t\left(\frac{\partial \overline{U_i}}{\partial x_j} + \frac{\partial \overline{U_j}}{\partial x_i}\right) - \frac{2}{3}k\delta_{ij}\right] \\ P_\omega &= \frac{\partial \overline{U_i}}{\partial x_j}\left[\nu_t\left(\frac{\partial \overline{U_i}}{\partial x_j} + \frac{\partial \overline{U_j}}{\partial x_i}\right) - \frac{2}{3}k\delta_{ij}\right] \end{aligned} \tag{3.12}$$

In 1994, Menter [44] improved the model developing the Shear Stress Transport (SST) $k-\omega$ model. His purpose was to blend the accuracy of the $k-\omega$ model in the near-wall region, which makes the model directly usable in the boundary layer region up to the viscous sub-layer, with the free-stream independence of the $k-\varepsilon$ model in the far-field, avoiding the problem of excessive sensitivity to the inlet free-stream turbulence properties commonly encountered when using the $k-\omega$ model.

In the SST formulation of the model, ν_t is calculated as:

$$\nu_t = \frac{a_1 k}{\max\left(a_1\omega, \Omega F_2\right)} \tag{3.13}$$

where $a_1 = 0.31$, $\Omega = \sqrt{2\Omega_{ij}\Omega_{ij}}$ is the vorticity magnitude with $\Omega_{ij} = \frac{1}{2}\left(\frac{\partial \overline{U_i}}{\partial x_j} + \frac{\partial \overline{U_j}}{\partial x_i}\right)$ and $F_2 = \tanh\left[\left[\max\left(\frac{2\sqrt{k}}{\beta^*\omega y}, \frac{500\nu}{y^2\omega}\right)\right]^2\right]$, with y the wall distance.
The constants present in Equation 3.11 can be written as functions on the blending function

$$F_1 = \tanh\left\{\min\left[\max\left(\frac{\sqrt{k}}{0.009\omega y}, \frac{500\nu}{\omega y^2}\right), \frac{4k}{(\sigma_\omega)_2 CD_{k\omega} y^2}\right]\right\} \tag{3.14}$$

where

$$CD_{k\omega} = \max\left(2\frac{1}{(\sigma_\omega)_2}\frac{1}{\omega}\frac{\partial k}{\partial x_j}\frac{\partial \omega}{\partial x_j}, 10^{-20}\right) \tag{3.15}$$

Finally, the model constants can be found:

$\gamma = F_1\gamma_1 + (1-F_1)\gamma_2$	$\beta = F_1\beta_1 + (1-F_1)\beta_2$	$\beta^* = 0.09$
$\sigma_k = F_1(\sigma_k)_1 + (1-F_1)(\sigma_k)_2$	$\sigma_\omega = F_1(\sigma_\omega)_1 + (1-F_1)(\sigma_\omega)_2$	$F_\omega = 2(1-F_1)(\sigma_\omega)_2^{-1}$
$\gamma_1 = 0.5532$	$\beta_1 = 0.075$	$(\sigma_k)_1 = 2$
$\gamma_2 = 0.4404$	$\beta_2 = 0.0828$	$(\sigma_k)_2 = 1$
$(\sigma_\omega)_1 = 2$	$(\sigma_\omega)_2 = 1.17$	

Transition SST model

Due to the Reynolds range of interest in this project, it is important to correctly predict the boundary layer development and to evaluate transition onset from laminar to turbulent regime. For this purpose, the Transition SST turbulence model can be adopted.
The basic idea behind this model is to combine the SST $k-\omega$ model with two other transport equations, one for the intermittency and one for the transition onset criteria, in terms of momentum-thickness Reynolds number.
The transport equation for the intermittency, γ, is written as:

$$\frac{\partial(\rho\gamma)}{\partial t}+\frac{\partial\left(\rho U_j\gamma\right)}{\partial x_j}=P_{\gamma1}-E_{\gamma1}+P_{\gamma2}-E_{\gamma2}+\frac{\partial}{\partial x_j}\left[\left(\mu+\frac{\mu_t}{\sigma_\gamma}\right)\frac{\partial\gamma}{\partial x_j}\right] \tag{3.16}$$

having the transitional sources

$$\begin{aligned} P_{\gamma1}&=C_{a1}F_{\text{length}}\rho S\left[\gamma F_{\text{onset}}\right]^{c_{\gamma3}}\\ E_{\gamma1}&=C_{e1}P_{\gamma1}\gamma \end{aligned} \tag{3.17}$$

with S the strain rate magnitude, F_{length} an empirical correlation that controls the length of the transition region, $C_{a1}=2$ and $C_{e1}=1$.
Moreover, the destruction sources are:

$$\begin{aligned} P_{\gamma2}&=C_{a2}\rho\Omega\gamma F_{\text{turb}}\\ E_{\gamma2}&=C_{e2}P_{\gamma2}\gamma \end{aligned} \tag{3.18}$$

with $C_{a2}=0.06$ and $C_{e2}=50$.
To calculate the transition onset, the following functions are used:

$$\begin{aligned} Re_V&=\frac{\rho y^2 S}{\mu}\\ R_T&=\frac{\rho k}{\mu\omega} \end{aligned} \tag{3.19}$$

hence, F_{onset} and F_{turb} are found as:

$$F_{\text{onset }1}=\frac{Re_V}{2193Re_{\theta c}} \tag{3.20}$$

$$F_{\text{onset }2}=\min\left(\max\left(F_{\text{onset }1},F^4_{\text{onset }1}\right),2.0\right) \tag{3.21}$$

$$F_{\text{onset }3}=\max\left(1-\left(\frac{R_T}{25}\right)^3,0\right) \tag{3.22}$$

$$F_{\text{onset}}=\max\left(F_{\text{onset }2}-F_{\text{onset }3},0\right) \tag{3.23}$$

$$F_{\text{turb}}=e^{-\left(\frac{R_T}{4}\right)^4} \tag{3.24}$$

with y being the wall distance and $Re_{\theta c}$ the critical Reynolds number at which the intermittency starts to increase in the boundary layer, occurring upstream of the transition Reynolds number; the difference between the two Reynolds numbers is found from an empirical correlation.

Regarding the transition momentum thickness Reynolds number, $\tilde{Re}_{\theta t}$, its transport equation is written as:

$$\frac{\partial\left(\rho R\tilde{e}_{\theta t}\right)}{\partial t}+\frac{\partial\left(\rho U_j R\tilde{e}_{\theta t}\right)}{\partial x_j}=P_{\theta t}+\frac{\partial}{\partial x_j}\left[\sigma_{\theta t}\left(\mu+\mu_t\right)\frac{\partial R\tilde{e}_{\theta t}}{\partial x_j}\right] \tag{3.25}$$

where the source terms are defined as:

$$\begin{aligned} &P_{\theta t}=c_{\theta t}\tfrac{\rho}{t}\left(Re_{\theta t}-R\tilde{e}_{\theta t}\right)\left(1.0-F_{\theta t}\right)\\ &t=\tfrac{500\mu}{\rho U^2}\end{aligned} \tag{3.26}$$

with $c_{\theta t}=0.03$, $\sigma_{\theta t}=2$ and

$$F_{\theta t}=\min\left(\max\left(F_{\text{wake}}e^{\left(-\frac{y}{\delta}\right)^4},1.0-\left(\frac{\gamma-1/50}{1.0-1/50}\right)^2\right),1.0\right) \tag{3.27}$$

which can be found knowing:

$$\theta_{BL}=\frac{R\tilde{R}_\theta\mu}{\rho U} \tag{3.28}$$

$$\delta_{BL}=\frac{15}{2}\theta_{BL} \tag{3.29}$$

$$\delta=\frac{50\Omega y}{U}\delta_{BL} \tag{3.30}$$

$$Re_\omega=\frac{\rho\omega y^2}{\mu} \tag{3.31}$$

$$F_{\text{wake}}=e^{-\left(\frac{Re_\omega}{1E+5}\right)^2} \tag{3.32}$$

The boundary conditions for $\tilde{Re}_{\theta t}$ are zero flux at the wall, whereas at the inlet the boundary condition is given by an empirical correlation based on the inlet turbulent intensity.

3.3 Scale-resolving Simulation models (SRS)

Unlike turbulence models based on the RANS equations, the Scale-Resolving Simulation (SRS) models can directly resolve the motion of the largest eddies in at least a portion of the domain. The eddies which are smaller than the mesh size are modeled. Hence, these models can highly improve the accuracy of the solutions and must be considered in the present study.
The most known SRS models are the LES model and the Hybrid RANS-LES models.

3.3.1 Large Eddy Simulation (LES)

The Large Eddy Simulation (LES) model is the most common and known SRS model. The main idea behind this model is to resolve large turbulent structures in space and time everywhere in the flow; the only limitation resides in the mesh size. Thus, it follows that an appropriate grid refinement must be applied, as well as an accurate time-step size. The largest scales in the turbulent spectrum are very small, hence the mesh needs to be excessively refined, especially in the near wall region, in both the wall normal and parallel plane.
These requirements make the simulation computationally expensive; for this reason, the LES model has not been taken into account in this study.

3.3.2 Hybrid RANS-LES models

Several hybrid models have been developed in the past years with the purpose of avoiding the problems related to the LES model due to its high resolution requirements. These models aim to combine both RANS and LES approach; in particular, the goal is to resolve the attached wall boundary layer using RANS model, whereas the large detached regions are handled by the LES model, with a partial resolution of the turbulent spectrum in space and time.
In the present case, where the flow reaching a bluff body is simulated, the hybrid models represent a very interesting possibility to correctly predict the mixing in the wake behind the cylinder, avoiding the expensive resolution in the boundary layer needed by the LES model. For this reason, two hybrid models are analyzed in this study.

Scale-Adaptive Simulation (SAS)

Introducing the Von Kármán length scale, L_{VK}, into the turbulence equations, the Scale-Adaptive Simulation (SAS) model proposed by Menter et al. [22] can be found. This length scale is defined as the ratio between the first derivative of the velocity vector, U', divided by the second one, U'', as Equation 3.33 displays:

$$L_{VK} = \kappa \left| \frac{U'}{U''} \right| \tag{3.33}$$

with $\kappa = 0.41$ being the Von Kármán constant.
In particular, the derivatives are calculated as:

$$U' = \sqrt{2\, S_{ij} S_{ij}} \Rightarrow S_{ij} = \frac{1}{2}\left(\frac{\partial U_i}{\partial x_j} + \frac{\partial U_j}{\partial x_i}\right) \tag{3.34}$$

$$U'' = \sqrt{\frac{\partial^2 U_i}{\partial x_k^2}\frac{\partial^2 U_i}{\partial x_j^2}} \tag{3.35}$$

Thanks to this term, the model can adjust its length scale to already resolved scales in the flow; in this way, the eddy viscosity becomes low enough to allow the model to use the LES mode.
The main advantage of this model is that its RANS part is not affected by the grid refinement, however the model can remain in RANS mode in the region where the flow instability is not high enough.

Detached Eddy Simulation (DES)

The particularity of the Detached Eddy Simulation (DES) model is its dependency on the mesh refinement. Indeed, the switch between RANS and LES is based on the comparison of the turbulent length scale, L_t, with the grid spacing, $\Delta_{\max}$; the model goes from RANS to LES if $\Delta_{\max} < L_t$ as, in the equation of the turbulent kinetic energy, k, ε[1] becomes:

$$\varepsilon = \frac{k^{3/2}}{\min\left(L_t, c_{DES}\Delta_{\max}\right)} \tag{3.36}$$

[1]It represents the dissipation rate, calculated as $\varepsilon = \beta^* \omega k$, with β^* being the model coefficient.

It appears clear the importance of the grid refinement in the DES method; a common problematic encountered using this model is indeed the grid-induced-separation (GIS). If the mesh for an attached wall boundary layer is excessively refined and reaches the DES delimiter, the RANS solution can be affected and an artificial flow separation in that region can occur. To avoid this problem, some blending functions have been proposed in order to shield the boundary layers to the DES limiter. One of this function resulted in the creation of the Delayed Detached Eddy Simulation (DDES), the most common DES model in use, which is recommended by ANSYS FLUENT User's Guide [3] and it has been adopted in this project.

3.4 Direct Numerical Solution (DNS)

The Direct Numerical Solution (DNS) method is the most expensive one as it predicts the turbulent flows without averaging the Navier-Stokes equations. Thus, all the turbulent scales in the model are fully resolved.
Obviously, the mesh refinement must be chosen accordingly; this leads to high computational costs even at low Reynolds numbers, since the number of mesh points goes as Re^3.

Figure 3.2 displays a comparison between the resolution of turbulence flows given by the LES and DNS models; all the smaller scales are resolved by the DNS model, whereas only the largest ones can be captured by the LES model.

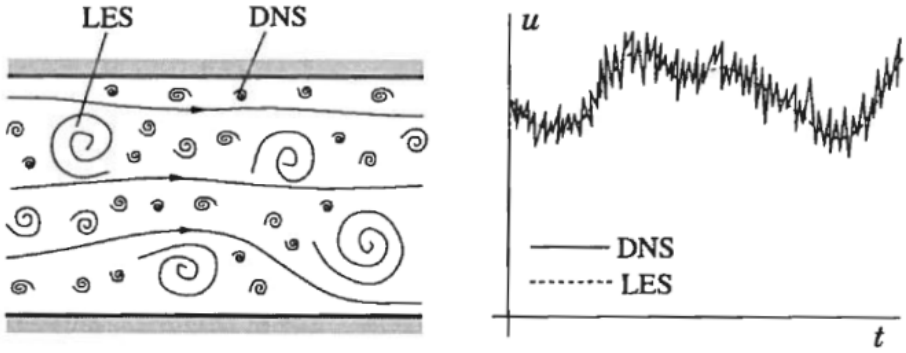

Figure 3.2: Comparison between LES and DNS resolution of turbulent scales (left) and time-dependent velocity (right) [25]

3.5 Numerical solution

As stated at the beginning of this chapter, the CFD methodology relies on numerical techniques in order to solve the governing equations described in the previous sections. In particular, the differential equations are approximated by a discretization in space and time, hence all the continuous equations are transferred to their discrete counterpart. For this purpose, the object of study must be divided into several discrete cells, which will form the new control volumes analyzed by the governing equations. This leads to the formation of the mesh, which will highly affect the solution of the model. It appears clear that a very fine mesh will better approximate the whole model and will produce a

more reliable solution. However, the grid generation should always be kept as a balancing between accuracy and computational cost, which tends to increase for finer mesh, as it will be shown in section 4.3.
There are three main types of discretization methods:

- **Finite Volume Method (FVM):** after having discretized the domain into a finite number of control volumes, the governing equations are applied to each control volume. Volume integrals in the partial differential equation that contain a divergence term are first converted to surface integrals, using the divergence theorem, and then evaluated as fluxes at the surfaces of each finite volume, which are conserved into the volume. This method is the one used in this study.

- **Finite Element Method (FEM):** the domain is divided into discrete volumes, called finite elements, typically triangles or quadrilaterals for 2D geometries and tetrahedral or hexahedra for 3D geometries. The method approximates the unknown functions over the domain and then the simple equations that model these finite elements are assembled into a larger system of equations modeling the entire problem.
  This model is more stable than FVM, however it requires more memory.

- **Finite Difference Method (FDM):** the partial differential equations are converted into a system of equations that can be solved by matrix algebra techniques and the derivatives are approximated by finite differences. This method is used only in few specialized codes.

3.5.1 Spatial and temporal discretization

For transient problems, such as the one in this project, both spatial and temporal discretization are required. Since the explicit time integration is only available using the explicit density-based solver, which is not considered in the present study, as it will be discussed in subsection 3.5.2, only the implicit time integration will be adopted. The basic idea is to evaluate the temporal evolution of a variable ϕ, $F(\phi) = \frac{\partial \phi}{\partial t}$, at the future time level:

$$\frac{\phi^{n+1} - \phi^n}{\Delta t} = F\left(\phi^{n+1}\right) \tag{3.37}$$

The above equation is resolved at each time level to find the value of the quantity at the next time level, ϕ^{n+1}, before moving to the next time step.
The implicit scheme can have first- or second-order accuracy; in this project, in order to have a more reliable solution, the second-order accuracy has been imposed.

On the other hand, the upwind scheme is used for the spatial discretization. Discrete values of the scalar quantity ϕ are evaluated at the cell center, however face values are also needed for the convection terms and they are interpolated from the cell center values. For this purpose, the upwind scheme is adopted, hence the face value is derived from quantities in the cell upstream relative to the direction of the normal velocity.
Several upwind schemes are available in Ansys Fluent; in this study, the second-order and the bounded central differencing scheme are implemented, as they are the ones recommended for the SRS turbulence models is use.

3.5.2 Solution Algorithm

The numerical methods implemented in Ansys Fluent are the pressure-based solver and the density-based solver. The latter is generally used for high-speed compressible flows, hence, in this study, where the flow velocity simulated is quite low ($U_\infty < 5$ m/s), the pressure-based approach has been implemented.

While the velocity field is obtained from the momentum equations, the pressure field is extracted by solving a pressure or a pressure correction equation obtained by manipulating continuity and momentum equations. Moreover, the individual governing equations for the solution variables are solved one after another and then they are decoupled from the other equations. The main algorithm in use are SIMPLE, SIMPLER, SIMPLEC and PISO.

SIMPLE Algorithm

The Semi-Implicit Method for Pressure Linked Equations (SIMPLE) is extensively used to solve the Navier-Stokes equations. In this method, the pressure field is guessed to solve the discretized momentum equations; it leads to the velocity component in the x- and y-direction. Then, by means of a correction pressure given by the difference between the correct velocity and the guessed one, the correct velocity field is found, satisfying the continuity equation.
The SIMPLER and SIMPLEC algorithms are evolutions of the SIMPLE method.

PISO Algorithm

The Pressure-Implicit with Splitting of Operators (PISO) algorithm is an extension of the SIMPLE algorithm using one predictor step and two corrector steps.
Firstly, the pressure field is guessed and used to solve the discretized momentum equation, in order to get the velocity components. Afterwards, two correction factors are applied to the velocity and pressure field, satisfying both the continuity and the momentum equation.

As it will be extensively discussed in section 4.5, in this project a very small time-step will be chosen to solve the created model; Ansys Fluent User's Guide [3] recommends to adopt the PISO algorithm in case of large time-steps, however it could lead to an high increase in the computational cost for problems requiring small time-steps. For this reason, the SIMPLE algorithm, which is also the default choice in Ansys Fluent for the considered turbulence models, has been adopted in this study.

Chapter 4

Validation of the computational model

In order to build a reliable computational model of a 3D cylinder, the validation of the present CFD code was first conducted.
This chapter describes how the computational model was validated by comparing the numerical and the experimental results obtained during a VIV experiment conducted in the wind tunnel of the University of Liège.
Several parameters have been considered, such as the drag and lift coefficient, the Strouhal number and the pressure coefficient; they have all been compared with the experimental results and with results obtained during previous studies by other researchers.

To build a reliable and efficient model, five main steps were conducted:

1. Grid quality check
2. Sensitivity analysis of the mesh
3. Choice of the best turbulence model to solve the present case
4. Study of the time-step size to be used
5. Reduction of the spanwise length of the cylinder

All these steps will be presented and discussed in this chapter after having introduced the model's geometry and having analyzed the experimental results.

4.1 Determination of the model geometry

Before discussing the analysis of the numerical results more deeply, the geometry of the model must be presented.
Since some experimental data were used to validate the computational model, it was decided to numerically recreate the same model of the cylinder adopted during the VIV experiment in the University of Liège. Hence, as for the experimental cylinder, a diameter equal to $D = 0.1$ m has been imposed. Moreover, as a first approach, like in the experiment, it was decided to let the cylinder's spanwise length fit the length of the wind tunnel of the University of Liège ($L \simeq 1.5$ m), which has been rounded to 1.5 m to get a spanwise length exactly equal to $15D$.
As it will be discussed in section 4.6, the cylinder's length will then be reduced to a value of πD and the results will be compared with the ones obtained using the original model; this choice was made to decrease the high computational cost needed for 3D simulations.

Furthermore, in order to have a good comparison between the computational and the experimental results, the latters have first been analyzed, thus the incoming flow velocity and turbulent level have been determined and the useful parameters (Strouhal number and pressure coefficient) have been extracted.

4.1.1 Analysis of the experimental results

As mentioned, the available experimental results were obtained during a VIV experiment conducted in the wind tunnel of the University of Liège. This is a typical example of experiment using an aeroelastic cylinder; the latter was indeed attached to springs to recreate a cylinder free to move, as Figure 4.1 shows.

Figure 4.1: Experimental test rig used in the wind tunnel of the University of Liège

The interaction between the incoming flow and the structure can induce the vibration of the cylinder, which can be amplified reaching the lock-in condition, as explained in section 1.2. The aim of this project was indeed to analyze the behavior of the cylinder within the lock-in region, hence the vibration's amplitude, the pressure coefficient and the velocity in wake behind the body were registered. In particular, a Pitot-tube was installed far from the body to capture the velocity components of the flow in the wake region and 36 equally-distanced taps were positioned at the mid-span section of the cylinder to get the unsteady pressure distribution and, consequentially, the temporal evolution of the pressure coefficient.
All data were measured synchronously at 300 Hz and 9000 samples were registered. The incoming incident air flow velocity lies in a range of $U_\infty = [1.48, 9.1]$ m/s; in particular, 29 different wind speeds were tested. This leads to a Reynolds number in the range of $Re \simeq [1.01 \cdot 10^4, 6.2 \cdot 10^4]$, calculated using Equation 1.1 and considering air at the sea level condition (i.e. $\rho = 1.225$ kg/m^3 and $\mu = 1.7894 \cdot 10^{-5}$ Pa·s). Moreover, a low oncoming turbulence level was tested ($\simeq 0.2\%$).

The progression of the dimensionless vibration's amplitude of the cylinder (represented by A, the standard deviation of the vibration's amplitude in the cross-flow direction, non-dimensionalized by the cylinder's diameter, D) for different wind speeds is displayed in Figure 4.2. It is possible to notice an high increase in A/D in the range $U_\infty \simeq [3.45, 4.7]$ m/s; the lock-in condition is indeed reached. The strongest vibrations are recorded at a velocity of 4.282 m/s, where the maximum amplitude approaches the value of 0.038 m (almost 40% of one cylinder's diameter).

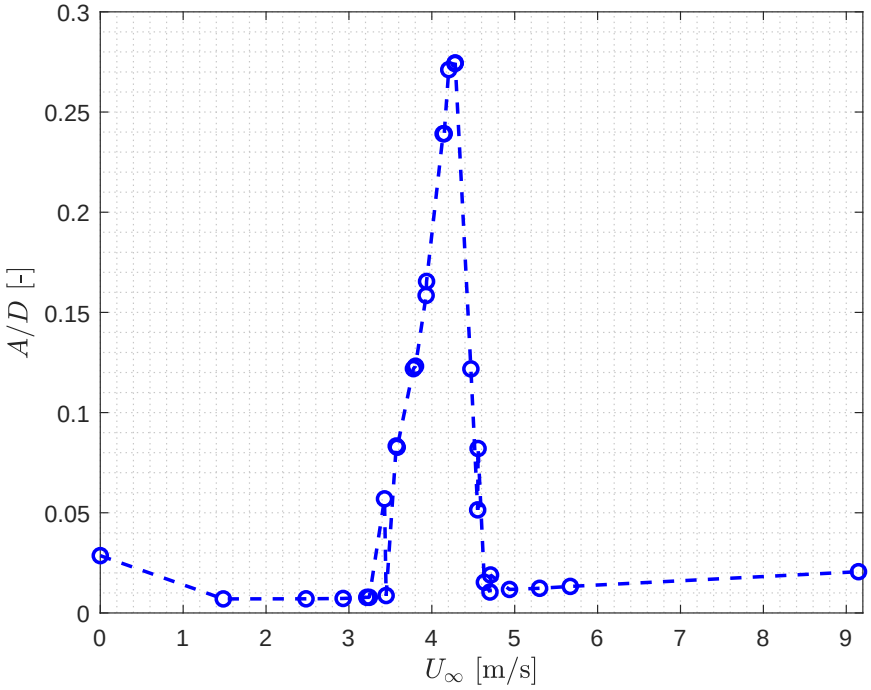

Figure 4.2: Evolution of the non-dimensional amplitude of vibration vs. free stream velocity obtained from the experimental data

As described in section 1.2, when the lock-in condition is reached, the structure takes control of the vortex shedding phenomenon, hence the frequency of vortex shedding does not follow the Strouhal relation anymore and it is locked to a certain value. In this case, the frequency of the cylinder's vibration, f, which equals the vortex shedding frequency, f_s, was found to be 7.07 Hz.
As mentioned in section 1.2, the lock-in condition is practically a resonance condition; strong vibrations of the body are registered at a frequency equal to its natural frequency, f_n. This can be proven by looking at the Fast Fourier Transform of the time response of the cylinder during the wind-off test ($U_\infty = 0$ m/s).

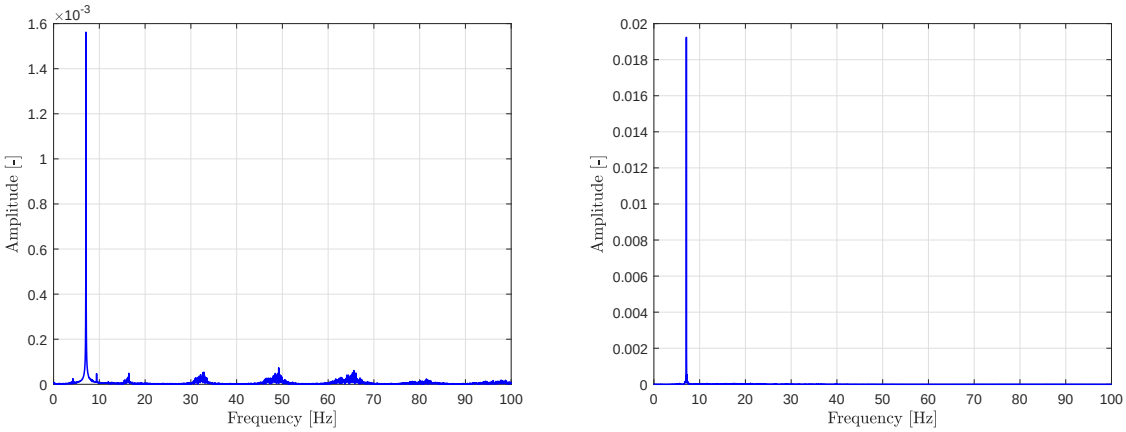

(a) $U_\infty = 0$ m/s (b) $U_\infty = 4.282$ m/s

Figure 4.3: Fast Fourier Transform of the cylinder's time response at two different wind speeds from the experimental data

Figure 4.3a shows the aforementioned FFT, where a main peak is observed at a frequency equal to 7.07 Hz, which then represents the natural frequency of the system. The same peak is also recorded in the FFT of the cylinder's time response performed at the point of maximum oscillations amplitude ($U_\infty = 4.282$ m/s), as visible in Figure 4.3b. Therefore, in the latter case, the cylinder vibrates with a frequency exactly equal to the body's natural frequency.

In order to understand when the onset of the VIV phenomenon occurs, the FFT of the wake velocity component along the y-direction (same direction of the cylinder's oscillations) can be calculated. The main frequency content in the FFT represents the frequency of vortex shedding, which should theoretically follow the Strouhal relation in Equation 1.2.
Figure 4.4 displays the variation in the vortex shedding frequency found from the experimental data at each wind speed tested. Moreover, the natural frequency of the body is also presented as well as the theoretical shedding frequency calculated using Equation 1.2.

It is possible to notice from Figure 4.4 that the lock-in condition is reached in the range $U_\infty = [3.45, 4.71]$ m/s, where the vortex shedding frequency becomes equal to the cylinder's natural frequency. On the other hand, the vortex shedding frequency for the other wind speeds tested approaches the theoretical values.

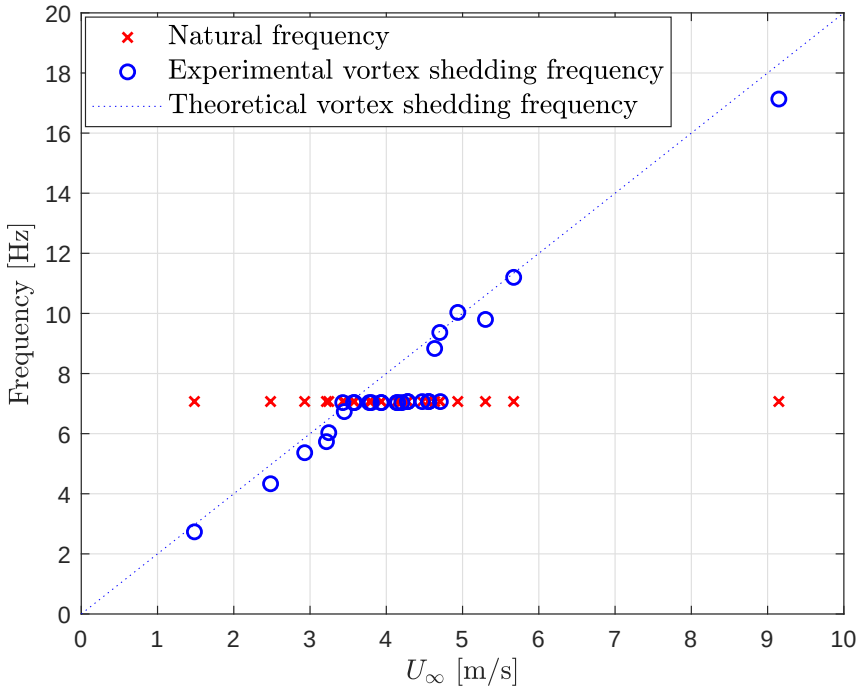

Figure 4.4: Variation of the experimental and theoretical vortex shedding frequency for different wind speeds

The Strouhal number of the present case can be evaluated by noticing that the critical VIV velocity, defined as the airspeed at which the lock-in phenomenon starts, is $U_\infty \simeq 3.45$ m/s ($Re \simeq 2.4 \cdot 10^4$). Thus, recalling Equation 1.2, the Strouhal number can be calculated as follows:

$$St = \frac{f_s \cdot D}{U_\infty} = \frac{7.07 \cdot 0.1}{3.45} \simeq 0.2049 \tag{4.1}$$

The latter approximates very well the theoretical Strouhal number of 0.2, typical value found in the Reynolds range of interest.

Furthermore, the evolution of the unsteady pressure coefficient was obtained; in order to have an estimation of the C_p, the time-average pressure coefficient at different locations around the mid-span section of the cylinder (each location corresponds to the location of the pressure tap) has been calculated in MATLAB using the function `mean`.
In order to recreate the typical C_p curve showed by previous researchers, like the one in Figure 1.7, the position of the pressure taps has been rearranged; each tap's location corresponds to a certain value of the angle θ visible in Figure 4.5. θ is equal to zero at the leading edge of the cylinder with an increasing value moving clockwise around the cylinder's section. The small red circles in Figure 4.5 represent the pressure taps location.

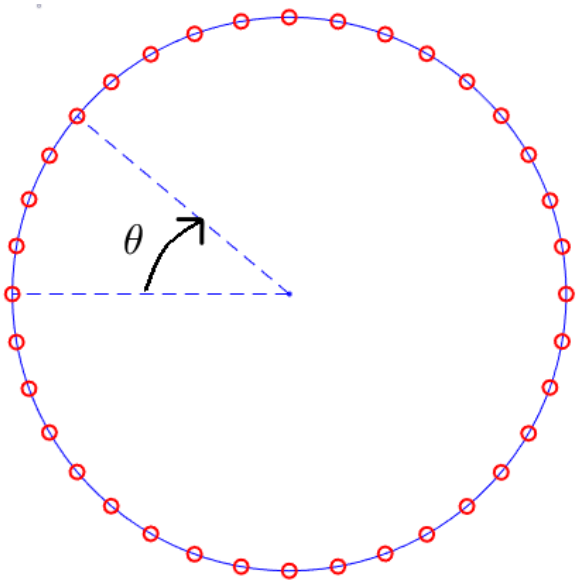

Figure 4.5: Location of the pressure taps at the mid-span section of the cylinder

Figure 4.6 displays one example of the variation of the mean pressure coefficient for θ lying in a range of $[0^o, 180^o]$; this graph has been obtained from the experimental data relative to a free-stream velocity value of 2.4823 m/s ($Re \simeq 1.7 \cdot 10^4$). The value of pressure coefficient at the leading edge is equal to 1, indicating the stagnation point. Then, it is possible to notice a drop in C_p until a minimum value occurring at $\theta = 60^o$, which is identified as θ_{sep}. Finally, the base pressure coefficient is reached at $\theta = 90^o$; its value is approximately $C_{pb} \simeq -0.763$.
The aforementioned experimental values of St, θ_{sep} and C_{pb}, as well as numerical and experimental values obtained by other researchers, will be used to validate the computational model built in this project. Furthermore, lift and drag coefficients of the present numerical model will be extracted and compared with the results from previous works.

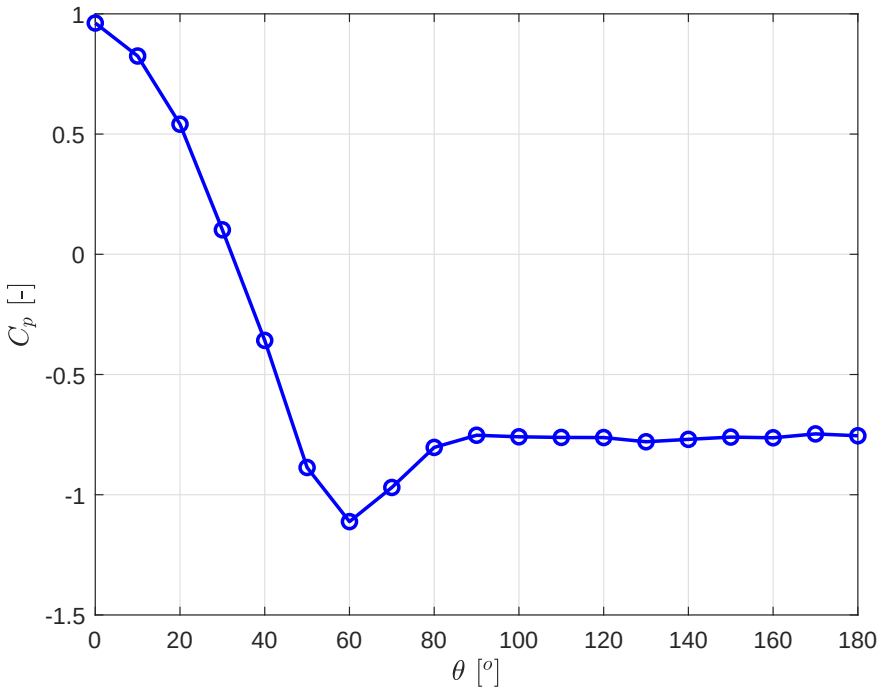

Figure 4.6: Variation of the experimental pressure coefficient obtained at the mid-span cylinder's section vs. θ at $Re \simeq 1.7 \cdot 10^4$

4.2 Determination of domain and grid type

Once the geometry of the cylinder is set and the experimental results analyzed, the model can be created using ANSYS WORKBENCH. Particular attention must be given to the size of the domain, which defines the environment surrounding the cylinder, location of the flow investing the body. In order to have a good resolution of the wake region behind the cylinder, it was decided to extend the domain up to $20D$ downstream of the body. Moreover, $10D$ separates the cylinder from the inlet location, as well as from the upper and lower boundary. As mentioned in section 4.1, $15D$ is the extension of the domain in the spanwise direction (it takes the whole cylinder's length and it will be further decreased to reduce the computational cost of the simulation).
Figure 4.7[1] displays a graphical representation of the domain sizes used in this project, $30D$x$20D$x$15D$. The choice of the size along the x- and y-axis was made to lie in the range of values adopted by previous researches (L_x=[$20D$, $65D$], L_y=[$10D$, $50D$]) [38] [41] [51] [52], which was proven to give reliable results.

[1]Please note that this is not a representation of the shape of the domain used in the project and it is only meant to visualize the sizes chosen.

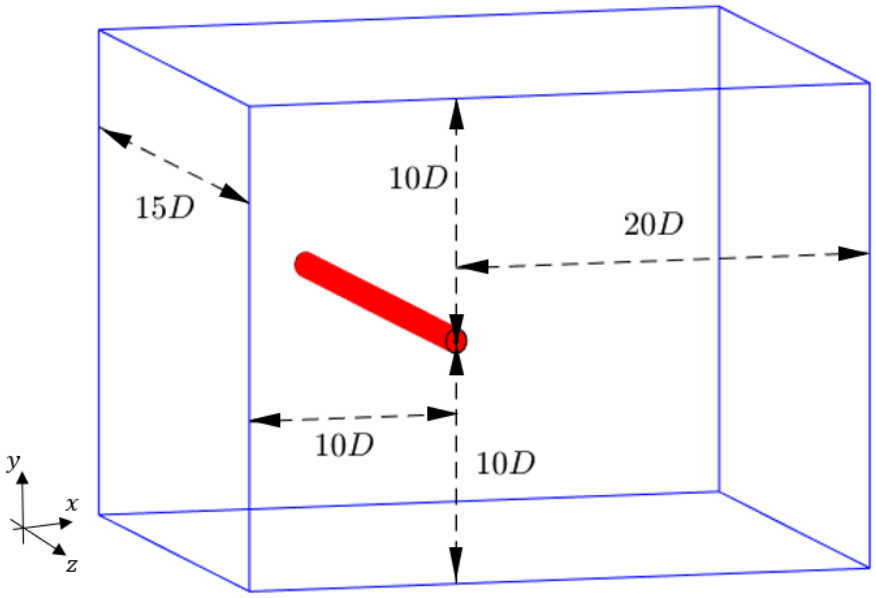

Figure 4.7: Representation of the domain size used in this study

After the definition of the domain size, the following step is the mesh generation. A first analysis of the grid quality was made before proceeding with the study of the mesh refinement.

4.2.1 Grid quality check

It was first decided to simplify the problem by generating a 2D model, a section of the cylinder in the $x-y$ plane. Three different grid types have then been built and compared to evaluate the mesh quality in the $x-y$ plane. For this purpose, some quality parameters have been observed; they are listed below:

- Aspect ratio: It represents the ratio between the element length and its width. It is ideally equal to 1 for perfect equilateral triangles or squares in case of triangular or quadrangular meshes, respectively.
- Jacobian ratio: It is a measure of the distortion of the element, being the ratio of the maximum to the minimum value of the Jacobian determinant. In the ideal case, it is equal to 1.
- Orthogonal quality: It lies in a range of [0, 1], with 1 being the best case, and it shows how close the angles between adjacent element faces (or adjacent element edges) are to some optimal angles (depending on the relevant topology).
- Skewness: It is defined as the difference between the shape of the cell and the shape of an equilateral cell of equivalent volume, hence it should be kept as close to zero as possible.

It was decided to use only quadrangular (or hexahedral, in the 3D case) elements; this was done to build a perfectly structured grid. Hence, the unstructured grid case was not considered in this study.

For the case of interest, two different domain geometries could be used, the circular and the rectangular one. In order to respect the domain sizes stated in section 4.2, a semi-circular domain having a circle radius of $10D$ was first built, as Figure 4.8 displays.

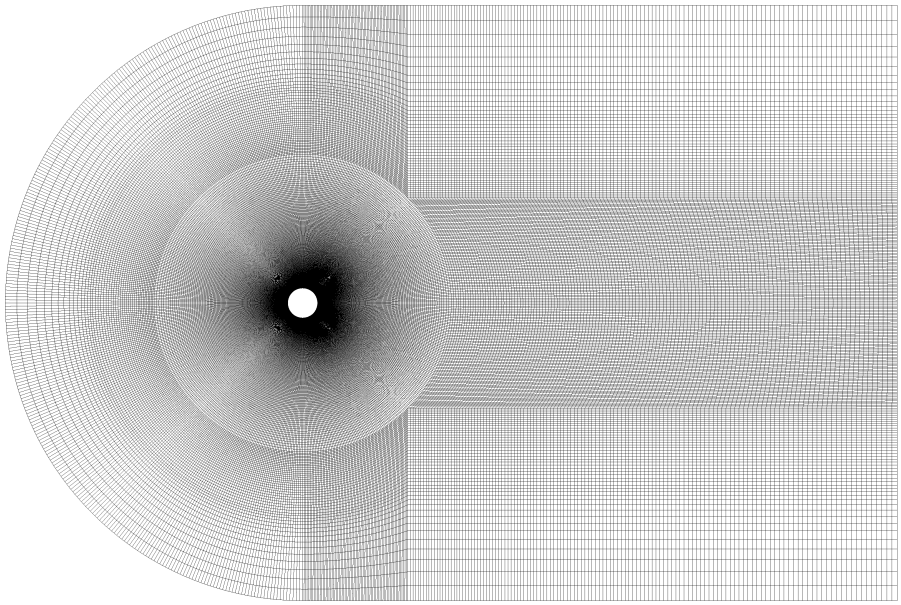

Figure 4.8: Representation of the semi-circular domain with an O-grid mesh

Thanks to this domain geometry, an O-type grid could be created, as Figure 4.8 clearly shows; this is a typical grid used for simulations dealing with circular cylinders.
In order to well capture the flow in the boundary layer, the element size has been biased towards the edges of the domain to have smaller elements in the proximity of the body, gradually increasing the element size moving away from it. Similar approach has been used in the wake region downstream of the cylinder, where very small elements are needed to resolve the small turbulent scales present in that zone.

The same methodology has then been applied to the rectangular domain. In this case, two different grids have been tested; in both grids, visible in Figure 4.9, a square has been created around the cylinder to ensure the correct refinement close to the body, however, in the grid in Figure 4.9b, the edges of the square have been rounded to smoothen the transition from the circular shape of the cylinder to the rectangular shape of the domain. Moreover, the grid in Figure 4.9b presents a perfect O-type mesh in the region close to the cylinder, as a circle was drawn around it.

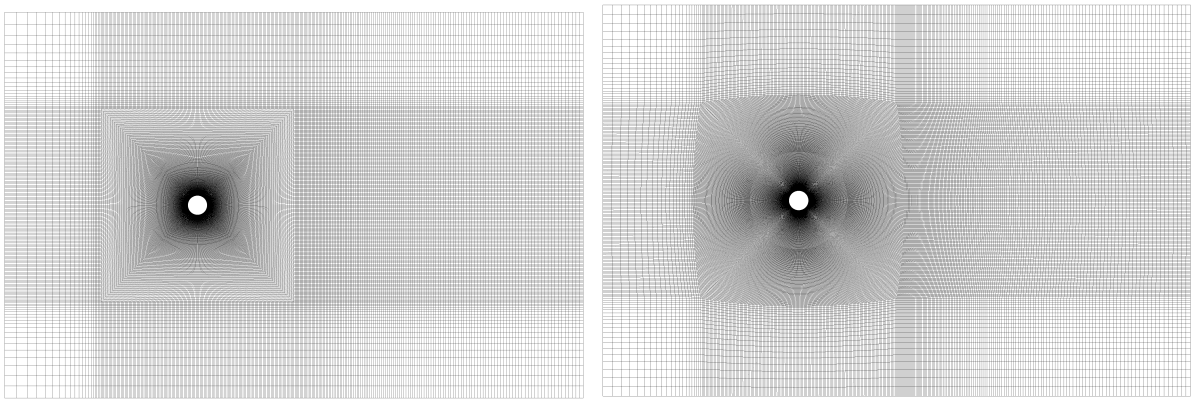

(a) First grid type with rectangular domain (b) Second grid type with rectangular domain

Figure 4.9: Representation of the two different grid types created using a rectangular domain

The comparison between the quality parameters of the three grids is visible in Table 4.1. In order to have a good comparability between them, the same mesh refinement has been applied to all the grids before the acquisition of the parameters.
In Table 4.1, the semi-circular domain with an O-grid is labeled as "Grid 1", whereas the grids in Figure 4.9a and Figure 4.9b are labeled as "Grid 2" and "Grid 3", respectively.

Table 4.1: Comparison between quality parameters of the three grids created

Quality parameters	Grid types		
	Grid 1	Grid 2	Grid 3
Aspect ratio [-]	6.8454	24.157	6.8762
Jacobian ratio [-]	0.98632	0.99238	0.98587
Orthogonality quality [-]	0.99265	0.95737	0.98899
Skewness [-]	0.032793	0.13183	0.052177
Number of elements [-]	1717000	1744500	1744500

The values of the quality parameters in Table 4.1 are the average values over all the elements in the models. It is possible to notice that the values closest to the ideal case are obtained in "Grid 1", whereas "Grid 2" reports the worst values among the three grids, except for the Jacobian ratio, slightly higher than in the other two cases. In general, "Grid 1" and "Grid 2" show very good results; the Aspect ratio of $\simeq 6.85$ is accepted for this case as it is mainly due to the cells far away from the cylinder having a rectangular rather than quadrangular shape. Being close to the domain's edges, they do not affect the correct resolution of the flow around the body.
Furthermore, Table 4.1 displays the number of elements present in the three grids. As the same mesh refinement was applied, the same number of elements is expected in "Grid 2" and "Grid 3", however, due to the shape of the domain in "Grid 1" (a rectangle with two rounded corners instead of a full rectangle), a lower value is observed. There is a reduction of $\simeq 1.58\%$ in the number of elements with respect to the other two grids, which becomes even more important in terms of computational cost when considering a 3D domain of similar shape. For this reason and for the high quality of the grid, as shown by the values of the parameters in Table 4.1, "Grid 1" has been chosen to proceed with further calculations.

4.3 Mesh refinement analysis

During the initial step of the mesh refinement analysis, it was decided to first simulate the simplified 2D section in Figure 4.8. Moreover, a laminar flow around the static cylinder was supposed: these choices were made to ensure a first reliable solution of the simplified model and a correctly running simulation, before proceeding with the complex 3D turbulent case. Hence, a first grid refinement in the $x - y$ plane was conducted using the 2D model in Figure 4.8.

4.3.1 Analysis of the 2D laminar case

A Reynolds number equal to 40 was first assumed: as mentioned in subsection 1.1.1, a pair of two vortices is expected downstream of the cylinder invested by a flow at this Reynolds number.
The incoming flow velocity was supposed to be $U_\infty = 1$ m/s, thus, recalling Equation 1.1, for the considered cylinder's diameter of $D = 0.1$ m, a flow kinematic viscosity of $\nu = 0.0025$ m^2/s must be imposed to get $Re = 40$.

In order to correctly set up the simulation in Ansys Fluent, the following boundary conditions must be enforced:

- Inlet: being the location where the flow enters the domain, the flow velocity at the inlet is imposed to be equal to the speed of the fluid, which flows in the direction of and parallel to the x-axis.
- Outlet: at the outlet location, where the flow exits the domain, the static pressure is imposed to be equal to the atmospheric one[2].
- Wall: at the walls present in the model (the boundaries of the domain and the cylinder's wall) a no-slip condition is enforced to ensure a zero velocity of the fluid relative to the boundary.

A first set of steady simulations using different mesh refinements were run and the evolution of the drag coefficient for an increasing value of the number of elements present in the model was registered, as Figure 4.10 displays. During all the simulations, it was ensured that the convergence of the calculation was achieved when all the residual values became lower than 10^{-6}.

[2]As Ansys Fluent deals with differential pressures, a gauge pressure of 0 Pa is imposed.

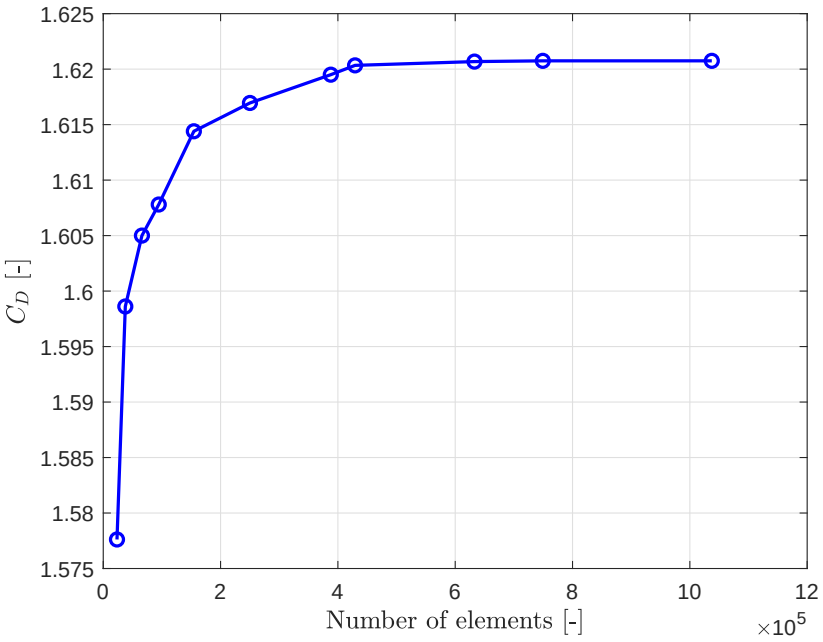

Figure 4.10: Evolution of the steady drag coefficient vs. number of elements at $Re = 40$

It is possible to notice that the steady drag coefficient tends to increase for higher numbers of elements of the system, until reaching a value equal to 1.62, corresponding to a model made by 429270 elements. Afterward, the C_D appears independent of the number of elements of the model. Since the computational cost of the simulation tends to increase when the number of elements in the system raises, it is possible to conclude that the best model for the current case is the one having the lowest number of elements required for the C_D convergence, thus 429270 elements. This gives a first idea of the refinement needed in the $x - y$ plane; the mesh will then be further refined in the wake and in the boundary layer region, in order to well capture the flow in these zones at high Reynolds numbers.

Moreover, in order to check the resolution given by the used model, the flow streamlines downstream of the body can be observed. A picture similar to the one in Figure 4.11 is expected, where the upper Von Kármán vortex is clearly visible.

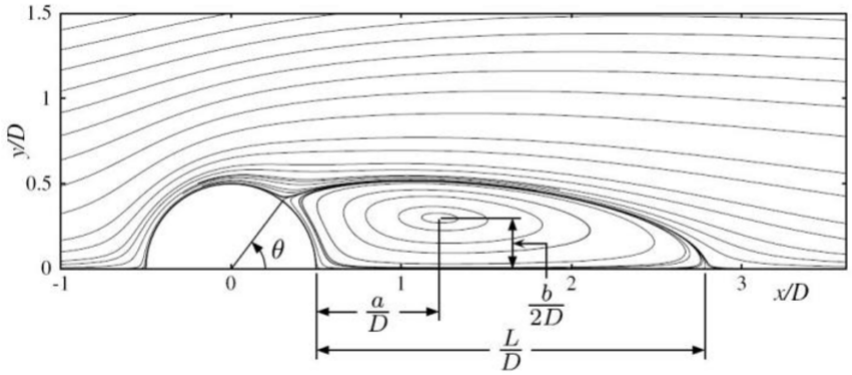

Figure 4.11: Streamlines of the flow downstream of a circular cylinder at $Re = 40$ [4]

The variables θ and a, b, L define the angle of separation and the size of the vortex, respectively. As displayed in Table 4.2, the values found in this project show a good comparison with the ones obtained by other researchers.

Table 4.2: Comparison between the flow vortex sizes downstream of a static circular cylinder at $Re = 40$

Researchers	C_D [-]	θ [^{o}]	a/D[-]	b/D [-]	L/D [-]
Asyikin [4]	1.6	49.5	0.73	0.6	2.27
Berthelsen and Faltinsen [6]	1.59	53.9	0.72	0.6	2.29
Calhoun [16]	1.62	54.2	-	-	2.18
Fasel and Linnick [23]	1.54	53.6	0.72	0.6	2.28
Herfjord [34]	1.6	51.2	0.71	0.6	2.25
Russel and Wang [57]	1.6	53.1	-	-	2.29
Xu and Wang [62]	1.66	53.5	-	-	2.21
Present study	1.62	53.1	0.69	0.59	2.19

Eventually, the streamlines graph found in this project is available in Figure 4.12, which clearly shows the two Von Kármán vortices.

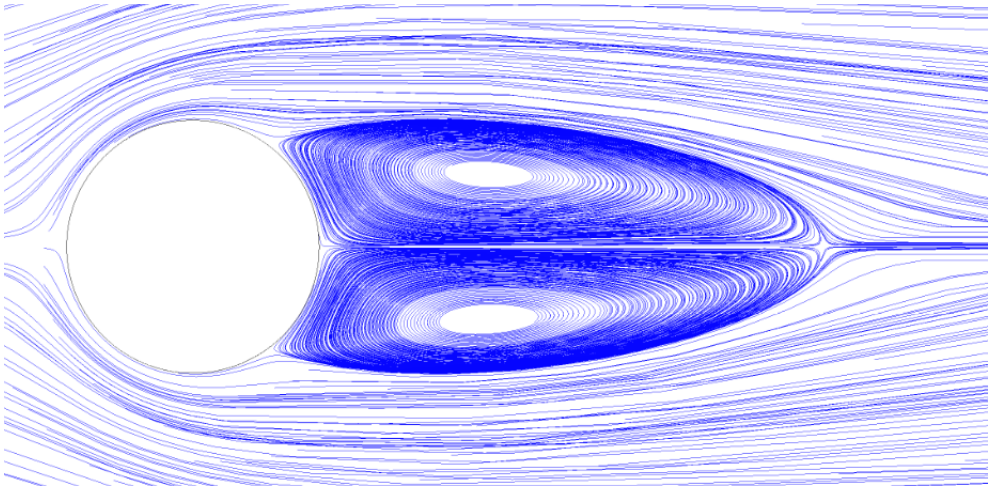

Figure 4.12: Visualization of the Von Kármán vortices in the wake of a flow reaching a circular cylinder at $Re = 40$

Transient case

Since the steady simulation was proven to give reliable results, a set of 2D transient laminar simulations was then run. In this case, the total number of time-steps was set to 1500. As recommended by ANSYS FLUENT User's Guide [3], around 20 time-steps should be set in one period of vortex shedding to properly capture the shedding mechanism, hence a rough estimation of the vortex shedding period was first calculated using Equation 1.2, setting the Strouhal number to the value found by Williamson [63] for the Reynolds numbers of interest. The time-step size can then be obtained accordingly for different Reynolds numbers in the range [60, 180], setting exactly 20 time-steps per one vortex shedding period.
In order to ensure a fast onset of the shedding process, a small flow instability was added by imposing an initial flow velocity of 0.1 m/s in the y-direction.

An example of the typical time variation of the lift coefficient observed during these unsteady simulations is available in Figure 4.13, where, after a first transient part, several stable vortex shedding periods are present.

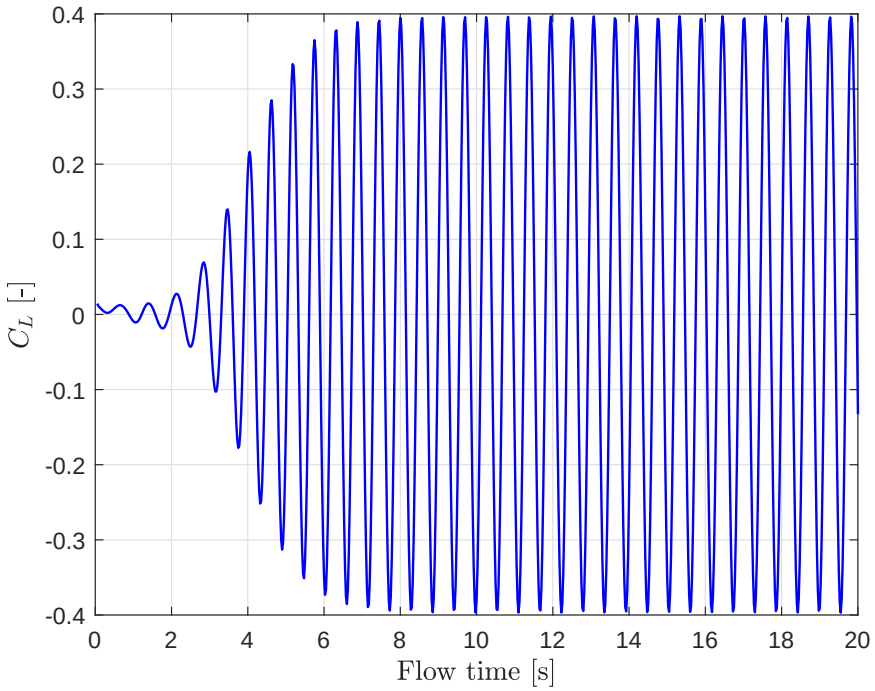

Figure 4.13: Time variation of the lift coefficient of a static circular cylinder invested by a flow at $Re = 120$

Calculating the Fast Fourier Transform (FFT) of the C_L curve, neglecting the first transient part, the frequency of vortex shedding can be obtained. Then, the Strouhal number can be found via Equation 1.2.
The Strouhal numbers determined in this study when the Reynolds number varies in the range [60, 180] are compared in Figure 4.14 with the results obtained by the following researchers in the Reynolds range of interest[3]:

- Norberg [50]: $St = 0.2663 - 1.019/\sqrt{Re}$
- Roshko [55]: $St = 0.2175 - 5.106/Re$
- Williamson [63]: $St = -3.3265/Re + 0.1816 + 1.6 \cdot 10^{-4} \cdot Re$

[3]They interpolated their results to get a numerical equation of the Strouhal number as a function of the Reynolds number, $St(Re)$.

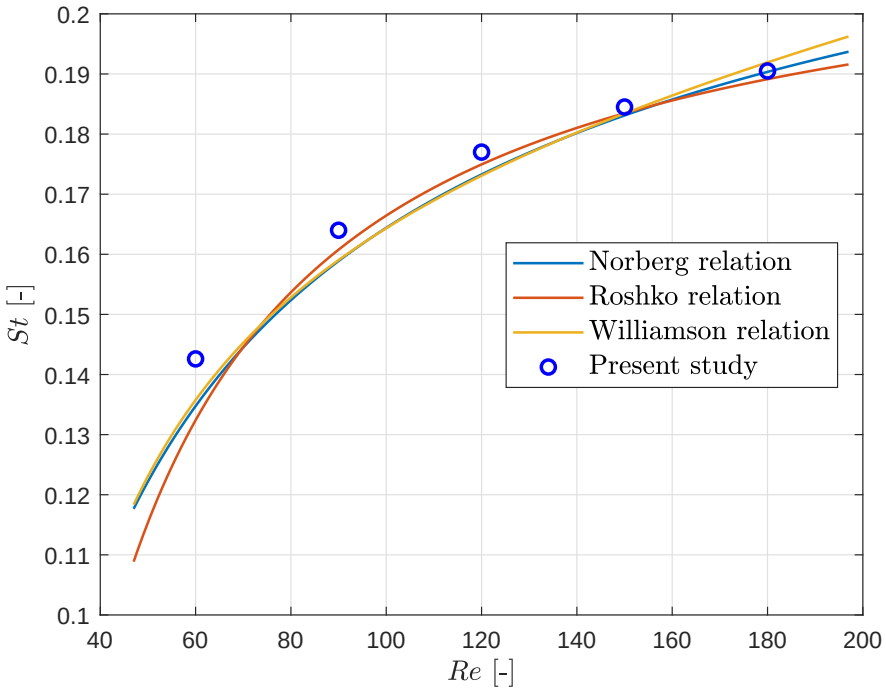

Figure 4.14: Comparison between $St(Re)$ obtained in this and in previous studies for the case of laminar flow reaching a circular cylinder

The present value of the Strouhal number seems to approach very well the one obtained by the aforementioned researchers at higher Reynolds numbers, however it tends to have a slightly bigger value at lower Re (a maximum error of $\simeq 7.5\%$ is found at $Re = 60$ with respect to the curve from Roshko [55]). Since only a small difference is observed, it can be concluded that the present simulations give a good and reliable representation of the laminar flow reaching a 2D cylinder, hence this case can be considered as validated.

4.3.2 Analysis of the 3D turbulent case

After having proven the reliability of the simplified 2D model, the 3D domain was then simulated. The Reynolds number was also highly increased; in particular, air at sea level conditions with a speed of $U_\infty = 1$ m/s was enforced, hence $Re \simeq 6.85 \cdot 10^3$ was considered during the mesh refinement analysis.
As explained in subsection 1.1.1, an incoming flow at this Reynolds number leads to a fully turbulent vortex street, while the boundary layer remains laminar; hence, an appropriate turbulence model must be used. During the mesh refinement analysis, it was decided to adopt the Hybrid SAS model combined with the $k-\omega$ SST model to resolve the boundary layer region. Indeed, Papadonikolaki and Stamou [52] demonstrated the efficiency of this turbulence model in the resolution of the flow around a 3D circular cylinder at high Reynolds numbers. A further analysis of the best turbulence model for the present case will then be presented in section 4.4. Moreover, in order to match the experiments conducted in the University of Liège, an oncoming turbulence level of 0.2% was imposed.
The time-step size was set to $dt = 0.025$ s in all the simulations (leading to a non-dimensional time-step of $U_\infty dt/D = 0.25$); this was done to ensure 20 time-steps per one period of vortex shedding, as recommended by [3]. However, it will be shown in

section 4.5 that a smaller time-step is needed to correctly capture the vortex shedding mechanism.
Furthermore, at each time-step it was ensured that the residuals became lower than 10^{-4} in order to get a proper convergence of the solution.
Finally, the simulations were run until reaching 15 stable periods of vortex shedding.
All the following simulations refer to the static cylinder case; the case of a cylinder undergoing forced motion will be presented in section 4.7 and will be deeply analyzed in chapter 5.

As the grid resolution analysis of the mesh in the $x-y$ plane was conducted in subsection 4.3.1, the same grid was used as a basis of the 3D model. Using the `Multizone` function in ANSYS MESHING, it was possible to create the 2D mapped mesh in Figure 4.8 and sweep it along the span. In this way, each section of the model at varying locations along the z-axis presents the same grid.
An analysis of the mesh resolution in the spanwise direction was conducted at this step, however, firstly, the grid in the $x-y$ plane was further checked and refined to meet the limitations required in case of such high Reynolds numbers. Indeed, a proper resolution of the flow in the boundary layer region is clearly dependent on the size of the mesh close to the cylinder's wall; in particular, prior importance is given to the height of the first cell touching the wall of the body, defined by the well-known y^+ value. In this project, it was ensured that the y^+ remained lower or equal to 1 for all the range of velocities tested, as recommended by [3] when using the turbulence models adopted.
Moreover, it was checked that the size transition of the elements from the boundary layer region to the edges of the domain was smooth enough, while ensuring a correct refinement in the wake downstream of the cylinder, in order to accurately capture the small turbulent scales present in that area.
A good resolution of the flow reaching the cylinder at $Re \simeq 6.85 \cdot 10^3$ was obtained in the $x-y$ plane by a first test, hence a deeper analysis of the grid resolution in the z-direction was conducted.

Analysis of the mesh resolution in the spanwise direction

Four different element sizes have been considered in the direction of the z-axis; in particular, the domain has been divided into 30, 75, 100 and 150 sections along the span, relative to an element size of 0.05 m, 0.02 m, 0.015 m and 0.01 m, respectively. These values fall perfectly in the range of spanwise number of elements and element sizes used by various researchers ($N_z = [4, 128]$) [18] [38] [41] [51] [52].

For the comparison of the different meshes, transient simulations were run and the Strouhal number, the mean drag coefficient and the root-mean-square value of the lift coefficient were first considered.
For these cases, the Strouahl number is easily obtained as $St = f_s/D$, as the incoming wind speed was set to 1 m/s, with f_s being calculated from the lift coefficient temporal evolution. Examples of unsteady lift and drag coefficients are available in Figure 4.15.

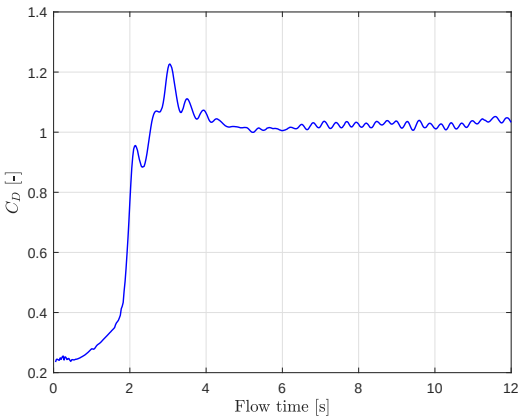

(a) Temporal evolution of C_D

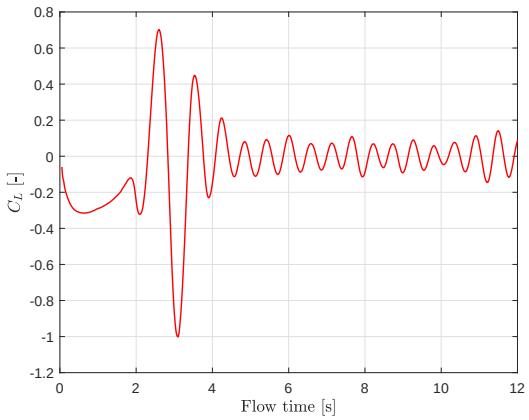

(b) Temporal evolution of C_L

Figure 4.15: Temporal evolution of the drag and lift coefficient at $Re \simeq 6.85 \cdot 10^3$, when $N_z = 100$

The variation in the amplitude of the lift and drag coefficient is a particularity encountered in the case of high Reynolds numbers; indeed, it was not observed in the laminar case in Figure 4.13. This can be explained by the fact the, at high Reynolds numbers, the vortex shedding mechanism is fully three-dimensional and small streamwise vortices appear together with the main spanwise vortex cores (this is a characteristic of the Mode B of vortex shedding), while the laminar case results completely two-dimensional.
High amplitude oscillations also occur in Figure 4.15 during the first 4 flow seconds; this is due to the small flow instability (an initial velocity component of 0.1 m/s along the y-direction) introduced as initial condition to fasten the onset of the vortex shedding mechanism.
However, despite the variations in the amplitude, only one main frequency characterizes the lift coefficient curve. Figure 4.16 presents the FFT of the lift coefficient in Figure 4.15b, where an high peak corresponding to the vortex shedding frequency is shown[4].

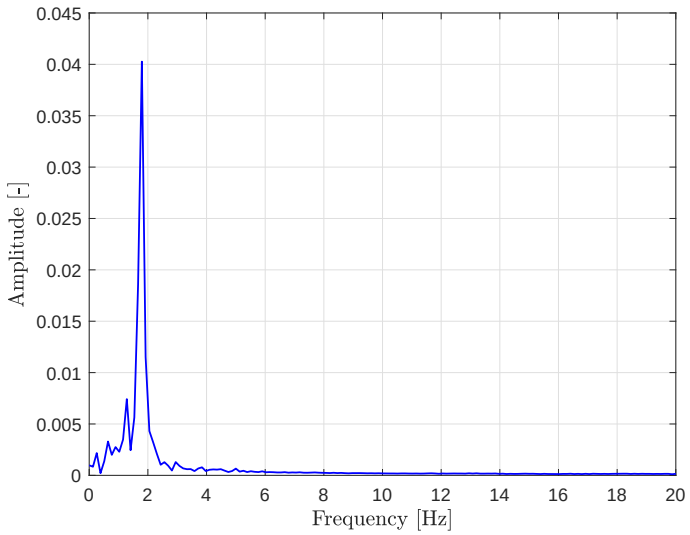

Figure 4.16: Fast Fourier Transform amplitude of the time variation of the lift coefficient at $Re \simeq 6.85 \cdot 10^3$ vs. frequency

[4]For the FFT calculation, the first transient part of the C_L curve was neglected, hence only the stable shedding periods were considered.

The Strouhal number can then be calculated; the results of St, $\bar{C}_D$ and $C_{L_{rms}}$ for the different grids are available in Table 4.3.

Table 4.3: Comparison between St, $\bar{C}_D$ and $C_{L_{rms}}$ for different mesh refinements along the span

N_z [-]	St [-]	$\bar{C}_D$ [-]	$C_{L_{rms}}$ [-]
30	0.1824	1.0335	0.2320
75	0.1818	1.0564	0.2320
100	0.1831	1.0318	0.2928
150	0.1824	1.0294	0.2942

An increase of $\simeq 20.8\%$ in the $C_{L_{rms}}$ is noticed in Table 4.3 when N_z goes from 75 to 100 elements; then a slight growth is observed at $N_z = 150$.
The mean drag coefficient reaches its maximum at $N_z = 75$, but it keeps similar values in the other cases. On the other hand, a very small variation in the Strouhal number is observed among the tested grids.
The $C_{L_{rms}}$ agrees well with the results obtained by Gerrard [28] ($C_{L_{rms}} = [0.02, 0.87]$ for $Re = [4 \cdot 10^3, 18 \cdot 10^4]$ and 0.3% of oncoming turbulence), Kefee [39] ($C_{L_{rms}} = [0.27, 0.52]$ for $Re = [5 \cdot 10^3, 9.2 \cdot 10^4]$ and 0.3% of oncoming turbulence) and other researchers [8] [40] [32] [45] [49]. Moreover, the mean drag coefficient approaches the results obtained by Young and Ooi [51] ($\bar{C}_D = 1.03$) and Kravchenko and Moin [41] ($\bar{C}_D = 1.04$) for $Re = 4 \cdot 10^3$.
The Strouhal number seems a bit lower (around -10.7%) than the expected value ($\simeq$ 0.2049 got in subsection 4.1.1). This result is accepted at this stage, as a quite big time-step was chosen to run these simulations. Indeed, a more accurate St will be found in section 4.5 when adopting smaller time-steps.

Furthermore, the variation in the mean velocity profiles for the different cases has been analyzed. In particular, the evolution of the x- and y-velocity components along the y-axis was registered at mid-span at two different locations in the wake region, $x/D = 1$ and $x/D = 3$[5]. The results are presented in Figure 4.17 and Figure 4.18, where they are non-dimensionalized using the free-stream velocity, U_∞, and the cylinder's diamater, D.

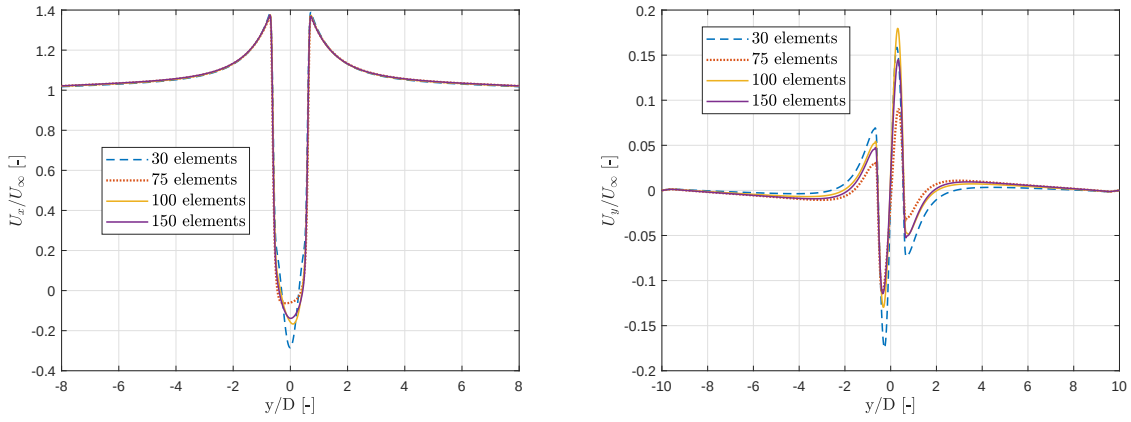

(a) Evolution of U_x/U_∞ vs. y/D (b) Evolution of U_y/U_∞ vs. y/D

Figure 4.17: Comparison between the non-dimensional U_x and U_y velocity components along the y-axis at $x/D = 1$ for different mesh refinements at $Re \simeq 6.85 \cdot 10^3$

[5]In this project, the center of each cylinder's section is positioned at $(x, y) = (0, 0)$.

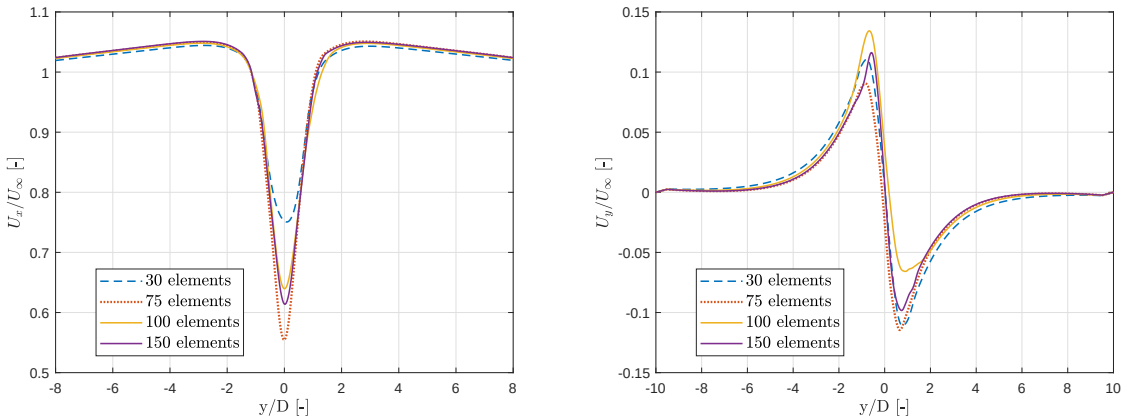

(a) Evolution of U_x/U_∞ vs. y/D

(b) Evolution of U_y/U_∞ vs. y/D

Figure 4.18: Comparison between the non-dimensional U_x and U_y velocity components along the y-axis at $x/D = 3$ for different mesh refinements at $Re \simeq 6.85 \cdot 10^3$

From the graphs above it is possible to notice that all the curves obtained using $N_z = 100$ and $N_z = 150$ are very similar; the only differences are visible in Figure 4.17b and Figure 4.18b, as slightly higher peaks denote the curves of the coarsest mesh. On the other hand, the models using 30 and 75 elements tend to excessively over- or under-estimate the two velocity components.

Similar trend is shown in Figure 4.19, where the evolution of the x-velocity component along the wake center line, at mid-span, is presented. Very close curves characterize the models using 100 and 150 elements, while some differences are observed in the other two cases.
However, the general shape of the curves is obtained in all the simulations: in Figure 4.19, a first drop in the velocity is noticed close to the cylinder; then, after the recirculation area, the flow accelerates and U_x reaches an approximately constant value.
The trend of the plots above approaches well the ones obtained by various researchers [41] [51] [52].

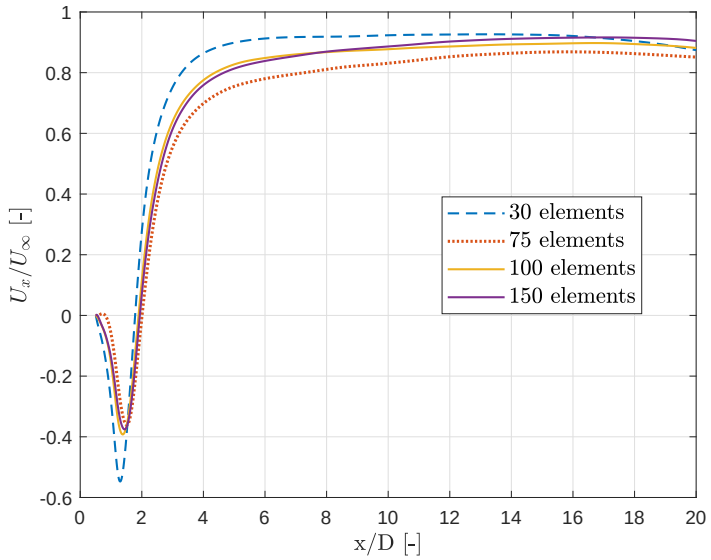

Figure 4.19: Comparison between the non-dimensional U_x component velocity along the wake center line for different mesh refinements at $Re \simeq 6.85 \cdot 10^3$

Finally, in order to have a complete understanding of the effects of the mesh refinement in the spanwise direction, the vortex flow structure was analyzed by means of the iso-surface plot of the second negative eigenvalue, λ_2, of the tensor $\Psi^2 + \Omega^2$. The latters are the symmetric and the anti-symmetric part of the velocity-gradient tensor, respectively. Indeed, the second negative eigenvalue gives the location of the vortex core, hence it allows to acquire a deep understanding of the vortex shedding mechanism encountered in the considered model.
For this purpose, the iso-surfaces were plotted in ANSYS CFD-POST by setting $-\lambda_2$ to be equal to 0.01[6].
Figure 4.20 and Figure 4.21 displays two views of iso-surface plot obtained using $N_z = 30$.

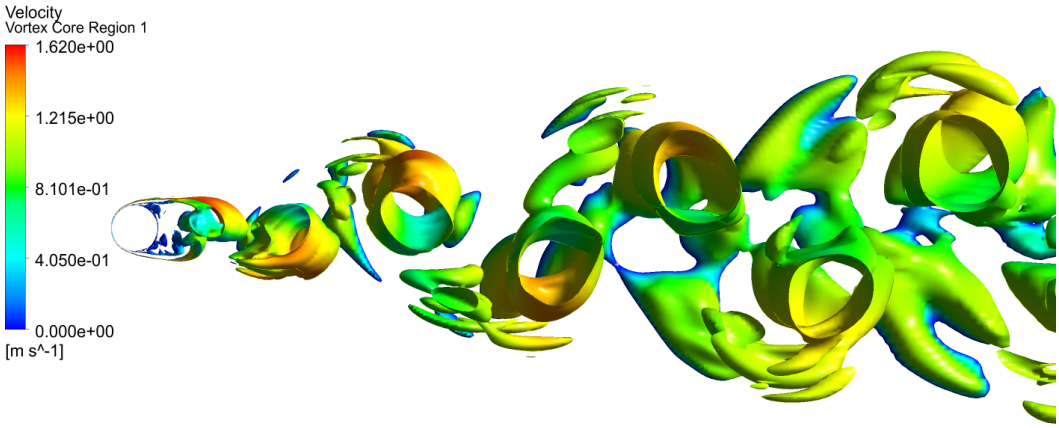

Figure 4.20: Iso-surface plot of $-\lambda_2 = 0.01$ colored using the velocity field for $N_z = 30$ at $Re \simeq 6.85 \cdot 10^3$(view in the $x - y$ plane, front view)

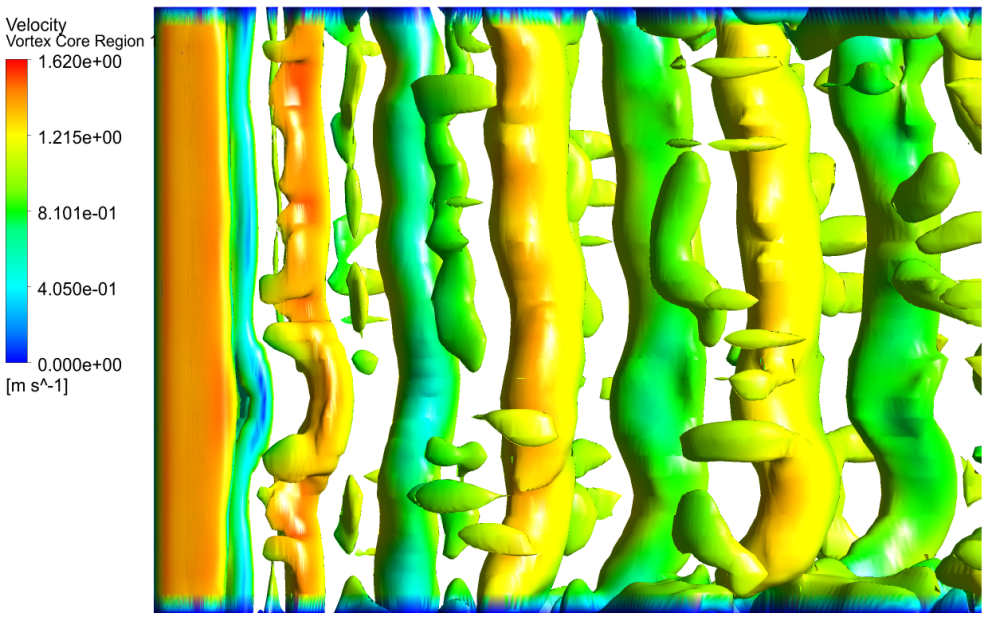

Figure 4.21: Iso-surface plot of $-\lambda_2 = 0.01$ colored using the velocity field for $N_z = 30$ at $Re \simeq 6.85 \cdot 10^3$ (view in the $x - z$ plane, top view)

It is possible to notice from the figures above that, despite the three-dimensionality of the flow in the wake region, this model is not able to capture the formation of finer-scale streamwise vortex pairs, typical of the Mode B of vortex shedding. The reason is

[6]All the iso-surface plots are taken at the last time-step of the simulation.

clearly the coarseness of the mesh; indeed, as Figure 4.22 and Figure 4.23 show, increasing the number of elements in the z-direction up to 100, these finer-scale streamwise vortex pairs appear and a more chaotic flow behavior is observed in the far-wake. Moreover, unlike in Figure 4.21, the big vortex cores no longer maintain the same shape in the spanwise direction as vortex dislocations occur. However, they remain almost parallel to the cylinder's axis, hence the oblique vortex shedding is not predicted by the present model (as it will be discussed in section 4.4, this is due to the turbulence model in use).

While for the model cases having $N_z = 30$ and $N_z = 75$ not all the vortex scales are resolved, no major differences appear using $N_z = 100$ and $N_z = 150$. This can also explain the growth in the $C_{L_{rms}}$ observed for finer grids.
It was then concluded that reliable results can be obtained by means of the model having 100 elements in the spanwise direction; the latter was then chosen to proceed with further calculations.

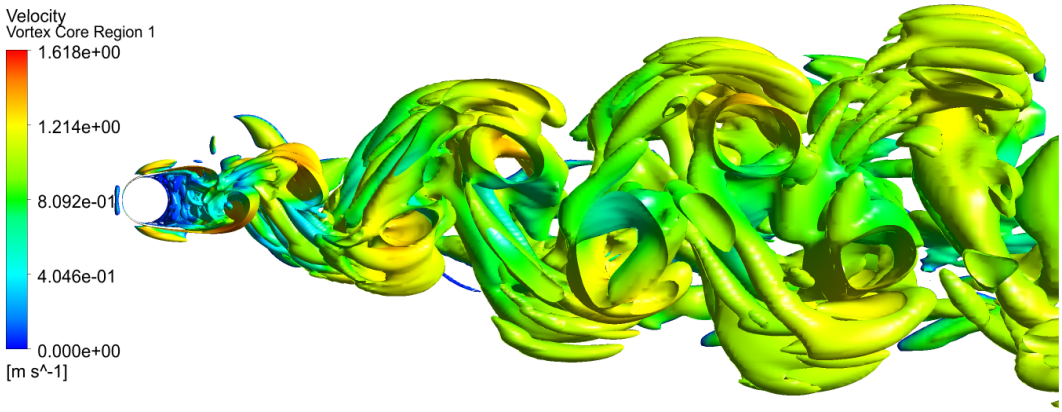

Figure 4.22: Iso-surface plot of $-\lambda_2 = 0.01$ colored using the velocity field for $N_z = 100$ at $Re \simeq 6.85 \cdot 10^3$(view in the $x - y$ plane, front view)

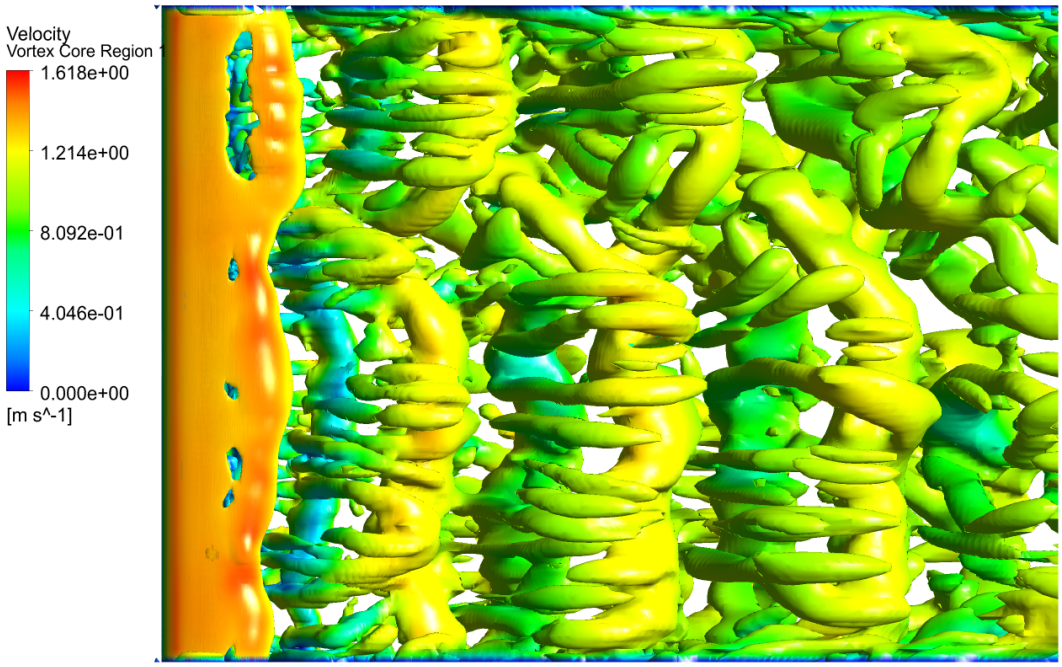

Figure 4.23: Iso-surface plot of $-\lambda_2 = 0.01$ colored using the velocity field for $N_z = 100$ at $Re \simeq 6.85 \cdot 10^3$(view in the $x - z$ plane, top view)

4.3.3 Mesh characteristics

In conclusion, remembering that the cylinder's diameter was set to $D = 0.1$ m, the chosen model presents the following characteristics:

Table 4.4: Characteristics of the model

Characteristics	Values
Model dimensions [-]	$30D$x$20D$x$15D$
Height of the first cell [m]	$8.3 \cdot 10^{-5}$
Total number of elements [-]	22488660
Number of elements in the x-direction [-]	380[7]
Number of elements in the y-direction [-]	295[8]
Number of elements in the z-direction [-]	100[9]
Number of nodes around each cylinder's section [-]	576

Finally, some pictures of the chosen mesh are presented above. In particular, some zooms allow to have a better vision of the mesh in the spanwise direction, as well as around the body and in the wake region.

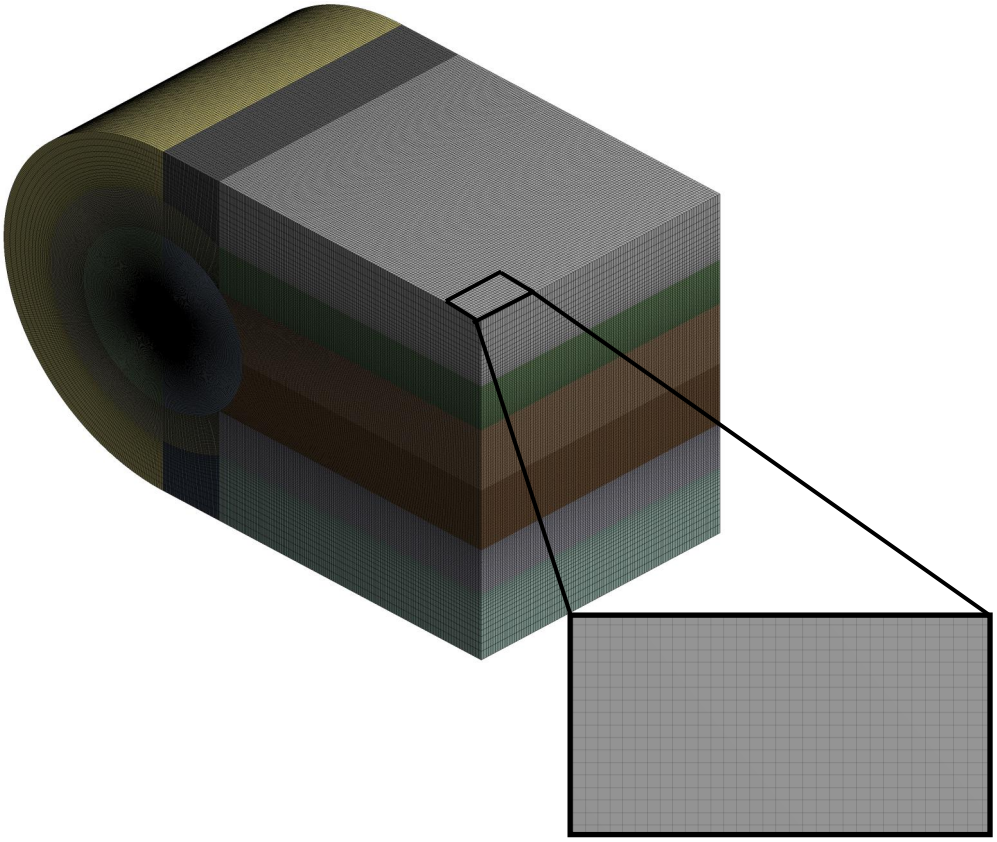

Figure 4.24: Zoom of the mesh in the spanwise direction

[7]This number indicates only the elements in the wake region (the elements occurring from the inlet to the cylinder's left half are neglected).

[8]It accounts only for the elements appearing from the cylinder's section upper point to the domain's upper boundary (the model is symmetric with respect to the x-axis, hence there is the same number of elements in the lower part).

[9]The element size in the z-direction is then equal to $0.15D$.

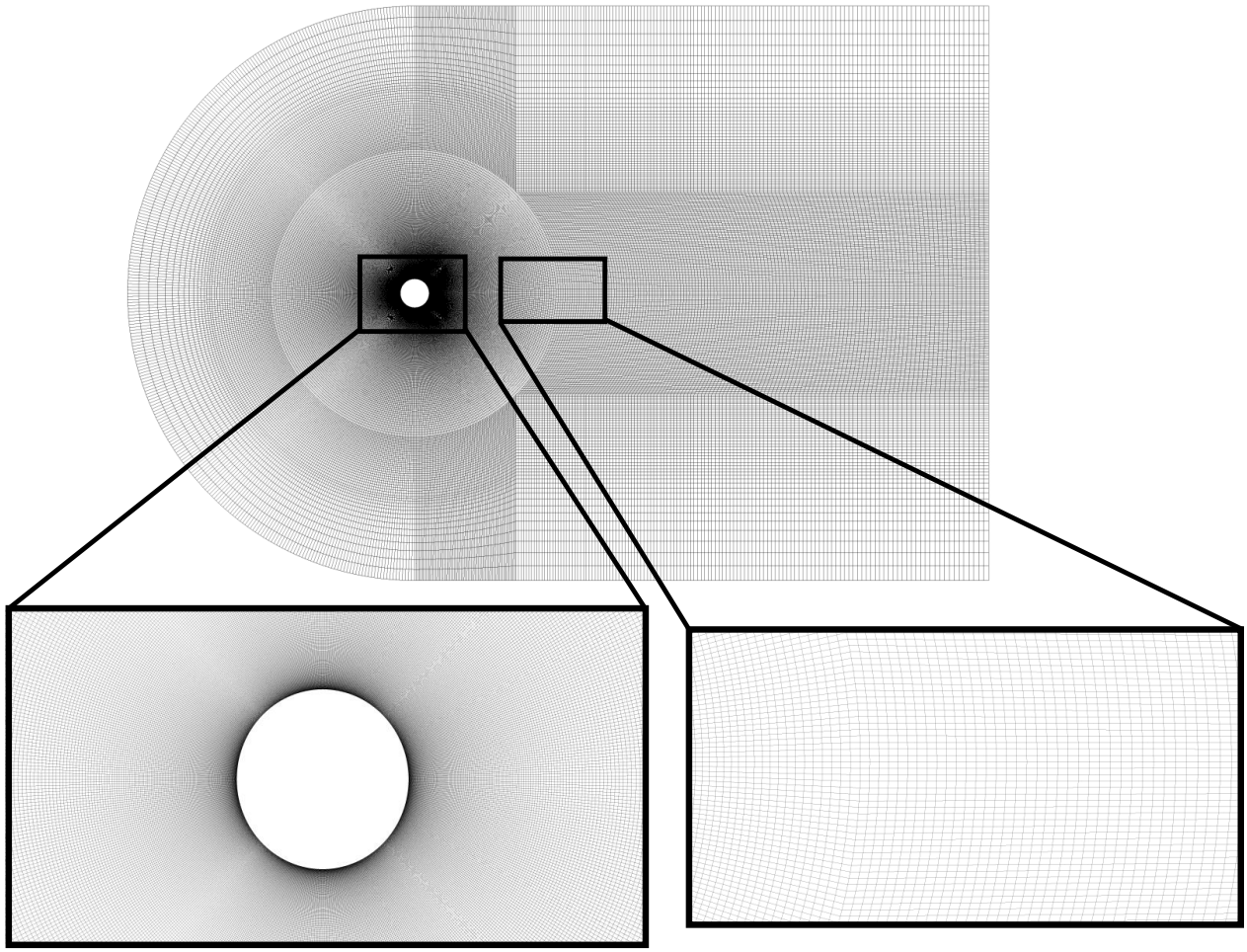

Figure 4.25: Zoom of the mesh around the body and in the wake, in the streamwise direction

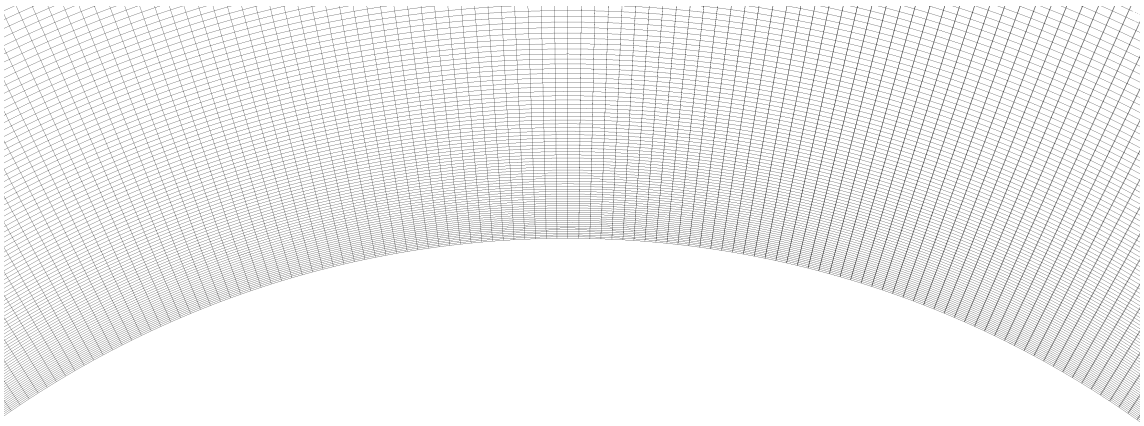

Figure 4.26: Zoom of the mesh in the proximity of the cylinder's wall

4.4 Turbulence model analysis

Once a proper mesh refinement was chosen, the analysis of the best turbulence model for the present case was then conducted.
The two different turbulence model categories have both been considered: the URANS and the SRS turbulence models. In particular, in this project, the $k-\omega$ SST, the Transition SST, the SAS and the DES models have been tested. The two SRS models have been combined with both $k-\omega$ SST and Transition SST for the resolution of the flow in the boundary layer region.

Table 4.5 displays several parameters found using the different turbulence models. The Strouhal number, St, the mean drag coefficient, $\bar{C}_D$ and the rms value of the lift coefficient, $C_{L_{rms}}$, have been extracted for the comparison, as well as the angle at which the boundary layer separation occurs, θ_{sep}, and the value of the base pressure coefficient, C_{pb}.

Table 4.5: Comparison of St, $\bar{C}_D$, $C_{L_{rms}}$, θ_{sep} and C_{pb} for different turbulence models

Turbulence model	St [-]	$\bar{C}_D$ [-]	$C_{L_{rms}}$ [-]	θ_{sep} [^{o}]	C_{pb} [-]
$k-\omega$ SST	0.1135	0.2045	0.1960	67	-0.6121
Transition SST	0.1173	0.2139	0.1916	68.87	-0.7094
SAS & $k-\omega$ SST	0.1831	1.0318	0.2928	68.24	-0.8778
SAS & Transition SST	0.1866	1.0496	0.2021	70	-0.8512
DES & $k-\omega$ SST	0.1811	1.0446	0.2571	69.5	-0.8415
DES & Transition SST	0.1824	1.0792	0.2239	70	-0.8812

While the SRS models give very similar St, $\bar{C}_D$ and $C_{L_{rms}}$, the URANS models highly underestimate the value of the Strouhal number and the mean drag coefficient (approximately, -39% of St and -79% of $\bar{C}_D$ with respect to the values found using the SAS & $k-\omega$ SST model). Indeed, it was registered a quite low vortex shedding frequency ($f_s \simeq 1.1$ Hz) when using the $k-\omega$ SST and the Transition SST model.
A bad resolution of the vortex shedding phenomenon using the URANS models can also be demonstrated by looking at the iso-surface plot in Figure 4.27. A 2D regular vortex shedding is indeed detected by the Transition SST model (similar results are observed using the $k-\omega$ SST model), while, as explained subsection 4.3.2, a fully 3D behavior is expected. No small turbulent scales are then present in Figure 4.27, due to the nature of the URANS models, based on averaging the Navier-Stokes equations, as deeply discussed in section 3.2. The bad resolution of f_s can also be explained by the large time-step chosen is these simulations, which, however, seems working fine when using the SRS models.

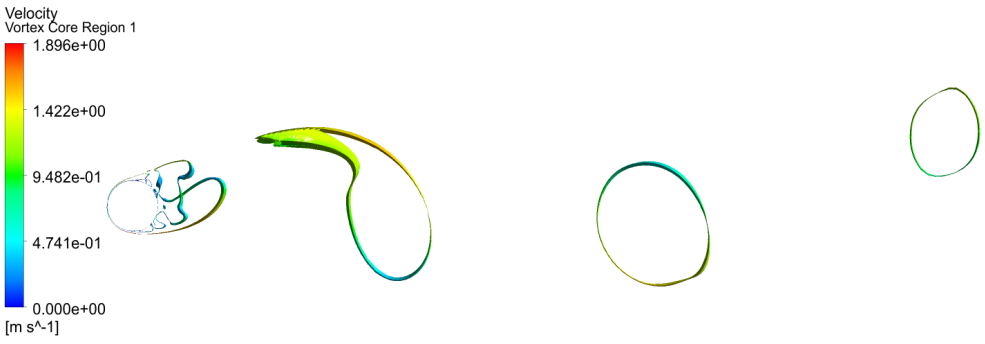

Figure 4.27: Iso-surface plot of $-\lambda_2 = 0.01$ colored using the velocity field obtained with the Transition SST model (view in the $x-y$ plane, front view)

On the other hand, the angle of separation, θ_{sep}, results well predicted by all the turbulence models used. A slight lower value is observed using the $k-\omega$ SST model, however, a non-negligible underestimation in the base pressure coefficient, C_{pb}, is given by the two URANS models.
A visualization of the complete C_p curves in the range $\theta = [0^o, 180^o]$ is available in Figure 4.28.

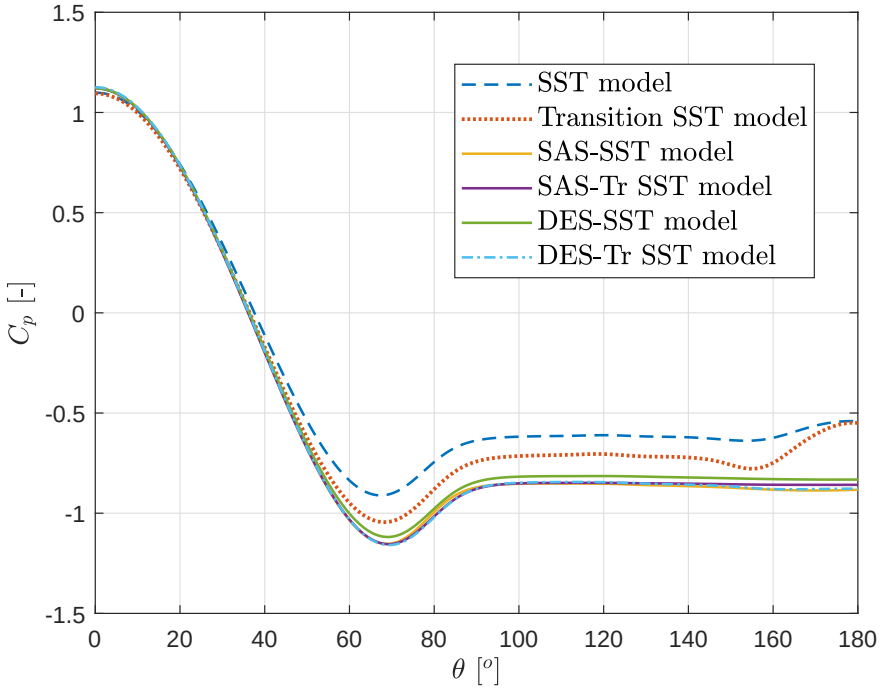

Figure 4.28: Comparison between the C_p vs. θ for different turbulence models

It is interesting to notice that all the curves do not start at $C_p = 1$, as it would have been expected. Thus, a small overestimation ($+10\%$) of the pressure coefficient at the stagnation point occurs. The same result is reported by Wornom et al. [19] and it might be «due to the fact that a compressible flow solver is used; even if the Mach number is low [...] and ad-hoc preconditioning is used, small compressibility effects are present at the stagnation point» [19].
On the other hand, a small jump in the C_p curve is observed at around $\theta = 155^o$ using the URANS models, not present in the other curves. However, the general shape of the C_p curve is recovered by all the turbulence models, but, while the DES and SAS models lead to very close results, the remaining curves are slightly shifted up.
The angle of separation ($\theta_{sep} \simeq 70^o$) is the same as the one found by Norberg [49] and Kravchenko [41] for $Re = 8 \cdot 10^3$ and $Re = 4 \cdot 10^3$, respectively, but the C_{pb} results a bit higher than the one predicted by Norberg ($C_{pb} \simeq -1.05$) at $Re = 8 \cdot 10^3$ and low oncoming turbulence level ($\simeq 0.1\%$).

Furthermore, the evolution of the mean x- and y-velocity components along the y-axis at mid-span at $x/D = 3$ is presented in Figure 4.29. It appears again clear that, while the SRS models produce very similar results, the URANS models tend to over- or underestimate the values of the velocity components.

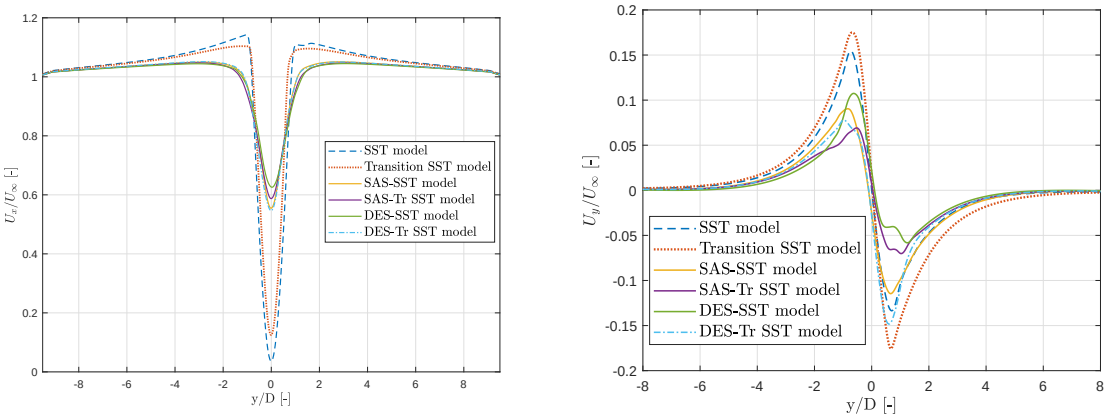

(a) Evolution of U_x/U_∞ vs. y/D

(b) Evolution of U_y/U_∞ vs. y/D

Figure 4.29: Comparison between the non-dimensional U_x and U_y velocity components along the y-axis at $x/D = 3$ for different turbulence models at $Re \simeq 6.85{\cdot}10^3$

A similar behavior is then visible in Figure 4.30, which represents the mean x-velocity component along the wake center line.

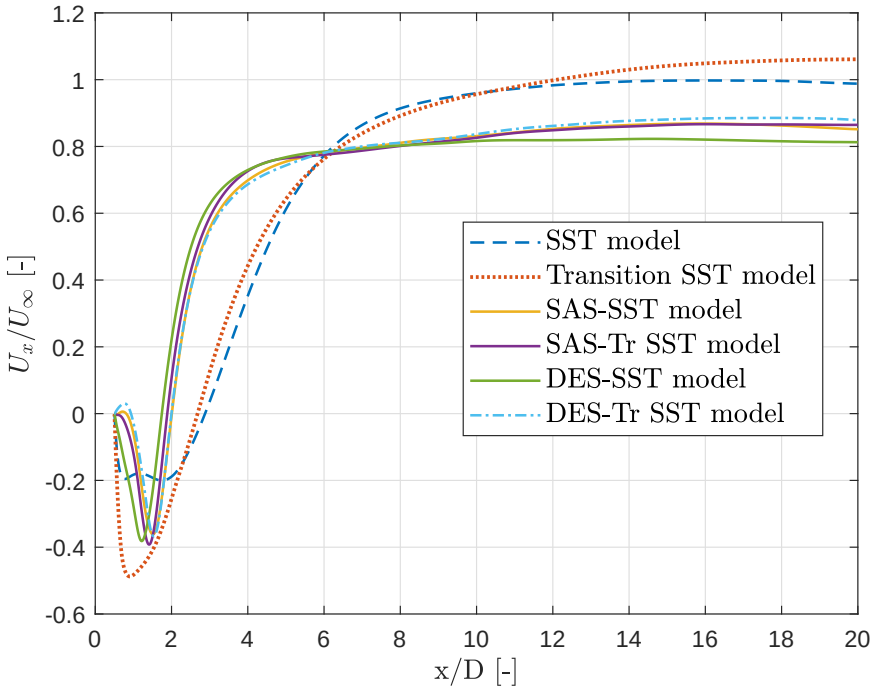

Figure 4.30: Comparison between the non-dimensional U_x velocity component along the wake center line for different turbulence models at $Re \simeq 6.85 \cdot 10^3$

For the aforementioned reasons, the URANS models have been judged not adapt to well resolve the turbulent flows reaching a 3D bluff body at high Reynolds numbers.
In order to choose the best SRS model to be adopted, the iso-surface plot of the λ_2 criterion at the end of the simulation has been analyzed. Figure 4.31 and Figure 4.32 indeed display the the iso-surface plot obtained using the DES model combined with the Transition SST model for the resolution of the boundary layer.

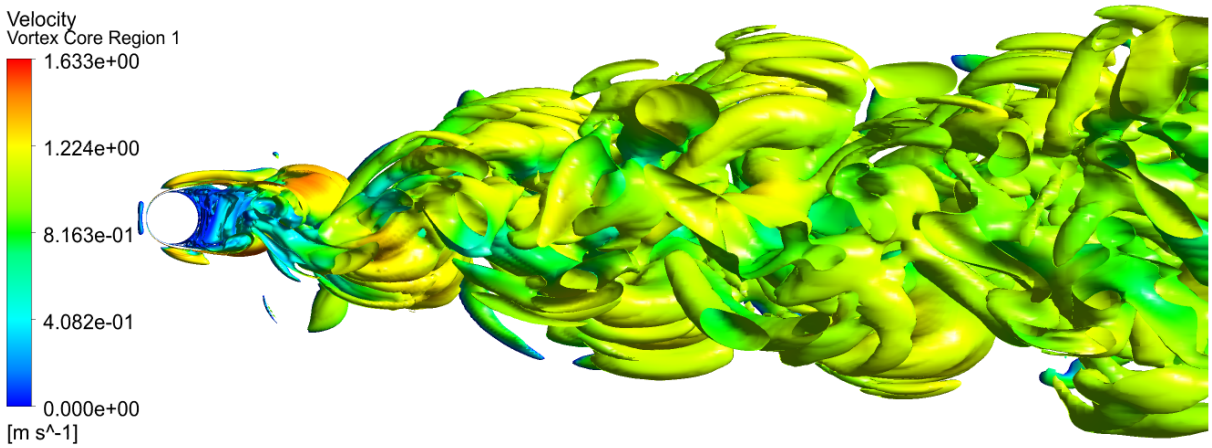

Figure 4.31: Iso-surface plot of $-\lambda_2 = 0.01$ colored using the velocity field for DES & Transition SST model at $Re \simeq 6.85 \cdot 10^3$ (view in the $x-y$ plane, front view)

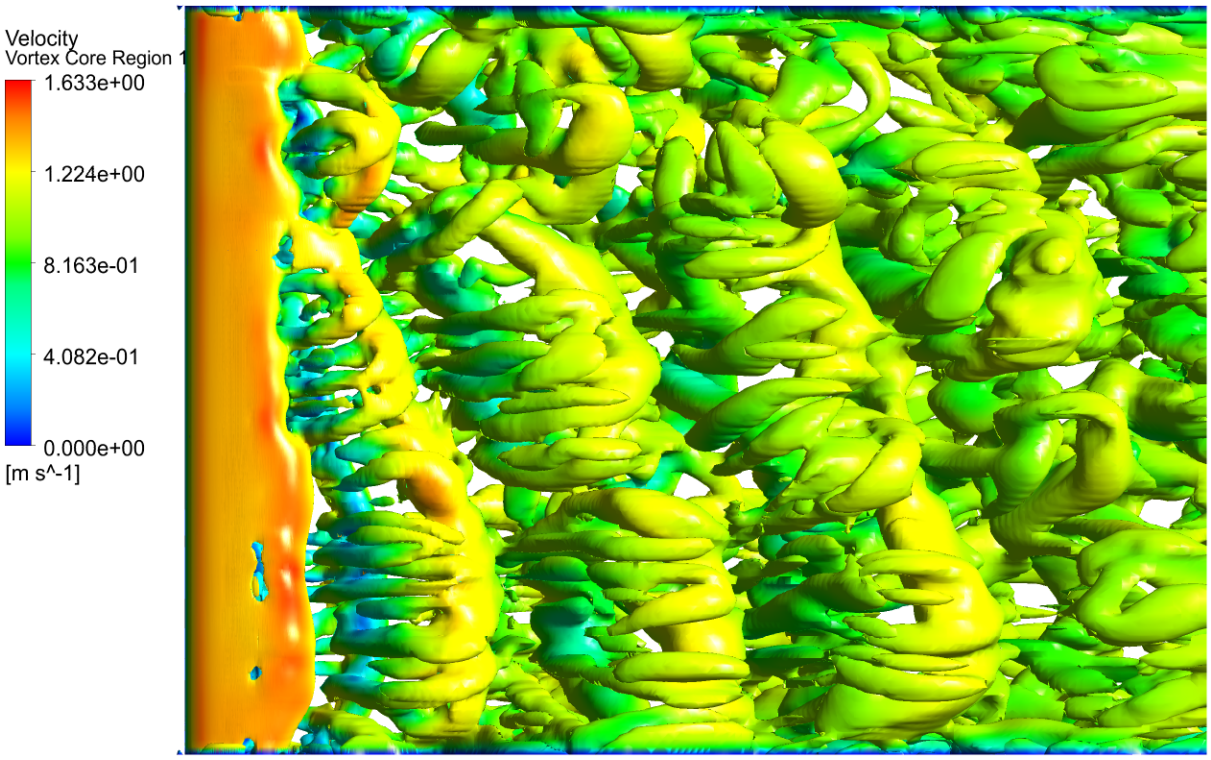

Figure 4.32: Iso-surface plot of $-\lambda_2 = 0.01$ colored using the velocity field for DES & Transition SST model at $Re \simeq 6.85 \cdot 10^3$ (view in the $x-z$ plane, top view)

The figures above clearly show a three-dimensional behavior of the wake region. The big spanwise vortex cores, as well as the finer-scale streamwise vortex pairs, appear in Figure 4.32, as predicted by the Mode B of vortex shedding. Some vortex dislocations along the span are also detected and a more chaotic flow characterizes the far-wake. It is very interesting to notice that, unlike the SAS model shown in Figure 4.23, the main vortex cores do not shed parallel to the cylinder's axis, but they are tilted by an angle of approximately 15^o. Thus, the oblique shedding is finally captured.

Moreover, from the vorticity contour plots in Figure 4.33 and Figure 4.34, it is possible to notice that a more complex flow behavior is detected by the DES model. Indeed, several small turbulent scales are present in Figure 4.34, especially in the far-wake, where the complexity of the flow highly increases.

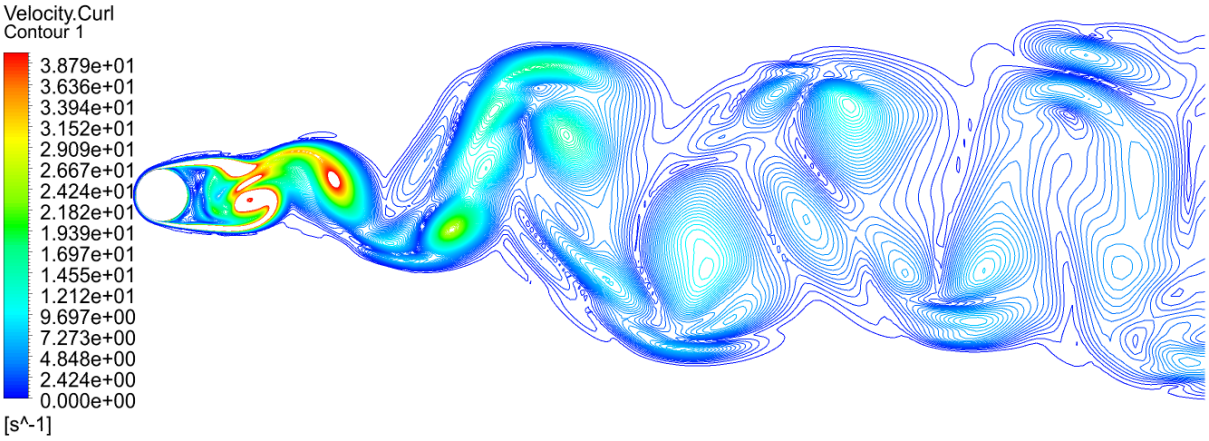

Figure 4.33: Vorticity contour plot for SAS & Transition SST model at $Re \simeq 6.85 \cdot 10^3$ (view at mid-span in the $x - y$ plane)

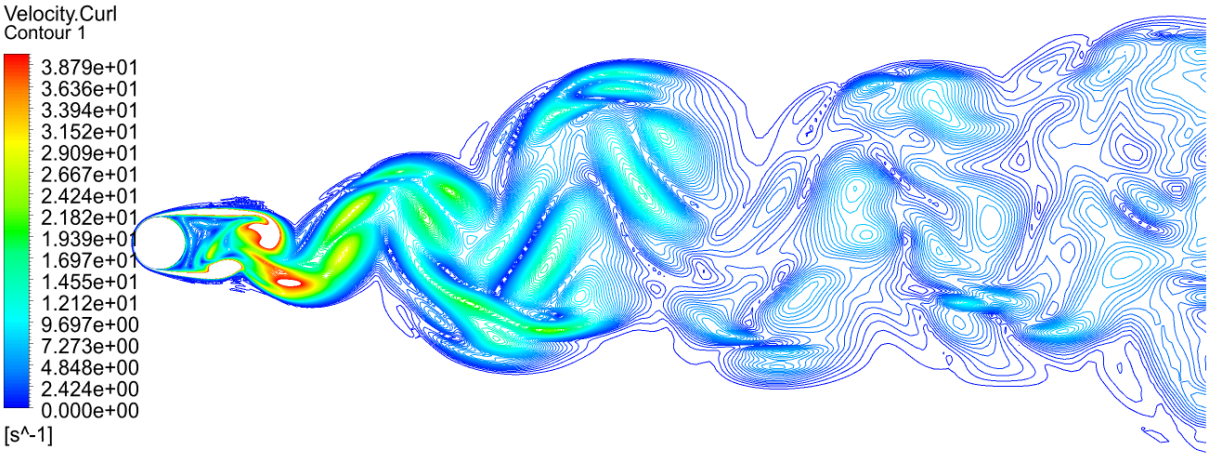

Figure 4.34: Vorticity contour plot for DES & Transition SST model at $Re \simeq 6.85 \cdot 10^3$ (view at mid-span in the $x - y$ plane)

Given the above results, it is possible to conclude that the DES turbulence model is able to well capture the complex behavior of the flow reaching the cylinder with no increase in the computational cost compared to the SAS model, hence it results the best model to adopt in this study.

Finally, no major differences in computational cost were observed when combining the DES model with the $k - \omega$ SST and the Transition SST model. It was anyway decided to adopt the DES model in combination with the Transition SST model as, despite the turbulence of the flow in the wake, in the Reynolds range of interest the boundary layer around the cylinder is laminar. The Transition SST model is indeed the only turbulence model among the ones analyzed capable of predicting a laminar boundary layer even with a turbulent flow in the wake region.

4.5 Time-step size analysis

Tha last parameter analyzed in this study was the size of the time-step imposed in the simulation.
As mentioned in section 4.3, 20 time-steps per period of vortex shedding were first considered, hence a time-step of $dt = 0.025$ s was imposed. This leads to a non-dimensional time-step of $U_\infty dt/D = 0.25$, way higher than the one used by previous researchers (in the range of [0.001, 0.05]) [38] [41] [51] [52], which, however, was giving quite satisfying results.
It was then decided to test different time-step sizes to also consider the case with 10, 50 and 100 time-steps per period of vortex shedding. Thus, a non-dimensional time-step of 0.5, 0.1, 0.05 was imposed in the simulations, approaching the range used by other researchers; the results are available in Table 4.6, where St, $\bar{C}_D$, $C_{L_{rms}}$, θ_{sep} and C_{pb} are shown.

Table 4.6: Comparison between St, $\bar{C}_D$, $C_{L_{rms}}$, θ_{sep} and C_{pb} for different time-step sizes

Time-step size [-]	St [-]	$\bar{C}_D$ [-]	$C_{L_{rms}}$ [-]	θ_{sep} [^{o}]	C_{pb} [-]
0.5	0.1429	1.0481	0.2694	70	-0.8982
0.25	0.1824	1.0792	0.2239	70	-0.8812
0.1	0.1948	1.0157	0.3093	70	-0.8194
0.05	0.2098	1.0347	0.2411	69	-0.9005

It appears clear from the table above that a too big time-step, such as $U_\infty dt/D = 0.5$, is not able well capture the vortex shedding phenomenon and an high underestimation of the Strouhal value and, consequentially, of the frequency of vortex shedding, occurs (approximately, -30% of St with respect to the expected value of 0.2). A sudden increase in St is then visible when 10 more time-steps are added in the shedding period ($U_\infty dt/D = 0.25$), going from 0.1429 to 0.1824. Afterwards, the Strouhal number seems to more gradually converge to the expected value; hence, finally, $St = 0.2098$ is reached at $U_\infty dt/D = 0.05$ ($\simeq$2% of difference from the experimental St found in subsection 4.1.1). On the other hand, the remaining parameters do not experience drastic changes when the time-step size is varied and only some small oscillations in their values occur. The maximum variation is given by the C_{pb}, which slightly drops (approximately, -8%) in the case of $U_\infty dt/D = 0.1$

Figure 4.35 shows the evolution of the pressure coefficient for varying time-step sizes. In general, the curves appear very similar to each other; the one relative to the smallest time-step presents a lower C_p at the stagnation point, which reduces the error due to the compressibility effects.
Some small variations are observed in the C_{pb}, as mentioned; it is also interesting to notice the similarity between the two curves with the highest and the lowest time-step size, which was explained as fortuitous.

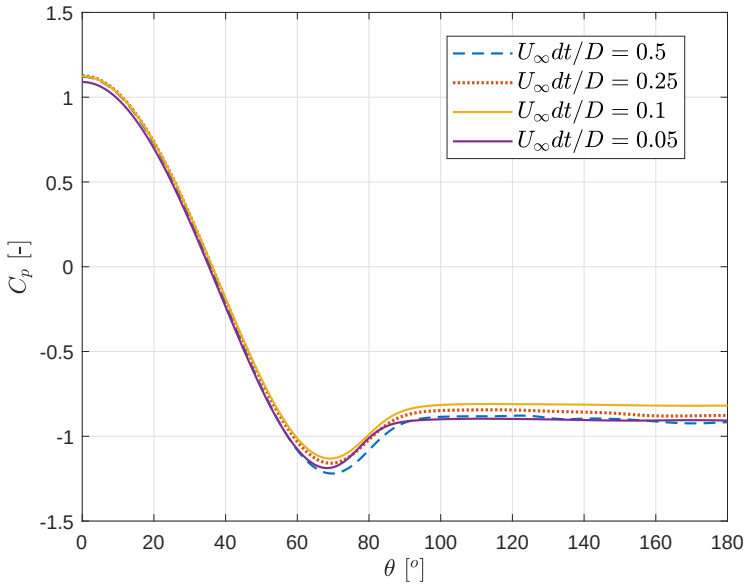

Figure 4.35: Comparison between the C_p evolution vs. θ for the different time-step sizes at $Re \simeq 6.85 \cdot 10^3$

Finally, the iso-surface plots of $-\lambda_2$ obtained by the run cases were compared; the plots relative to $U_\infty dt/D = 0.5$ and $U_\infty dt/D = 0.1$ are available in Figure 4.36.

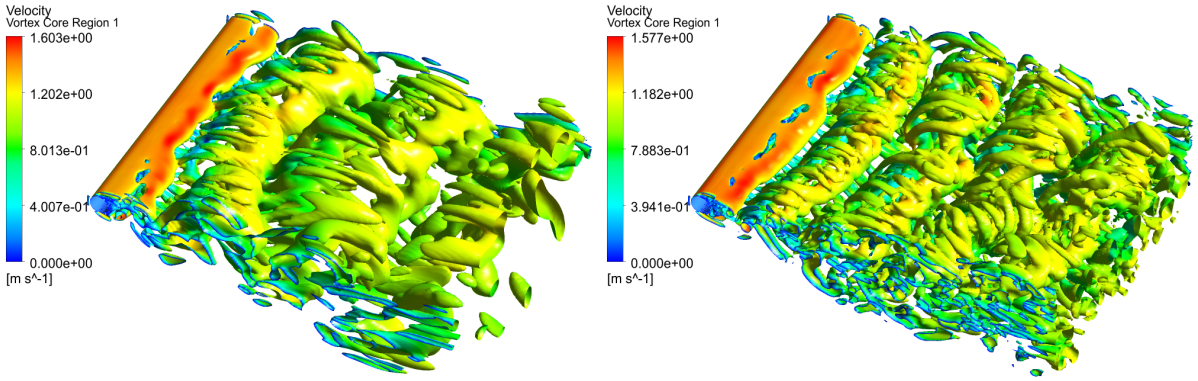

(a) Plot for $U_\infty dt/D = 0.5$ (b) Plot for $U_\infty dt/D = 0.1$

Figure 4.36: Iso-surface plot of $-\lambda_2 = 0.01$ colored using the velocity field obtained at the end of the simulation for different time-step sizes at $Re \simeq 6.85 \cdot 10^3$

It is clearly visible the difference in the wake region between the plots in Figure 4.36a and Figure 4.36b; despite its three-dimensionality, the wake formed using the biggest time-step does not contain all the small-turbulent scales captured by smaller time-steps. Moreover, its bad resolution of the vortex shedding frequency makes this time-step size unsuitable for this project.

Finally, it was decided to adopt the non-dimensional time-step equal to 0.05 (the same as the one used by Young and Ooi [51]). Indeed, it proved to give very good results regarding all the parameters presented in Table 4.6, while leading to an high resolution of the flow in the wake region. In particular, the Strouhal number is very similar to the experimental one and to the one found by other researchers [38] [41] [49] [51], and the base

pressure coefficient appears to be the closest one to the value obtained by Norberg [49] ($C_{pb} = -1.05$).

As mentioned in section 4.3, the simulations were stopped after reaching 15 stable periods of vortex shedding (the range of periods found in previous works is [10, 86] [38] [41] [51] [52]). It was also tested the resolution of the aforementioned parameters over higher numbers of stable shedding periods, N_T. No significant effects were reported when increasing N_T; indeed, the Strouhal number only increases by 1.5% ($St = 0.2129$) when going from $N_T = 15$ to $N_T = 30$. Hence, it can be concluded that the model gives good results even after 15 vortex shedding periods, which is an important point in order to run the simulation for a lower amount of time.

4.6 Reduction of the domain size

Before proceeding with the comparison between the computational and the experimental results described in subsection 4.1.1, it was decided to test a smaller computational domain with the purpose of possibly reducing the overall computational cost. Indeed, the choices of mesh refinement, turbulence model and time-step sizes made in the previous sections, despite necessary for a correct resolution of the case of study, led to a very expensive cost. Approximately 40 hours were needed to run 15 stable periods of vortex shedding; this cost would then be further increased for the case of cylinder forced to oscillate.
The main idea to reduce the cost of the simulation was then to decrease the spanwise length of the domain. Indeed, several researchers [18] [38] [41] [51] [52] built their models using a fairly short spanwise length (in the range $L_z = [D, 2\pi D]$); in particular, $L_z = \pi D$ was often used and was proven to give reliable results, thus it was tested in this project[10].

After the domain's reduction, the mesh has been maintained unaltered, hence the element size in the z-direction has been kept to the value chosen in section 4.3, equal to 0.015 m ($0.15D$). A picture of the new model is shown in Figure 4.37, where the total number of elements has been reduced to 4264920 (-81% of elements).

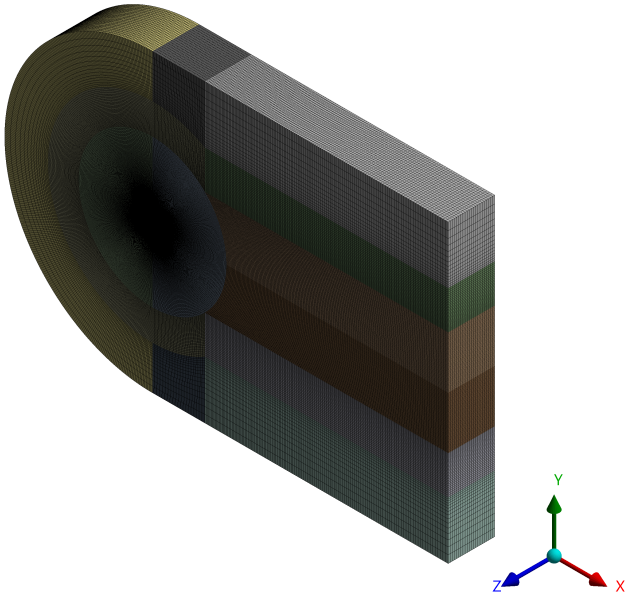

Figure 4.37: Visualization of the domain with $L_z = \pi D$

[10]It was approximated to 0.315 m.

Moreover, when only a piece of the cylinder is modeled, periodic boundary conditions should be enforced at the front and at the back face of the domain; this is done to simulate a cylinder with an infinite length, avoiding non-negligible end effects.

Eventually, this reduction in L_z did not have major effects on the various parameters in Table 4.6. The Strouhal number indeed remained almost equal to the value of 0.2098 found in the previous section, reaching 0.2067. Furthermore, Figure 4.38 shows that the two C_p curves obtained using the biggest and the smallest domain are very close to each other; the C_{pb} is slightly reduced and becomes equal to -0.9274, approaching the experimental results from Norberg [49].

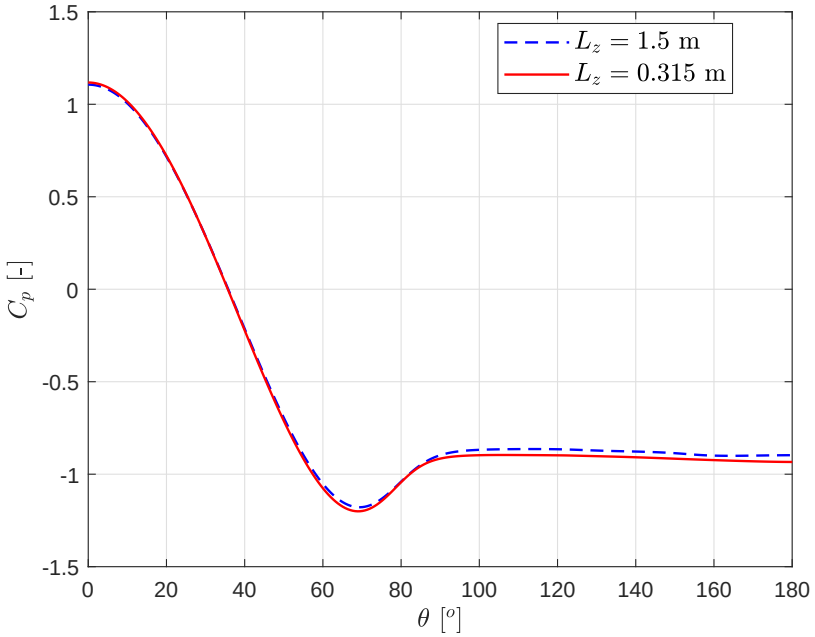

Figure 4.38: Comparison between the C_p evolution vs. θ for the two models having $L_z = 1.5$ m and $L_z = 0.315$ m at $Re \simeq 6.85 \cdot 10^3$

Finally, in order to confirm the reliability of the small model, the iso-surface plot of the λ_2 criterion was analyzed. The front and the top view of the plot are available in Figure 4.39 and Figure 4.40, respectively.
The model is certainly able to capture the Mode B of vortex shedding, as proven by the finer-scales streamwise vortices visible in the figures below. Moreover, as expected, the flow becomes more chaotic in the far-wake, where vortices following an ordered pattern no longer appear.
However, the model seems not able to capture the vortex dislocations nor the oblique shedding mode. This can be easily explained by the short spanwise length chosen, along which the vortex cores do not experience any dislocation. On the other hand, the absence of oblique shedding can be explicated by the boundary conditions adopted in this model. Indeed, remembering that the main source of oblique shedding is given by the end effects, as explained in subsection 1.1.1, the periodic boundary conditions applied to the front and back faces of the domain annuls any possible effect from the edges of the model. However, this seems not affecting the vortex shedding frequency resolution nor the mean pressure coefficient at the mid-span section.

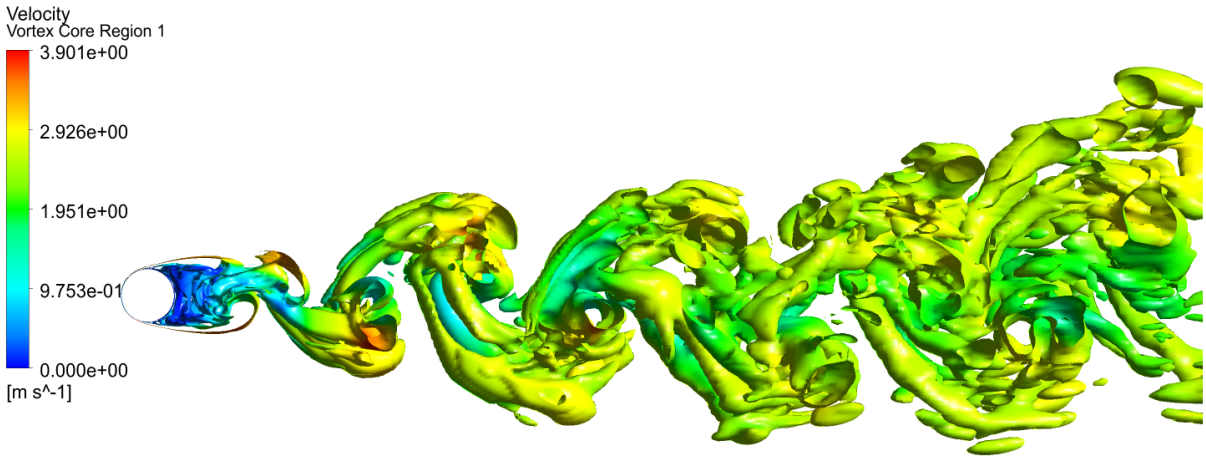

Figure 4.39: Iso-surface plot of $-\lambda_2 = 0.01$ colored using the velocity field for the model with $L_z = \pi D$ at $Re \simeq 6.85 \cdot 10^3$ (view in the $x - y$ plane, front view)

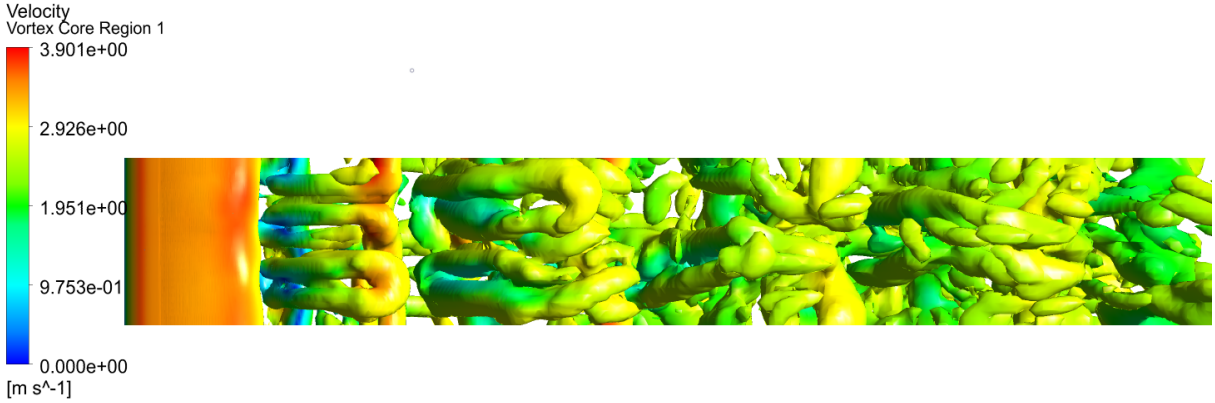

Figure 4.40: Iso-surface plot of $-\lambda_2 = 0.01$ colored using the velocity field for the model with $L_z = \pi D$ at $Re \simeq 6.85 \cdot 10^3$ (view in the $x - z$ plane, top view)

Given the above results, the reliability of this short model can be demonstrated. Furthermore, the computational cost experiences a drastic drop from $\simeq$ 40 hours of running simulation up to $\simeq$ 7 hours (considering $N_T = 15$). Hence, the model having a spanwise length of $L_z = \pi D$ has been clearly adopted for further simulations.

4.7 Comparison between the computational and the experimental results

Finally, the boundary conditions imposed in the simulation has been aligned to the ones used in the experiment described in subsection 4.1.1 with the purpose of comparing the computational and the experimental results.
As discussed in subsection 4.1.1, a VIV experiment was conducted in the wind tunnel of the University of Liège; however, this project is focused on the case of a cylinder undergoing forced motion rather than an aeroelastic cylinder. Hence, in order to have an acceptable comparison with the experimental case, it was decided to impose the motion of the body transverse to the flow at the same wind speed at which the experimental cylinder reached the highest amplitude of vibrations. As mentioned in subsection 4.1.1, the

strongest oscillations were recorded at a wind speed of 4.282 m/s, reaching an amplitude of 0.038 m. Being the cylinder locked, the frequency of vortex shedding no longer follows the Strouhal relation and it takes a value of 7.07 Hz, equal to the frequency of the body's fluctuations. Thus, in the computational model, a forced vibration of the cylinder at a frequency of $f = 7.07$ Hz and an amplitude of $A = 0.038$ m was imposed in combination with a free-stream velocity of 4.282 m/s. Practically, a sinusoidal motion was enforced in ANSYS FLUENT using a `User Defined Function (UDF)`, considering the following equation for the time-varying position of the cylinder along the y-axis:

$$y(t) = A \cdot \sin(2\pi f \cdot t) = 0.038 \cdot \sin(2\pi \cdot 7.07 \cdot t) \tag{4.2}$$

Furthermore, as visible in Figure 4.2, a very low vibration's amplitude characterizes the experimental cylinder's motion at certain wind speed values far from the lock-in region. Being the amplitude close to zero, hence almost no fluctuations are registered, these cases have been simplified by simulating them in ANSYS FLUENT as static cases.

4.7.1 Static cylinder case

Firstly, the simulations of the static cylinder were carried on. One of the points in Figure 4.2 with the lowest amplitude of oscillations ($A \simeq 0.001$ m, 1% of one diameter) corresponds to a free-stream velocity of 2.4823 m/s, which was then imposed as boundary condition at the inlet, leading to a Reynolds number of $1.69 \cdot 10^4$.
For the comparison, the evolution of the mean pressure coefficient along the cylinder's mid-span section, where the pressure taps were positioned in the experimental case, was recorded. Both the experimental and the computational results are available in Figure 4.41 together with two results found by previous researches. In particular, the experimental results from Norberg [49], who analyzed the flow around a static cylinder at $Re = 8 \cdot 10^3$ and low oncoming turbulence level (0.1%), and the ones from Dong et al. [20], who studied a static cylinder at $Re = 10^4$ and low oncoming turbulence level using DNS simulations, are presented in Figure 4.41.

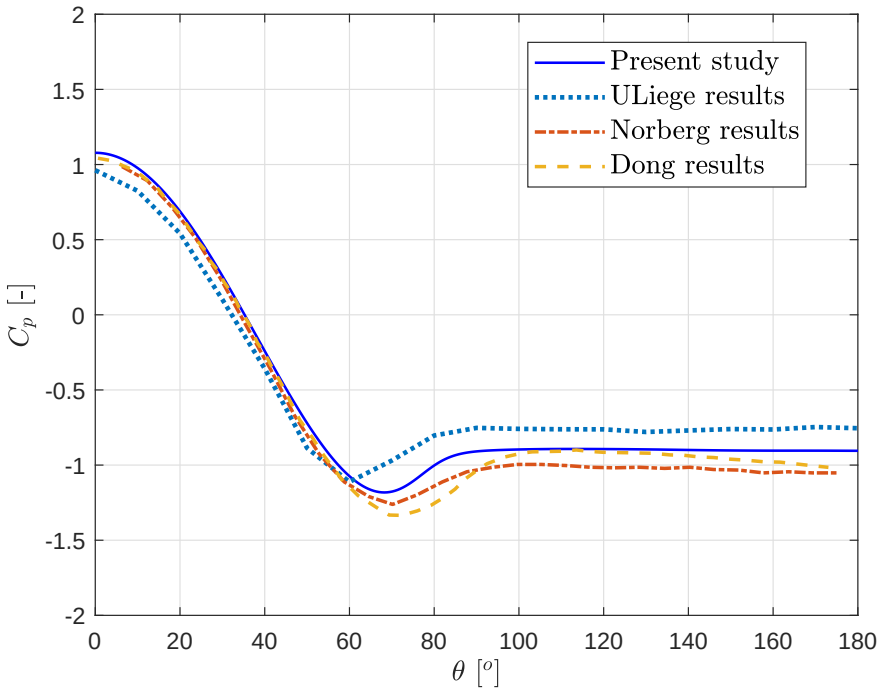

Figure 4.41: Comparison between the C_p evolution vs. θ obtained by different researchers

Some discrepancies are visible in Figure 4.41 when comparing the results from this and previous researches with the ones obtained in the University of Liège. While the formers are very close to each other for $\theta < 60^o$[11], slightly lower values characterizes the latters. Moreover, a difference of $\simeq 10^o$ in the angle of separation is registered, as θ_{sep} is equal to 60^o in the ULiège experimental case, reaching almost 70^o in the other cases.
A non-negligible gap is also observed in the base pressure coefficient value; indeed, while the curve from Dong et al. and the one got in this study approaches $C_{pb} \simeq -0.92$ (afterwards, the former tends to gradually decrease), the two experimental curves follows different behaviors. The results from Norberg records a C_{pb} of -1.05 and the ones from the University of Liège experience an increase in the C_{pb} up to -0.763.

In general, as also explained in the previous sections, a quite satisfying comparison with the results obtained by other researchers is observed, however some non-negligible discrepancies appear when looking at the experimental results from the University of Liège. While the base pressure coefficient value seems slightly changing among the researchers, the angle of separation is always predicted to be very close to 70^o in the Reynolds range of interest. Thus, the drop up to 60^o recorded by the University of Liège results the most unusual observation.
Several reasons could explain these discrepancies; beside the possible presence of bias and/or random errors, neglected during the analysis of the experimental data, a non perfect experimental setup (e.g. non-perfectly rounded and smooth cylinder), and obvious limitations of the computational model in the resolution of real-life flows, one explanation could also be the simplification of the present CFD simulation, where a static rather than an aeroelastic cylinder was considered.

4.7.2 Cylinder with imposed motion

Finally, the sinusoidal motion has been imposed to the vertical coordinate of the cylinder by means of a `User Defined Function`.
For this purpose, the Dynamic Mesh option was adopted in ANSYS FLUENT to ensure the temporal variation of the mesh synchronized with the change in the cylinder's position. In particular, a Diffusion parameter of 2 was imposed in the Dynamic mesh settings; this was done to bias the deformation of cells to the far-field, so that the mesh quality near the body remained unchanged.
The rigid body motion was imposed to the cylinder by enforcing the velocity of the cylinder's center of gravity, while the edges of the domain (inlet, outlet and upper and lower boundary) were set as static. Then, a deforming condition was enforced to the front and back face of the model, as well as to the volume inside the domain. This was necessary to ensure that only the domain's edges remained static during the cylinder's motion.
Moreover, in order to decrease the transient part of the simulation, the static case run at the same wind speed of the moving case was set as initial condition of the simulation. In this way, the vortex shedding mechanism is already stably set when the cylinder starts to move.

Given the good resolution of the mesh and the turbulence model chosen to solve the static cylinder case, the same model was adopted in the forced cylinder case. Furthermore, the non-dimensional time-step was set to 0.05, as in the static case. Indeed, it

[11] It is possible to notice that the slight overestimation of the pressure coefficient at the stagnation point is also predicted by Dong et al. [20].

proved to give good results, reaching the convergence in a maximum of 10 iterations per time-step, which is the value recommended by ANSYS FLUENT User's Guide [3].

After a first test to check the reliability of the model and the simulation set-up in the case of a moving cylinder, the latter was then forced to oscillate following Equation 4.2. It was first checked that the lock-in condition was reached, as expected from the experimental results; hence, the temporal variation of the lift coefficient was analyzed. Indeed, within the lock-in range, as a one-frequency system is created, the unsteady lift coefficient oscillates at a frequency equal to the one of the imposed motion. Moreover, an increase in its amplitude with respect to the static case is expected.
Figure 4.42a and Figure 4.42b displays the time-varying lift coefficient and the amplitude of its Fast Fourier Transform, respectively. It appears clear that the system reached the lock-in condition; indeed, only one main frequency content is visible in Figure 4.42b, equal to the forcing one.

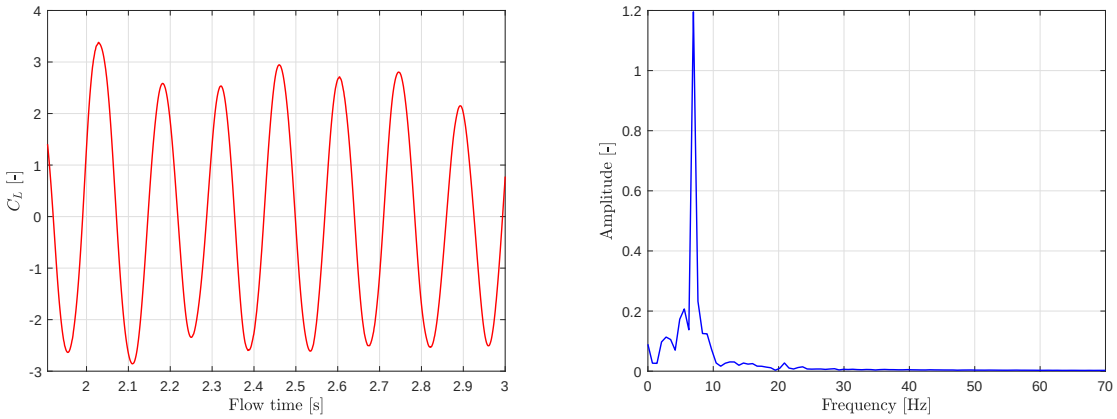

(a) Time-varying lift coefficient (b) FFT amplitude of the lift coefficient

Figure 4.42: Temporal variation of the lift coefficient and its FFT amplitude for the case of an oscillating cylinder at $U_\infty = 4.282$ m/s

Furthermore, as explained in section 1.3, the vortex cores in the wake region assume certain patterns within the lock-in range. Being the frequency of vortex shedding equal to 8.542 Hz at $U_\infty = 4.282$ m/s[12], the ratio between the forcing frequency and the shedding one is $f/f_s = 7.07/8.542 \simeq 0.83$. As shown in Figure 1.11, for the present frequency ratio and non-dimensional vibration's amplitude ($A/D = 0.038/0.1 = 0.38$), this case lies close to the transition from 2S to 2P pattern, hence one of the two modes is expected[13].
The iso-surface plot of the λ_2 criterion confirmed the expectations; Figure 4.43 displays the iso-surface plots at $t = 3$ s, where the 2S pattern is clearly visible.

[12]The vortex shedding frequency has been obtained by simulating the cylinder as static at the free-stream velocity of 4.282 m/s.

[13]In Figure 1.11, the ratio between the imposed and the shedding period is calculated assuming a Strouhal number of exactly 0.2 [56], which could not perfectly describe the real-life flow, hence the transition curve could be slightly shifted.

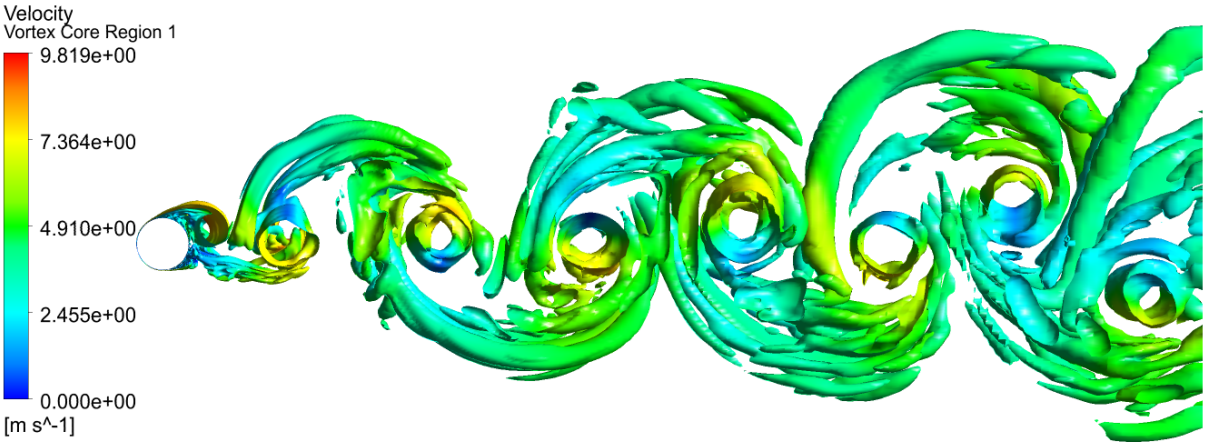

Figure 4.43: Iso-surface plot of $-\lambda_2 = 0.01$ colored using the velocity field at $t = 3$ s and at $Re = 2.9 \cdot 10^4$ (view in the $x - y$ plane, front view)

Finally, the computational mean C_p coefficient has been compared with the experimental results, as Figure 4.44 shows.
An excellent comparison between the two curves is observed up to $\theta = 80^o$. Afterwards, some small differences arise; in particular, a more gradual decay[14] in the pressure coefficient value is seen in the experimental curve. At $\theta = 180^o$, a C_p of $\simeq -2.2$ is registered by the computational model with respect to a smaller value of $\simeq -2.7$ got in the experimental results.

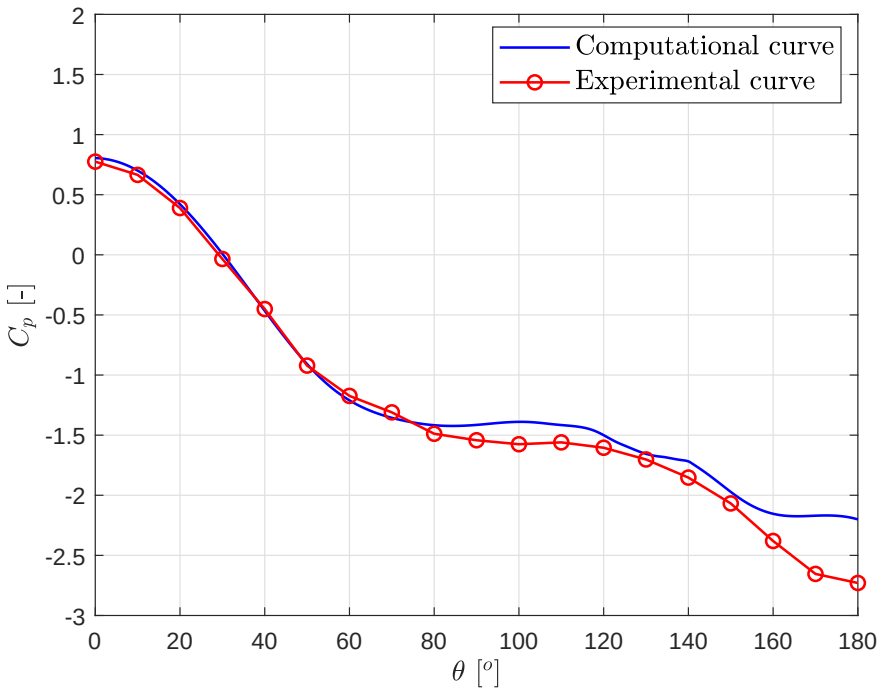

Figure 4.44: Comparison between the computational and the experimental C_p evolution vs. θ for the forced cylinder case at $Re = 2.9 \cdot 10^4$

Eventually, despite some discrepancies with the experimental results, which could be explained by imperfections in the experimental setup, bias and/or random errors in the

[14]The reason for this decay, not observed in the static cylinder case, will be explained in section 5.3.

empirical data and limitations in the numerical model, the computational model presented in this study resulted satisfying and reliable in the resolution of the flow around a 3D circular cylinder (static and oscillating) at high Reynolds numbers. Hence, it has been considered as validated.

4.8 Model characteristics

In this section, a summary of the characteristics of the validated model in combination with the best simulation's settings for this study (i.e. turbulence model and time-step size) is presented in Table 4.7.

Table 4.7: Characteristics of the validated model

Characteristics	**Values**
Cylinder diameter [m]	0.1
Model dimensions [-]	$30D$x$20D$xπD
Height of the first cell [m]	$8.3 \cdot 10^{-5}$
Total number of elements [-]	4264920
Number of elements in the x-direction [-]	380[15]
Number of elements in the y-direction [-]	295[16]
Number of elements in the z-direction [-]	21[17]
Number of nodes around each cylinder's section [-]	576
Turbulence model in use	DES & Transition SST model
Time-step size in use [-]	0.05

[15]This number indicates only the elements in the wake region (the elements occurring from the inlet to the cylinder's left half are neglected).

[16]It accounts only for the elements appearing from the cylinder's section upper point to the domain's upper boundary (the model is symmetric with respect to the x-axis, hence there is the same number of elements in the lower part).

[17]The element size in the z-direction is then equal to $0.15D$.

Chapter 5

Analysis of the unsteady pressure around the cylinder

Once the reliability and the efficiency of the 3D computational model has been proven, the latter can be use to predict the behavior of the flow around the cylinder forced to oscillate at various frequencies and amplitudes. The main purpose of this study is to analyze the evolution of the unsteady pressure around the mid-span section of the cylinder inside and outside the lock-in region. Hence, the time-varying pressure coefficient and lift coefficient have been studied.

The first step is the choice of the combinations between frequency and amplitude of oscillation which would enforce the motion of the body; a certain combination can indeed lead to the lock-in phenomenon, where the vortex shedding frequency equals the frequency of the imposed vibrations.
For this purpose, a free-stream velocity of 4.282 m/s ($Re = 2.9 \cdot 10^4$) and an oncoming turbulence level of 0.2% were assumed, as done in subsection 4.7.2.

5.1 Lock-in region analysis

The desired objective of this step is to possibly recreate the graph presented in Figure 1.10, where the ratio between the imposed frequency and the vortex shedding frequency, as well as the non-dimensional amplitude of oscillations, A/D, clearly defines the region of lock-in, with a shape similar to a V. However, in the present study, due to the 3D nature of the model in use, imposing the motion of the cylinder resulted a very expensive step. The need of a dynamic mesh, required for non-static cases, leads to the necessity of updating the all grid at each time-step, highly increasing the computational cost of the simulation. If, as mentioned in section 4.6, the flow reaching a 3D static cylinder with a spanwise length of $L_z = \pi D$ could be simulated in approximately 7 hours (considering 15 stable periods of vortex shedding), several days are needed to predict the behavior of the flow around an oscillating cylinder. It was indeed estimated that, in the latter case, approximately 6-7 days are necessary to obtain 7-8 stable periods of vortex shedding. The computational time further increases when the frequency and the amplitude of the imposed motion lead the cylinder to be very close to the lock-in region boundaries. Indeed, a difficulty in reaching the convergence of the simulation is encountered, thus the latter would need to be run for several more time-steps to improve the accuracy of the results.
For these reasons, various months would be necessary to recreate the graph in Figure 1.10; in this project, due to lack of time, only few cases could be studied. Thus, a general overview of the behavior of the unsteady pressure around the cylinder is given as an input to possible future specialized studies.

The choice of the combinations between amplitude and frequency of the forced motion was anyway based on the results shown in Figure 1.10. Firstly, the frequency was set to the value tested in subsection 4.7.2, equal to 7.07 Hz; as mentioned in subsection 4.7.2, the ratio between the imposed frequency and the vortex shedding frequency, found simulating the cylinder as static, is 0.83 in this case. At this frequency, two amplitudes were tested, 0.038 m and 0.01 m (38% and 10% of one cylinder's diameter, respectively). These two cases are expected to lie in the lock-in region. Moreover, the body was forced to oscillate at its vortex shedding frequency ($f/f_s = 1$) and at an amplitude of 0.038 m. Afterwards, it was decided to approach the lock-in region boundaries to observe the switch from locked to unlocked cylinder, thus $f = 4.271$ Hz and $f = 15.37$ Hz were enforced. In both cases, the amplitude was kept to 0.038 m, however, as a V shape of the region of lock-in is expected, two different amplitudes were also tested ($A = 0.05$ m & $f = 4.271$ Hz and $A = 0.01$ m & $f = 15.37$ Hz). This was done with the purpose of possibly observing the switch from unlocked to locked cylinder at the same frequencies but at different amplitudes.

A graphical representation of the amplitudes and frequencies enforced in this study is available in Figure 5.1. In particular, as in Figure 1.10, the axes represent the ratio between the imposed frequency and the vortex shedding frequency, as well as the non-dimensional amplitude; the combinations of frequency-amplitude leading to locked or unlocked cylinder are clearly shown.

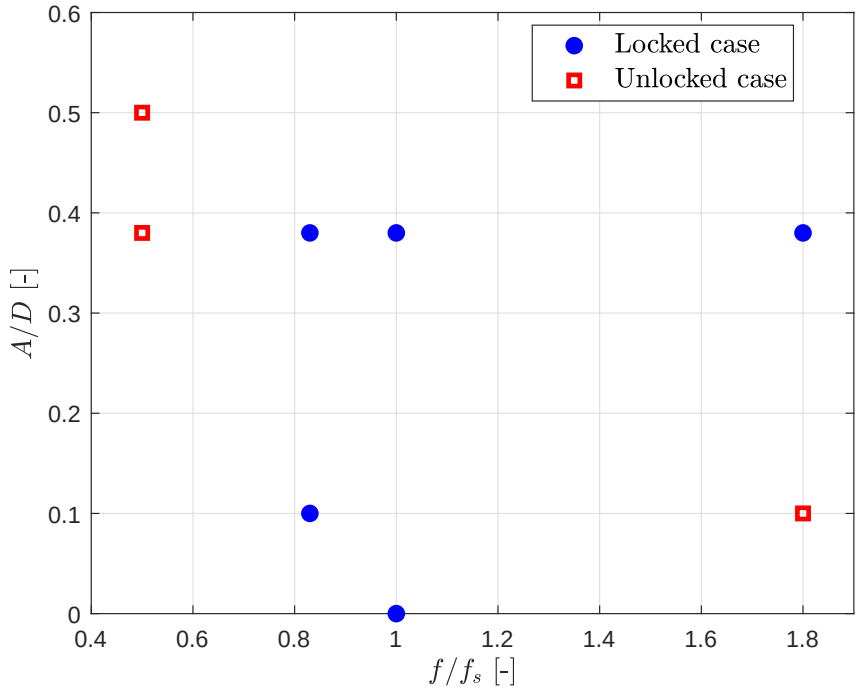

Figure 5.1: Visualization of the lock-in region for the cylinder oscillating transverse to the flow at $Re = 2.9 \cdot 10^4$

Finally, Table 5.1 lists all the cases studied, indicating the behavior of the cylinder (locked or unlocked).

Table 5.1: List of the non-dimensional frequencies and amplitudes imposed to force the cylinder's motion, leading to locked or unlocked conditions

Forced motion		Condition
f/f_s [-]	A/D [-]	
0.5	0.38	Unlocked
0.5	0.5	Unlocked
0.83	0.1	Locked
0.83	0.38	Locked
1	0	Locked
1	0.38	Locked
1.8	0.1	Unlocked
1.8	0.38	Locked

5.1.1 Lift coefficient analysis

As mentioned in subsection 4.7.2, the unsteady lift coefficient is the first key point to evaluate when analyzing the region of lock-in. Indeed, it reflects the possible frequency contents present in the case of study; a one-frequency system characterizes the lock-in region, where the vortex shedding frequency, f_s, and the imposed frequency, f, are equal, while two-frequency contents are expected in the case of unlocked cylinder, both f_s and f. An analysis of the FFT of the time-varying lift coefficient, which, as explained in subsection 1.1.3, should theoretically follow a sinusoidal law with a frequency equal to f_s, would then show the frequency contents of the system.

An example of unsteady lift coefficient in both the time and the frequency domain was already presented in Figure 4.42b; in this section, another example obtained forcing the cylinder to vibrate at $f = 7.07$ Hz and $A = 0.01$ m is shown, as Figure 5.2 displays. Moreover, the time-varying position of the cylinder along the y-direction, $y(t)$[1], is visible in Figure 5.2.
The FFT of the C_L revealed that the cylinder reached the lock-in condition when forced to oscillate at $f = 7.07$ Hz and $A = 0.01$ m, as only one main frequency content is observed, equal to the imposed frequency. Furthermore, as Figure 5.2 displays, as the two curves oscillate at the very close frequencies, an almost constant phase shift between the C_L and $y(t)$ is observed. A phase lag of 93.83^o (C_L lags behind $y(t)$ by 93.83^o) has been calculated by averaging the phase shift obtained considering the time difference between each peak in the C_L and $y(t)$ curve[2].

Even though the lock-in condition is reached, the lift coefficient in Figure 5.2 appears not purely sinusoidal and a small variation in the values of its peaks occurs. Several more vortex shedding periods should be captured to evaluate the evolution of the lift coefficient, which may reach a more stable behavior despite the three-dimensionality of the flow in the wake. Unfortunately, due to lack of time, it was not possible to perform this analysis.

[1]The curve of $y(t)$ has been created using Equation 4.2 at $f = 7.07$ Hz and $A = 0.01$ m.

[2]Due to the high cost of these simulations, only 7 stable vortex shedding periods could be run and, thus, considered in the calculation.

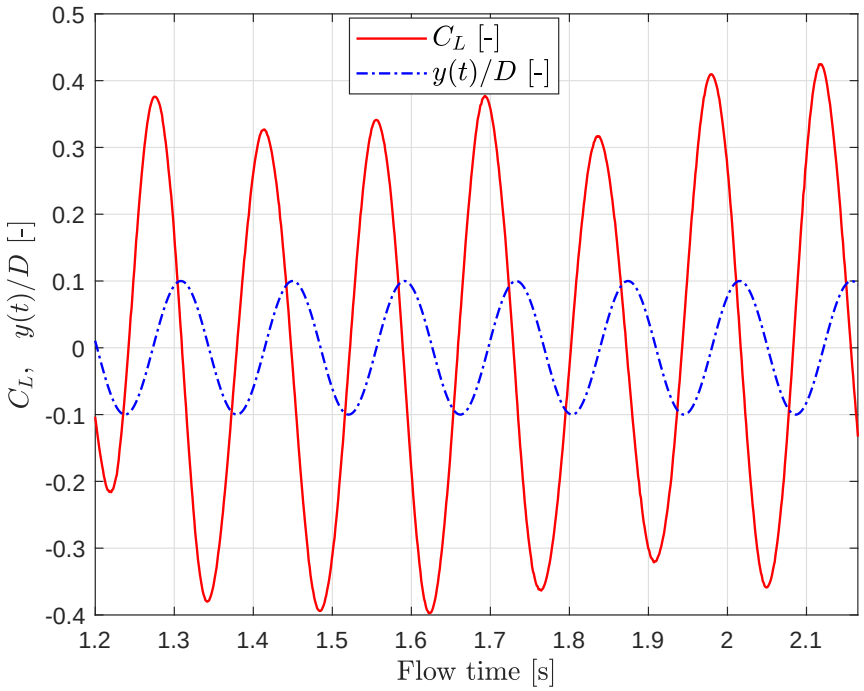

Figure 5.2: Temporal variation of the lift coefficient and of the cylinder's position along the y-axis while forced to oscillate with $f = 7.07$ Hz and $A = 0.01$ m at $Re = 2.9 \cdot 10^4$

As mentioned in section 4.7, an increase in the C_L amplitude occurs with respect to the static case when the cylinder is forced to vibrate. In this study, it was observed that the root-mean-square value of the lift coefficient, as well as the phase shift between C_L and $y(t)$, is dependent on the forcing frequencies and amplitudes, as it is shown in subsection 5.1.2 and subsection 5.1.3. Furthermore, the evolution of the amplitude of the main frequency content in the FFT of the C_L obtained in the tested cases is presented in subsection 5.1.4.

5.1.2 Variation in the root-mean-square amplitude of the lift coefficient

The variation in the $C_{L_{rms}}$ is first analyzed.
Table 5.2 shows the evolution of the $C_{L_{rms}}$ for different frequency ratios but keeping the non-dimensional forcing amplitude equal to $A/D = 0.38$.

Table 5.2: Evolution of the $C_{L_{rms}}$ for different forcing frequencies and non-dimensional amplitude $A/D = 0.38$

f/f_s [-]	$C_{L_{rms}}$ [-]
0.5	0.559
0.83	1.861
1	1.506
1.8	2.672

The $C_{L_{rms}}$ tends to increase for higher frequency ratios, however a small drop is observed from $f/f_s = 0.83$ to $f/f_s = 1$ (-19%); afterwards, its value becomes bigger,

reaching 2.672 at $f/f_s = 1.8$. This value is approximately 5 times bigger than the $C_{L_{rms}}$ got at $f/f_s = 0.5$. Indeed, in the latter case, an unlocked condition was reached; this led to a non-negligible variation in the amplitude of the lift coefficient, as two frequency contents are present. Figure 5.3 shows the time-varying C_L curve and its FFT, where two peaks are visible corresponding to the vortex shedding frequency and to the imposed frequency[3].

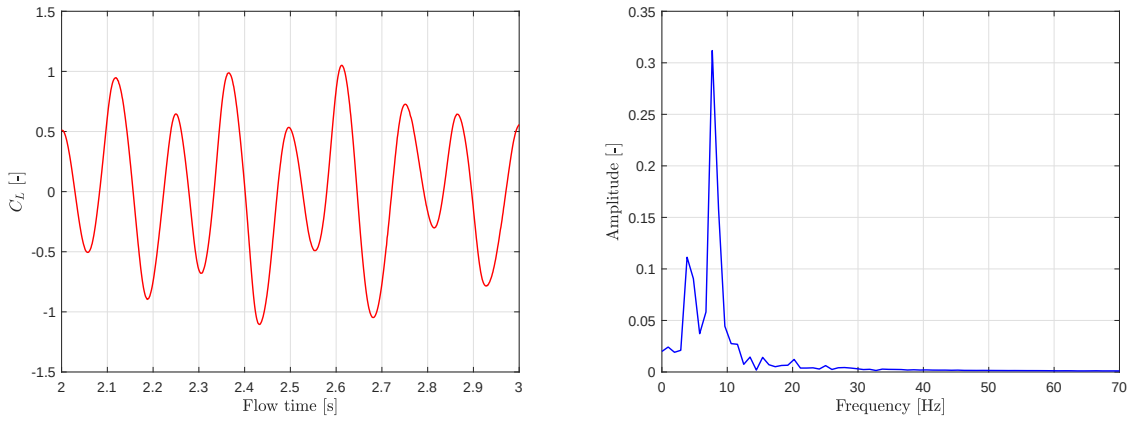

(a) Time-varying lift coefficient

(b) FFT amplitude of the lift coefficient

Figure 5.3: Temporal variation of the lift coefficient and its FFT amplitude for the case of an oscillating cylinder at $f/f_s = 0.5$ and $A/D = 0.38$, at $Re = 2.9 \cdot 10^4$

A variation in the $C_{L_{rms}}$ is also noticed when observing the results from the cases having the same forcing frequency but different amplitudes, as reported in Table 5.3. In general, the root-mean-square of the lift coefficient tends to increase for higher values of the amplitude of the forced oscillations, however, while it increases of only 22% in the case of $f/f_s = 1.8$ when forcing the cylinder at $A/D = 0.1$ and $A/D = 0.38$, a big variation (+86%) occurs at $f/f_s = 0.83$.

The case of $f/f_s = 1.8$ presents one locked condition at $A/D = 0.38$ and one unlocked condition at $A/D = 0.1$, hence it is very close to the right boundary of the lock-in region. Indeed, a difficulty in reaching the convergence of the simulation in the unlocked case was encountered; it was decided to stop the simulation before the convergence was reached to avoid a too expensive computational cost, with the purpose of being able to test other cases. The results are anyway presented for comparison.

Table 5.3: Evolution of the $C_{L_{rms}}$ for cases with the same forcing frequencies and different imposed amplitudes

f/f_s [-]	A/D [-]	$C_{L_{rms}}$ [-]
0.83	0.1	0.255
0.83	0.38	1.861
1.8	0.1	2.08
1.8	0.38	2.672

[3]The resolution of the FFT curve, as well as all the collected results, could be improved by running the simulations for several more time-steps, which was not done due to lack of time.

5.1.3 Variation in the phase shift between C_L and $y(t)$

The phase shift between the unsteady lift coefficient and the time-varying position of the cylinder experiences a variation when forcing the body to oscillate at different frequencies and amplitudes.
Intuitively, due to the presence of two frequency contents in the lift coefficient resulted from an unlocked case, the C_L and $y(t)$ curves do not have the same period, therefore the calculation of the phase shift is senseless. For this reason, only the locked cases are considered in this section.

Table 5.4 shows the evolution of the phase shift (intended as a phase lag of C_L behind $y(t)$) for different frequency ratios and same amplitude of oscillation ($A/D = 0.38$).

Table 5.4: Evolution of the phase lag between C_L and $y(t)$ for cases with different forcing frequencies and same imposed amplitude equal to $A/D = 0.38$

f/f_s [-]	Phase lag [^{o}]
0.83	-58.945
1	-56.877
1.8	-4.112

It is possible to notice from Table 5.4 that the absolute value of the phase lag tends to decrease for higher frequency ratios, becoming almost null when $f/f_s = 1.8$. Indeed, as visible in Figure 5.4, the lift coefficient and the $y(t)$ curves are almost perfectly in phase.

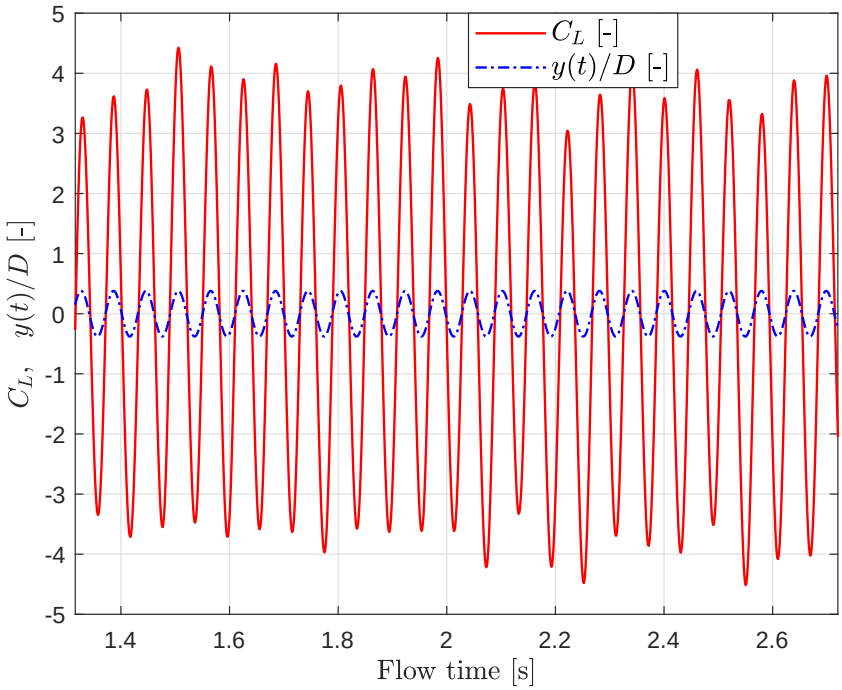

Figure 5.4: Temporal variation of the lift coefficient and of the cylinder's position along the y-axis when forced to oscillate at $f/f_s = 1.8$ and $A/D = 0.38$ at $Re = 2.9 \cdot 10^4$

Furthermore, the variation of the phase lag when forcing the cylinder at the same frequency but different amplitudes ($A/D = 0.38$ and $A/D = 0.1$) is shown in Table 5.5. Increasing the amplitude of vibrations, the phase lag changes sign becoming smaller (C_L first lags behind $y(t)$ and then leads); the C_L is indeed out-of-phase by more than 90^o with respect to $y(t)$ when $A/D = 0.1$. As also shown in the previous section, the variation in the amplitude of oscillation has a big impact on the lift coefficient.

Table 5.5: Evolution of the phase lag between C_L and $y(t)$ for cases with frequency ratio of $f/f_s = 0.83$ and different imposed amplitudes

A/D [-]	Phase lag [^{o}]
0.1	93.831
0.38	-58.945

5.1.4 Variation in the amplitude of the main frequency contents in the FFT of the lift coefficient

Finally, the variation in the amplitude of the main frequency contents in the FFT of the lift coefficient was analyzed in the different cases tested.

Firstly, only the cylinder reaching the lock-in condition was studied, where the main and unique frequency content in the FFT of the lift coefficient corresponds to the imposed frequency, f. As visible in Table 5.6, which shows the evolution of the amplitude of f in the FFT of the lift coefficient for cases with different frequency ratios and same imposed amplitude equal to $A/D = 0.38$, the amplitude of f increases for high values of f/f_s, experiencing a very big growth at $f/f_s = 1.8$, where an amplitude of 1.812 is registered. However, the smallest value occurs at $f/f_s = 1$. The same trend was observed in subsection 5.1.2.

Table 5.6: Evolution of the amplitude of the main frequency content in the FFT of the C_L for cases with different frequency ratios and same imposed amplitude equal to $A/D = 0.38$: locked cases

f/f_s [-]	Amplitude [-]
0.83	1.232
1	1.022
1.8	1.812

Furthermore, Table 5.7 displays the values obtained when keeping the frequency ratio constant to a value of $f/f_s = 0.83$ but varying the amplitude of oscillation, where the increase in A/D leads to an increase in the amplitude of f in the FFT of the C_L.

Table 5.7: Evolution of the amplitude of the main frequency content in the FFT of the C_L for cases with same frequency ratio ($f/f_s = 0.83$) and different imposed amplitudes of oscillation: locked cases

A/D [-]	Amplitude [-]
0.1	0.173
0.38	1.232

On the other hand, in the unlocked cases, two main frequency contents are present in the FFT of the lift coefficient, f_s and f. Table 5.8 shows the variation in the amplitude of both frequency contents in the unlocked cases obtained in this study.
In all the cases in Table 5.8, an higher amplitude of the vortex shedding frequency content is observed with respect to amplitude of the imposed frequency. As expected from the aforementioned results, the amplitude tends to increase for bigger values of f/f_s and A/D. Moreover, the amplitude of f_s and f at $f/f_s = 1.8$ and $A/D = 0.1$ shows two different orders of magnitude; in particular, it experiences a big increase in the vortex shedding frequency with respect to the case of $f/f_s = 0.5$ (+71%), while the imposed frequency reaches only +38%.

Table 5.8: Evolution of the amplitude of the main frequency contents in the FFT of the C_L: unlocked cases

Forced motion		Amplitude [-]	
f/f_s [-]	A/D [-]	Vortex shedding frequency	Imposed frequency
0.5	0.38	0.312	0.111
0.5	0.5	0.36	0.176
1.8	0.1	1.263	0.2827

From the presented results, it is then possible to conclude that an increase in the amplitude and the frequency of the imposed motion causes the growth of the root-mean-square value of the lift coefficient and of the amplitude of the main frequency contents in the FFT of the C_L, except in the case of $f/f_s = 1$, while the phase shift between the unsteady lift coefficient and the temporal variation of the cylinder's position along the y-axis becomes closer to zero, leading the two curves to be in-phase.
However, it must be stated that, due to the small amount of simulations available, these results might change when analyzing different combinations of forcing frequencies and amplitudes of oscillation, which would enrich the graph in Figure 5.1; hence, several more cases should be run to have a better understanding of the behavior of the flow around the cylinder when the lock-in phenomenon is (or is not) encountered.

5.2 Vortex shedding modes

As mentioned in section 1.3, within the lock-in region, the vortex shedding mechanism appears organized in defined patterns, depending on the frequency and on the amplitude of the forced motion.
It has already been shown in Figure 4.43 the presence of a 2S vortex pattern when the cylinder is forced to oscillate at $f/f_s = 0.83$ and $A/D = 0.38$. The same pattern is observed in the case of $f/f_s = 1$ and $A/D = 0.38$, as expected from Figure 1.11.

However, when the cylinder is unlocked, due to the presence of two different frequency contents, no ordered pattern is observed in the wake downstream of the body. Figure 5.5 shows the iso-surface plot of the λ_2 criterion in one unlocked case, where the flow appears organized in the near-wake, becoming more disorganized in the far-wake, where it is difficult to detect a perfectly ordered pattern.

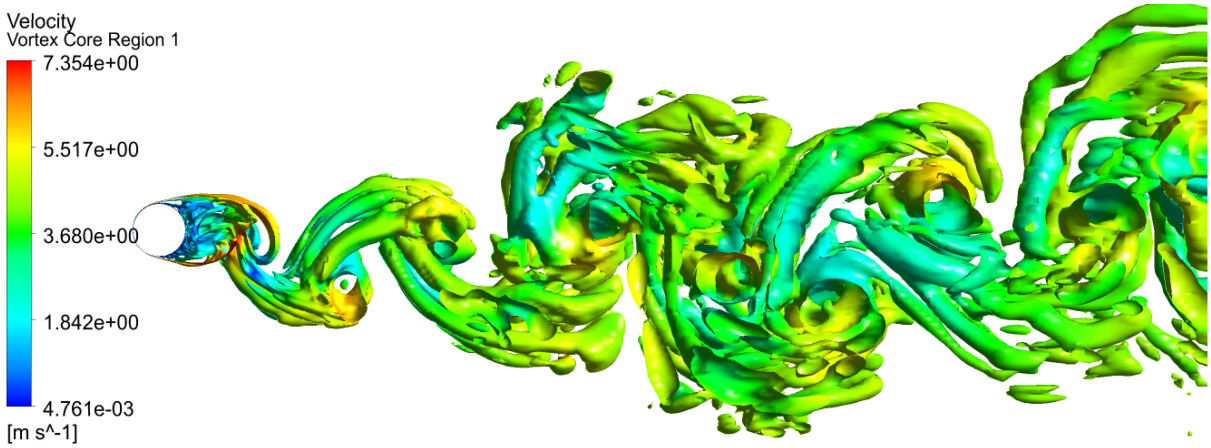

Figure 5.5: Iso-surface plot of $-\lambda_2 = 0.01$ colored using the velocity field when the cylinder is forced to oscillate at $f/f_s = 0.5$ and $A/D = 0.38$, at $Re = 2.9 \cdot 10^4$: unlocked case (view in the $x - y$ plane, front view)

5.3 Analysis of the unsteady pressure around the cylinder

Finally, the evolution of the time-varying pressure around the cylinder was studied. In particular, the pressure coefficient has been recorded at each location around the mid-span section of the cylinder at each time-step, to have an idea of its temporal variation.

As for the lift coefficient, two main frequency contents are expected in the unlocked cylinder cases, while a one-frequency system should characterize the cases lying in the lock-in region. The expectations were satisfied by the obtained results; however, a more accurate analysis of the evolution of the frequency contents around the cylinder's section must be presented.
Subsection 5.3.1 and subsection 5.3.2 discuss the variation in the unsteady pressure coefficient in the cases of locked and unlocked cylinder, respectively.

5.3.1 Locked case

To analyze the behavior of the time-varying pressure coefficient within the lock-in region, the Fast Fourier Transform of the unsteady C_p was first calculated at each location around the mid-span section of the cylinder.
In the first step, it was checked that only one main frequency content (with possible higher harmonics) was present and that it coincided with the frequency of the imposed motion, f. It was noticed that a small variation between f and the main frequency content in the FFT occurs, as the latter reaches a maximum of $+3\%$ with respect to f. This difference seems decreasing when f/f_s approaches higher values, becoming almost null ($+0.1\%$) when $f/f_s = 1.8$. These results are confirmed also by the unlocked cases and, consequentially, by the analysis of the FFT of the lift coefficient. The reason of these small discrepancies can be related to a low resolution of the FFT curves, since few stable vortex shedding periods were considered, as previously mentioned. On the other hand, at higher imposed frequencies, more shedding periods are obviously registered in the same time interval and a better resolution of the FFT curves can be obtained.

The evolution of the amplitude of the main frequency content of the FFT of the pressure coefficient was then analyzed at each location around the cylinder's mid-span section. One example is shown in Figure 5.6, corresponding to $f/f_s = 0.83$ and $A/D = 0.38$.

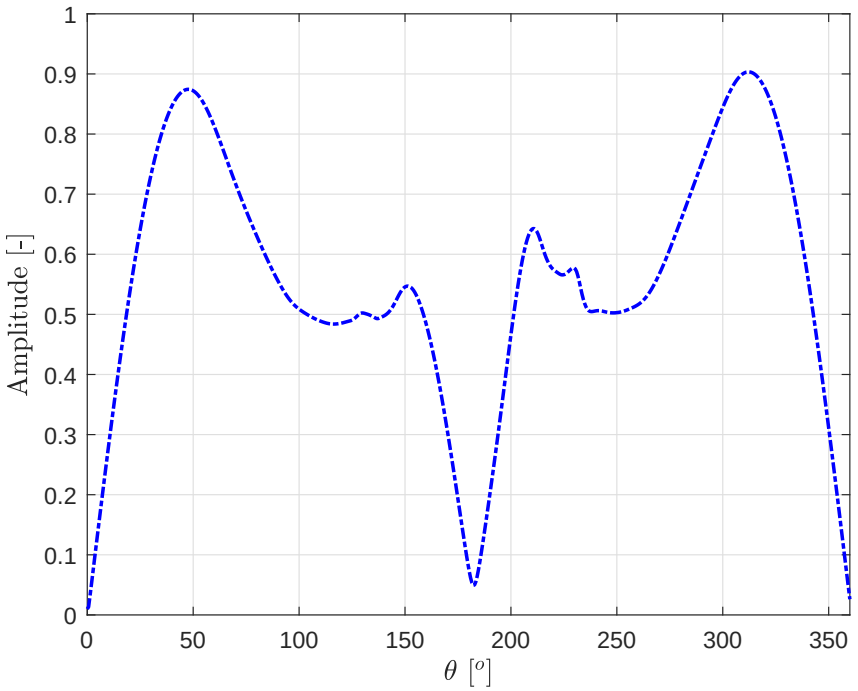

Figure 5.6: Variation in amplitude of the main frequency content ($f = 7.07$ Hz) in the FFT of the C_p at different locations around the mid-span section of the cylinder forced to oscillate at $f/f_s = 0.83$ and $A/D = 0.38$, at $Re = 2.9 \cdot 10^4$

A very low amplitude is recorded at the leading and at the trailing edge of the cylinder's section ($\theta = 0^o$ and $\theta = 180^o$, respectively); these regions are indeed characterized by several frequency contents with very small amplitude and it is not possible to correctly extract the main one. This can be explained by the fact the leading edge corresponds to the stagnation point, at which the flow is then brought to rest, causing the pressure to be equal to the stagnation pressure. On the other hand, the flow at the trailing edge is exactly in the wake center line, a chaotic region where several small frequency contents are observed.
The maximum amplitudes are reached at $\theta \simeq 48^o$ and $\theta \simeq 312^o$, which are very close to the angles of separation in top and in the bottom half of the cylinder's section; then, going inside the wake region, the amplitude gradually decreases becoming almost constant in the ranges $\theta = [113^o, 120^o]$ and $\theta = [235^o, 239^o]$. After small peaks at $\theta \simeq 151^o$ and $\theta \simeq 212^o$, a sharp decrease is observed until reaching small values at the trailing edge.
In general, the overall graph looks close to be symmetric; a correct symmetry might be obtained by running the simulation for more time-steps to get a better resolution of the FFT curves.

Table 5.9 displays the numerical values of the amplitude got at the key points in Figure 5.6.

Table 5.9: Variation in amplitude of the main frequency content ($f = 7.07$ Hz) in the FFT of the C_p at different locations around the mid-span section of the cylinder forced to oscillate at $f/f_s = 0.83$ and $A = 0.38$

Left half		Right half	
θ [^{o}]	Amplitude [-]	θ [^{o}]	Amplitude [-]
0	0.009	113	0.485
48	0.874	120	0.486
90	0.555	160	0.48
270	0.569	180	0.073
312	0.903	235	0.522

Afterwards, when increasing the frequency ratio up to 1, keeping the amplitude of oscillations equal to $A/D = 0.38$, the evolution of the amplitude of the main frequency content in the FFT of the C_p slightly changes, as visible in Figure 5.7.
The general shape of the curves looks very similar, however the increase in the frequency ratio leads to a shift of the correspondent curve to lower amplitudes. Moreover, the locations of the maximum peaks in amplitude is slightly moved when going from $f/f_s = 0.83$ to $f/f_s = 1$ (the two angles have a value of 44^o and 316^o for $f/f_s = 1$). Then, the point lying in the wake with a minimum amplitude goes from 182^o when $f/f_s = 0.83$ to exactly 180^o for $f/f_s = 1$.
The decrease in the amplitude of the frequency content was also observed in subsection 5.1.4, during the analysis of the FFT of the lift coefficient.

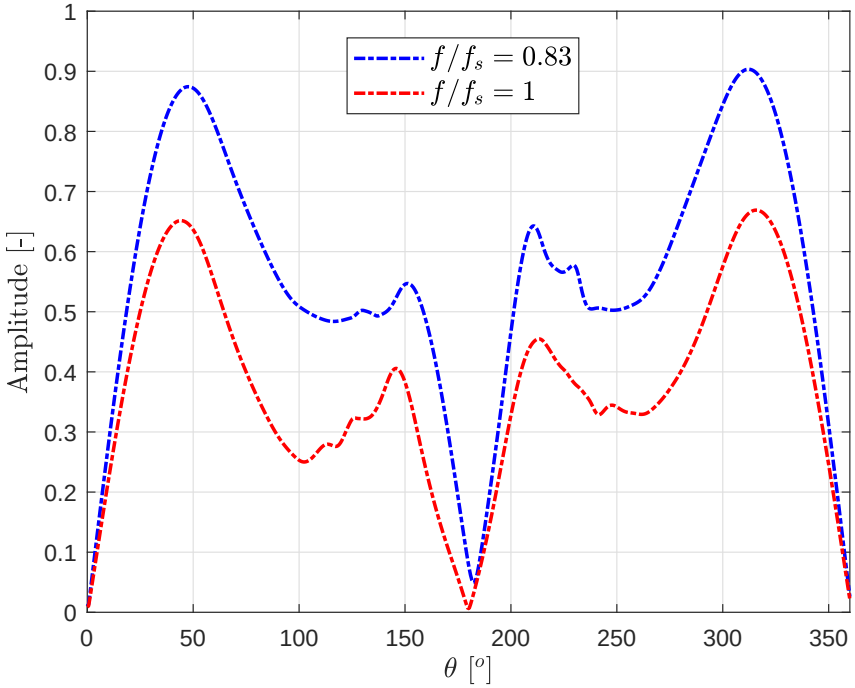

Figure 5.7: Variation in amplitude of the main frequency content in the FFT of the C_p at different locations around the mid-span section of the cylinder forced to oscillate at $f/f_s = 0.83$ and $f/f_s = 1$ and $A/D = 0.38$, at $Re = 2.9 \cdot 10^4$

A different trend is visible in Figure 5.8, which displays the evolution of the amplitude

obtained by forcing the cylinder to oscillate at $f/f_s = 1.8$ and $A/D = 0.38$[4]. Very high amplitudes are reached, especially at $\theta = 45^o$ and $\theta = 316^o$ (1.657 and 1.619, respectively); then, a decay up to 0.06 occurs at $\theta = 180^o$. Hence, the locations of the maximum and minimum amplitude do not change with respect to the case of $f/f_s = 1$.

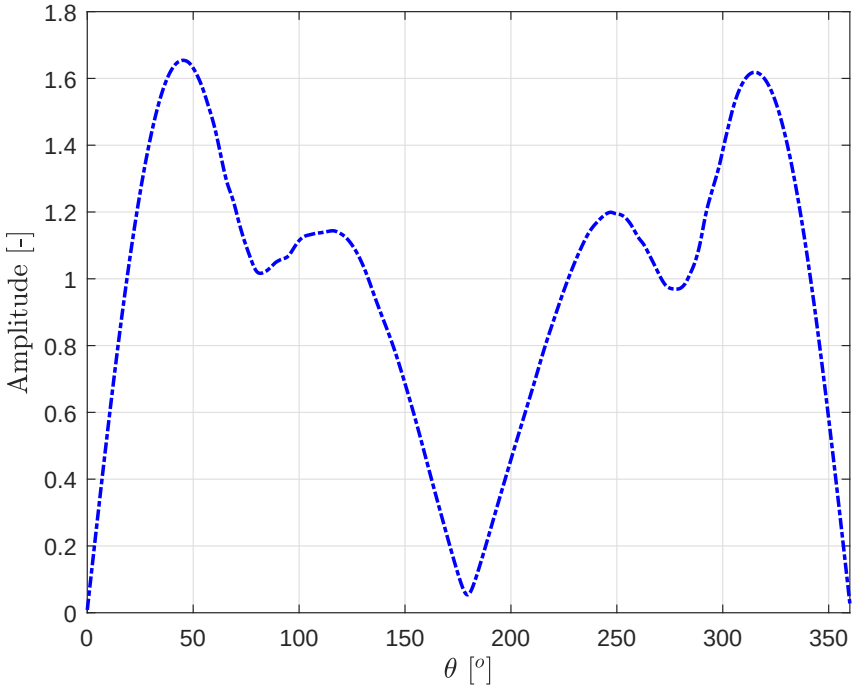

Figure 5.8: Variation in amplitude of the main frequency content in the FFT of the C_p at different locations around the mid-span section of the cylinder forced to oscillate at $f/f_s = 1.8$ and $A/D = 0.38$, at $Re = 2.9 \cdot 10^4$

In all the cases shown, after the maximum amplitude is reached, the latter tends to decay until a certain location, where it increases again before sharply decreasing (the same observation is done in the bottom half of the cylinder, considering that the curve is almost mirrored with respect to the trailing edge location). It was indeed noticed the presence of a small region where the flow tends to recirculate at the same locations of the small decay in amplitude (it separates and then it reattaches). This is obviously due to the oscillations of the cylinder, as recirculation regions appear alternatively at the top and at the bottom of the body depending on the direction of its motion.
In general, this recirculation region seems to be shifted to lower angles in the top half of the cylinder (and to higher ones in its counterpart in the bottom half) when f/f_s increases. Furthermore, this region looks narrower for higher values of the forcing frequency.

An example is visible in Figure 5.9, which shows a zoom of the flow streamlines in the top part of the mid-span cylinder's section ($\theta \simeq [70^o, 120^o]$), when the body is forced to oscillate at $f/f_s = 0.83$ and $A/D = 0.38$. A change in the streamlines direction is observed in Figure 5.9, where the flow results no more attached to the body, causing the drop in the amplitude of the main frequency content in the FFT of the C_p.

[4]The graph is presented in a different figure as, due to its high amplitude, it would not have been possible to accurately see the shape and the values of the curves in Figure 5.7 and Figure 5.8 when inserting them in a single plot.

These regions of separations and reattachments, appearing in the points around the cylinder exposed to the wake, cause not only the small peaks in the amplitude of the main frequency content, but also the variation in the mean pressure coefficient, which, unlike in the static case, tends to decrease towards the trailing edge, as it was shown in Figure 4.44 (the flow separates for the presence of an adverse pressure gradient, hence an increase in pressure moving around the cylinder is registered. Then, the latter drops when the flow reattaches, due to the favorable pressure gradient).

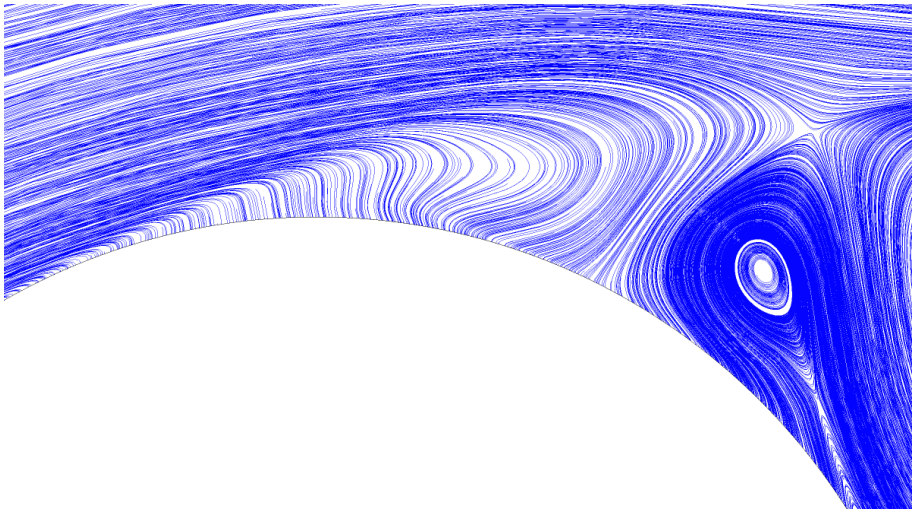

Figure 5.9: Recirculation regions observed when forcing the cylinder to oscillate at $f/f_s = 0.83$ and $A/D = 0.38$, represented by the flow streamlines at $\theta \simeq [70^o, 120^o]$

The evolution in the amplitude of the steady component (at frequency equal to 0 Hz) of the FFT of the pressure coefficient was also analyzed. It is shown in Figure 5.10, where the cases with $f/f_s = 1$ and $f/f_s = 1.8$ combined with $A/D = 0.38$ are presented.
It is possible to notice that the amplitude of the steady part of the FFT is similar to the one observed in the unsteady counterpart when $f/f_s = 1.8$, however, it is one order of magnitude higher in the cases of $f/f_s = 1$. The general behavior follows the one in Figure 5.7 and Figure 5.8; the curve relative to $f/f_s = 1$ is not perfectly symmetrical, while the one relative to $f/f_s = 1.8$ results closer to be symmetrical. Moreover, the main peak in the curve of $f/f_s = 1$ seems to have an opposite trend with respect to the one in the $f/f_s = 1.8$ case. Indeed, if the latter reaches higher steady values close to the $\theta = 180^o$, the former experiences a drop in the steady component at that location.
It is interesting to notice a sharp decay at $\theta \simeq 30^o$ and $\theta \simeq 330^o$ only when $f/f_s = 1$.

In general, all the curves in Figure 5.10 show the tendency of the steady component to become the predominant one when approaching the wake region, where, on the other hand, the unsteady components experience a relevant drop.

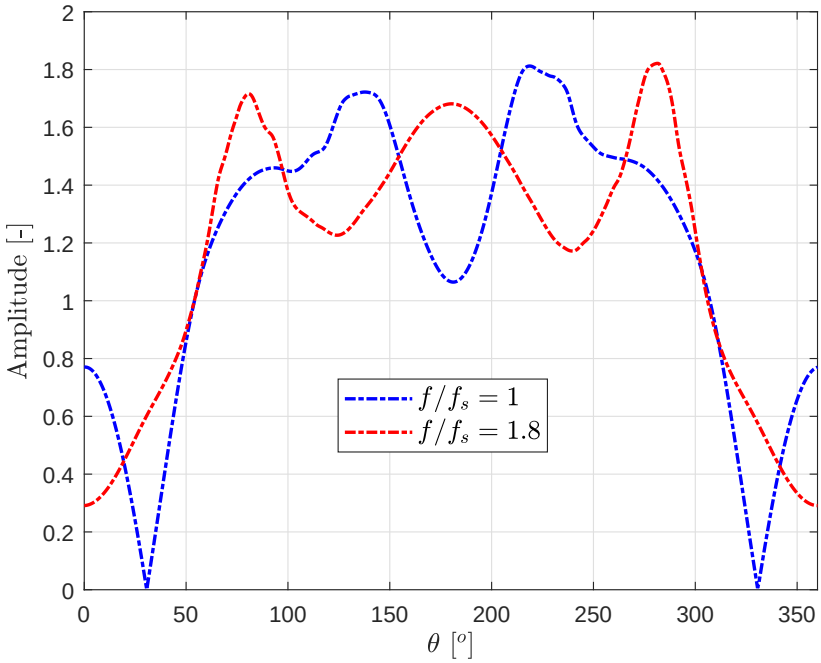

Figure 5.10: Variation in amplitude of the steady component in the FFT of the C_p at different locations around the mid-span section of the cylinder forced to oscillate at $f/f_s = 1$ and $f/f_s = 1.8$ and at $A/D = 0.38$

Furthermore, the variation of the amplitude of the unsteady frequency components with A/D was analyzed. Figure 5.11 displays the evolution of the amplitude of the main frequency content in the FFT of the C_p for two locked cases having $f/f_s = 0.83$ combined with $A/D = 0.1$ and $A/D = 0.38$.

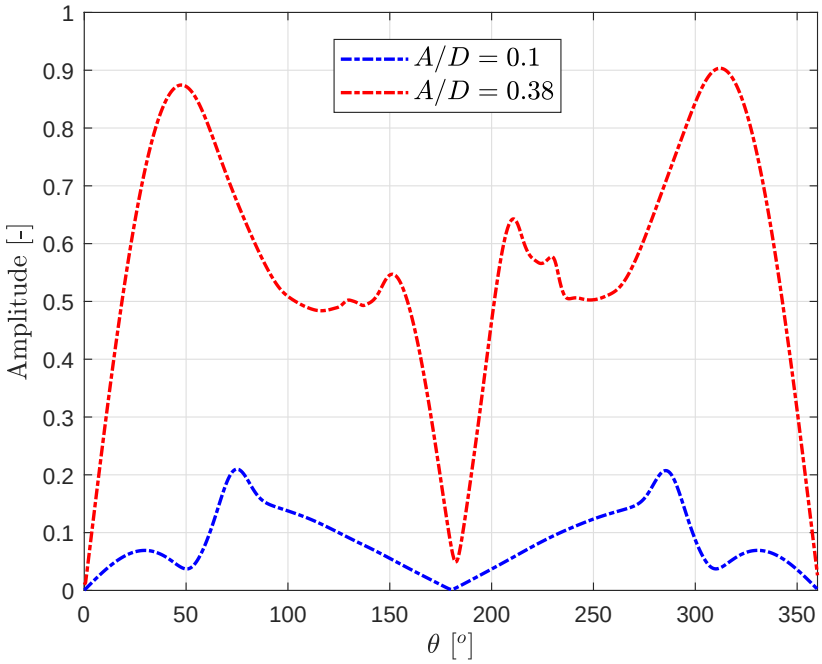

Figure 5.11: Variation in amplitude of the main frequency content ($f_s = 7.07$ Hz) in the FFT of the C_p at different locations around the mid-span section of the cylinder forced to oscillate at $f/f_s = 0.83$ and $A/D = 0.1$ and $A/D = 0.38$

The effect of the decrease in A/D is the decay in the amplitude of the frequency content, thus the curve relative to $A/D = 0.1$ results shifted down with respect to the one of $A/D = 0.38$. Moreover, the maximum amplitude is reached at $\theta = 75.76^o$ and $\theta = 285.5^o$, at the angles of separation of the flow. After the two peaks, the amplitude tends to gradually decrease up to the value of 0.002 at $\theta = 180^o$.
Two smaller peaks in amplitude are recorded at $\theta = 30^o$ and $\theta = 330^o$, not visible in the other curve.

While the cases having $A/D = 0.38$ are not perfectly symmetric, the case with $A/D = 0.1$ seems very close to be symmetric. This might be explained by considering the fact that a smaller amplitude of oscillation leads the cylinder to be closer to the static case, where the regions of flow reattachment are not observed.

Finally, it can be concluded that the variation in f/f_s and in A/D has a non-negligible impact on the evolution of the amplitude of the main frequency content in the FFT of the pressure coefficient at different locations around the mid-span section of the cylinder. In particular, higher amplitudes are registered for greater values of f/f_s and A/D, while the peaks in the amplitude tend to move closer to the cylinder's leading edge.
However, several more simulations should be run to exactly prove the accuracy of the obtained results.

5.3.2 Unlocked case

In the unlocked case, two main frequency contents are expected, the imposed frequency, f, and the vortex shedding frequency, f_s. Thus, the same analysis presented in subsection 5.3.1 was conducted and the evolution of the amplitude of the main frequency contents in the FFT of the pressure coefficient at different locations around the mid-span section of the cylinder was then studied.

Figure 5.12 displays the variation in the amplitude obtained forcing the cylinder's oscillations at $f/f_s = 0.5$ and $A/D = 0.38$, which led the body to be unlocked. Thus, both curves relative to f and f_s are shown.
It is possible to notice from Figure 5.12 that the amplitude of the vortex shedding frequency content follows a trend similar to the one shown in the previous section, reaching its maximum at the angles $\theta = 85.2^o$ and $\theta = 289.3^o$, and gradually decreasing approaching the trailing edge of the cylinder's section. However, no smaller peaks are observed in the curve.

On the other hand, the curve relative to the imposed frequency experiences four main peaks having different amplitudes. Once again, a perfect symmetry of the curve is not reached, which might however be improved by running the simulation for more time-steps. Moreover, it should be checked how close the present case is to the left boundary of the lock-in region.

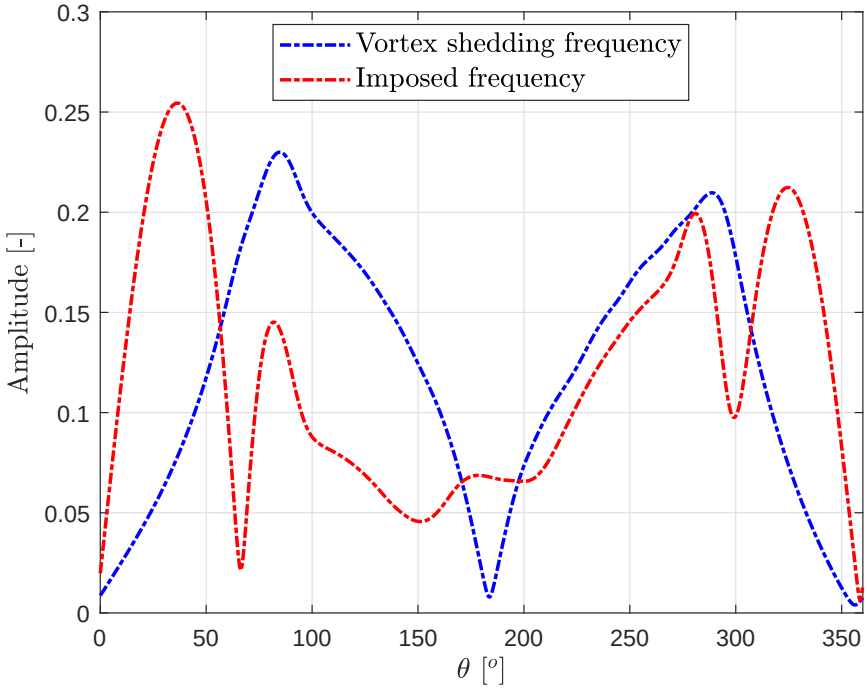

Figure 5.12: Variation in amplitude of the two main frequency contents ($f_s = 8.56$ Hz and $f = 4.271$ Hz) in the FFT of the C_p at different locations around the mid-span section of the cylinder forced to oscillate at $f/f_s = 0.5$ and $A/D = 0.38$, at $Re = 2.9 \cdot 10^4$: unlocked case

Some observations can be made by analyzing the curves in Figure 5.12. Indeed, in the proximity of the leading edge, the imposed frequency results the dominant frequency content, as an high amplitude is rapidly reached. This region is indeed far from the wake, where the frequency of the cylinder's forced oscillations is mostly experienced. After having reached its maximum values at $\theta = 37^o$ and $\theta = 325^o$, a sharp drop in f is observed until $\theta = 66.37^o$ and $\theta = 300^o$, while f_s keeps increasing. The small peaks in f are observed at values close to the peaks in f_s, coincident with the location where the flow separation occurs.
The curves of f and f_s cross each others at two positions, $\theta = 60^o$ and $\theta = 307^o$, where f_s overcomes f becoming the predominant frequency. This is due to the fact that the wake region is approached, where the vortex shedding mechanism, regulated by f_s, is observed. Then, very close to the trailing edge, another intersection of the curves appears and an higher amplitude of f is registered with respect to f_s.

A similar behavior is also observed in Figure 5.13, where the case with the same forcing frequency ($f/f_s = 0.5$) but higher amplitude ($A/D = 0.5$) with respect to the one in Figure 5.12 is presented.

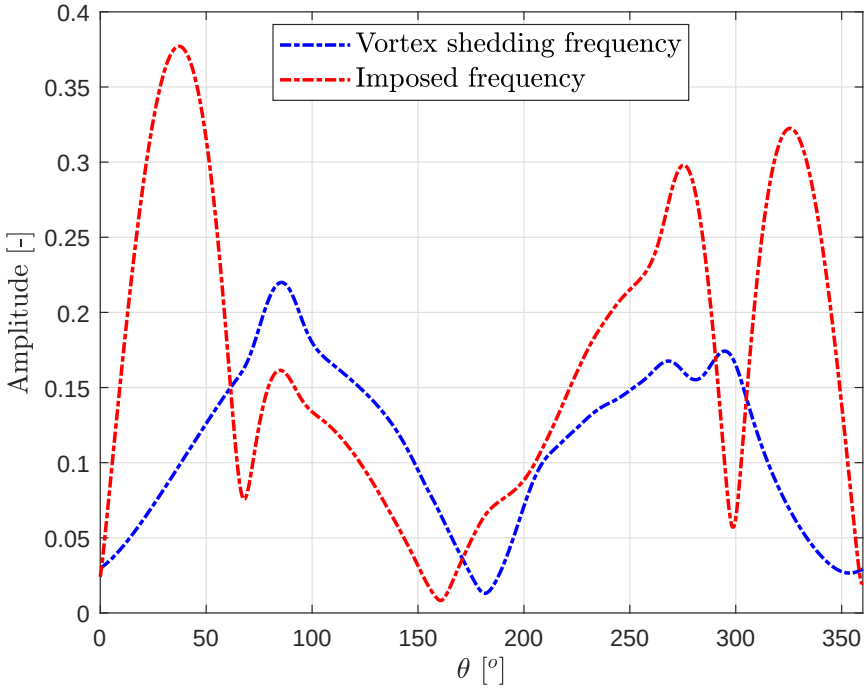

Figure 5.13: Variation in amplitude of the two main frequency contents ($f_s = 8.56$ Hz and $f = 4.271$ Hz) in the FFT of the C_p at different locations around the mid-span section of the cylinder forced to oscillate at $f/f_s = 0.5$ and $A/D = 0.5$, at $Re = 2.9 \cdot 10^4$: unlocked case

While the vortex shedding frequency curve results close to the one in Figure 5.12, despite some small discrepancies, the imposed frequency curve presents higher amplitudes with respect to both the f_s curve and the f curve in Figure 5.12. This is obviously due to the increase in the amplitude of the forced oscillations of the cylinder.
The four peaks in the f curve are again observed, occurring slightly closer to the wake region (a small difference of $\simeq 2\%$ is calculated with respect to the values found inFigure 5.12). However, unlike in Figure 5.12, while, as expected, the forcing frequency content is the predominant one only in the proximity of the leading edge in the top half of the cylinder, becoming less important when approaching the wake region (the switch from f to f_s occurs at $\theta = 61.36^o$), an high predominance of the imposed frequency content is registered in almost all the bottom half of the cylinder. The overall minimum of f is then observed at $\theta = 160.9^o$.
This particular behavior results unclear and a deeper study of the unlocked region should be conducted, especially considering cases far away from the lock-in region boundary, where the worst computational results are registered.

Finally, looking at the spatial evolution of the amplitude of the steady component in the FFT of the pressure coefficient at $f/f_s = 0.5$ combined with $A/D = 0.38$ and $A/D = 0.5$ presented in Figure 5.14, no major differences are encountered when varying A/D. Both curves show an higher amplitude with respect to their unsteady counterparts. Hence, a more steady flow occurs in the wake region downstream of the cylinder.

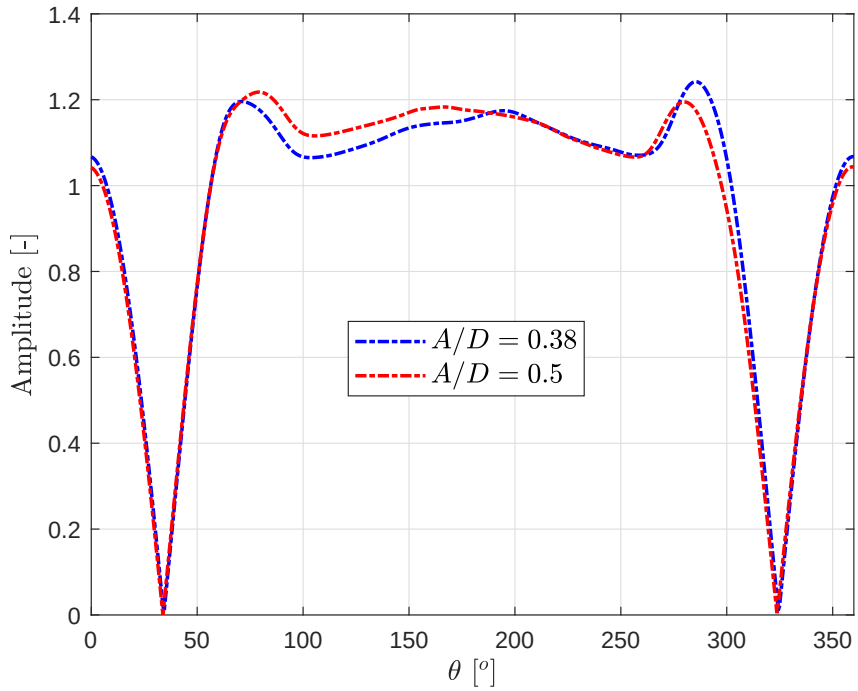

Figure 5.14: Variation in amplitude of the steady component in the FFT of the C_p at different locations around the mid-span section of the cylinder forced to oscillate at $f/f_s = 0.5$ and $A/D = 0.38$ and $A/D = 0.5$, at $Re = 2.9 \cdot 10^4$

It can be then concluded that the variation in the amplitude of the forced oscillations of the cylinder mainly affects the forcing frequency curve. This is an important result showing that the behavior of the unsteady pressure coefficient might be predictable in the unlocked case as the sum of two frequency components, the vortex shedding frequency, which experiences very small variations with A/D, and the imposed frequency, which tends to increase for greater values of A/D. Simulating other similar cases could then prove if there exists a certain proportionality between the amplitude of the forced vibrations and the amplitude of the imposed frequency content in the FFT of the pressure coefficient. In a positive case, this would make the evolution of the unsteady pressure around the cylinder predictable.

Chapter 6

Comparison between 2D and 3D results

This chapter will present the comparison between the computational results obtained in this project with the ones got by Oier Jauntsarats Sacedo [37], who performed the same analysis shown in this thesis by means of a 2D computational model.

In particular, this comparison will focus of the unsteady analysis conducted in chapter 5, hence the evolution of the time-varying lift coefficient and pressure coefficient obtained by the 2D model will be shown with the purpose of understanding how close the 2D and the 3D results are.
The 2D model was run at a Reynolds number of $\simeq 2.9 \cdot 10^4$ ($U_\infty = 4.2786$ m/s) and an incoming turbulence level of 0.2%, while the results were studied among 10 stable periods of vortex shedding [37].

6.1 Comparison of the lock-in region

A better resolution of the lock-in region boundaries was obtained in the 2D results, as it was possible to test several more cases due to the shorter time needed by the 2D simulations to be solved.
Figure 6.1 shows the characterization of the cylinder (locked or unlocked) for different ratios between the forcing frequency and the vortex shedding frequency (labeled f_{osc}/f^0_{vs} in Figure 6.1) and for various non-dimensional amplitudes of the forced vibrations (labeled $|y|/D$ in Figure 6.1), obtained in the 2D case.

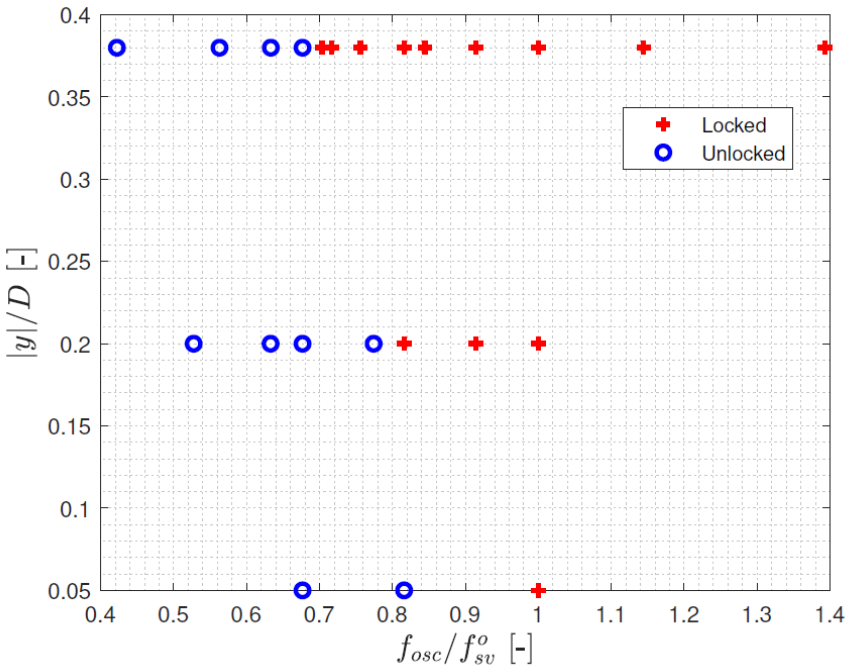

Figure 6.1: Visualization of the lock-in region for the 2D cylinder oscillating transverse to the flow at $Re = 2.9 \cdot 10^4$ [37]

The classical V-shape of the lock-in region is clearly visible; comparing Figure 6.1 with Figure 5.1, it is possible to conclude that both 2D and 3D models reach the lock-in condition at values of the frequency ratio equal to 1 and to 0.83 and a non-dimensional amplitude of 0.38. The 2D cylinder then becomes unlocked when the frequency ratio is equal to 0.82 and the non-dimensional amplitude falls down to 0.05. In the present study, a locked cylinder was observed at $f/f_s = 0.83$ and $A/D = 0.1$, hence a deeper analysis should be conducted to understand at which amplitude of oscillations the cylinder switches to the unlocked condition.
Finally, both cases predict a wider lock-in region for frequency ratios greater than 1 with respect to the counterparts lower than 1.

6.2 Comparison of the unsteady lift coefficient

The comparison of the unsteady lift coefficient obtained by the 2D and the 3D model is done by considering the phase difference between the lift coefficient curve and the sinusoidal curve of the imposed motion described by Equation 4.2, as well as the amplitude of the main frequency content in FFT of the C_L.

Firstly, it was observed the both models were able to accurately capture the nature of the lift coefficient in both the locked and unlocked cases: two main frequency contents are visible in the unlocked case, equal to the forcing frequency and the vortex shedding frequency, while a one-frequency system is created within the lock-in region.

The evolution of the amplitude of the main frequency content obtained in the FFT of the 2D lift coefficient for different frequency ratios (labeled as $|c_L|$) is displayed in Figure 6.2, as well as its phase lag with respect to the cylinder's motion (labeled as ϕ_L). All the results are related to a value of A/D equal to 0.38.

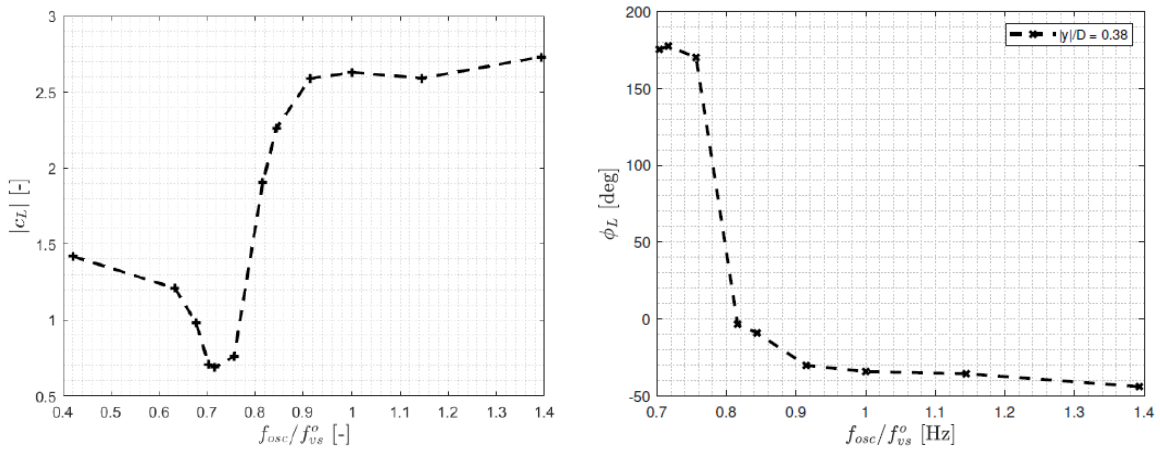

(a) Evolution of $|c_L|$ vs. frequency ratio [37] (b) Evolution of ϕ_L vs. frequency ratio [37]

Figure 6.2: Evolution of the amplitude of the main frequency content in the FFT of the lift coefficient (left) and of the phase difference between the lift coefficient and the imposed motion of the cylinder curve (right) as a function of the imposed frequency and at $A/D = 0.38$ ($Re = 2.9 \cdot 10^4$) [37]

Analyzing Figure 6.2a, it is possible to notice one main difference with the 3D results; while at $f/f_s = 1$ the 3D lift coefficient reaches its minimum value among the locked

cases, as shown in Table 5.6, the 2D lift coefficient seems to display a different trend. However, both models experience a growth in the lift coefficient for higher values of the frequency ratio. In particular, a sharp drop in the amplitude of the vortex shedding frequency content is observed in Figure 6.2a when the cylinder approaches the lock-in region boundary becoming unlocked; the same trend is visible in the 3D case in Table 5.8 for $f/f_s < 1$.

On the other hand, the phase lag in Figure 6.2b seems approaching lower values for greater frequency ratios, highly increasing when approaching the boundary of the lock-in region, very close to a frequency ratio of $\simeq 0.8$. In this region, the phase lag changes sign, becoming positive.
The same trend was observed in subsection 5.1.3, but, as well as in Figure 6.2a, lower absolute numerical values derive from the 3D simulations, which, however, keep the same order to magnitude of their 2D counterparts. Nevertheless, a big difference in the phase lag is observed at $f/f_s > 1$, where the 3D model tends to show an almost null phase lag, which becomes around -40^o in the 2D case.
These discrepancies might be due to a low resolution of the FFT curve in the 3D models and to the impossibility of the 2D cylinder to perfectly model the flow around a real 3D body.

Furthermore, it was noticed that both models led to an increase in the amplitude of the lift coefficient for higher amplitudes of the forced motion close to a frequency ratio of 1, as proven in subsection 5.1.4 and from Figure 6.3.

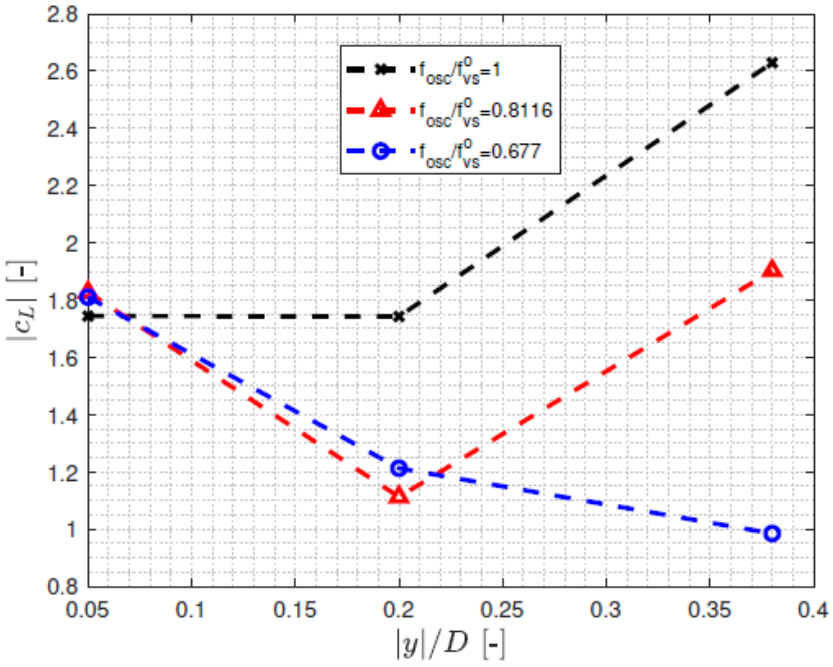

Figure 6.3: Evolution of the amplitude of the main frequency content in the FFT of the 2D lift coefficient as a function of the non-dimensional amplitude of motion and different frequency ratios at $Re = 2.9 \cdot 10^4$ [37]

6.3 Comparison of the unsteady pressure coefficient

Finally, the comparison between the 2D and 3D unsteady pressure coefficient is presented.

Figure 6.4 displays the spatial evolution of the amplitude of the main frequency content in the FFT of the 2D pressure coefficient for a frequency ratio of 1 (labeled f_{osc}/f^0_{vs}) and different imposed amplitudes (labeled $|y|/D$), as well as for a non-dimensional imposed amplitude of 0.38 and two frequency ratios. All the results are related to locked cases.

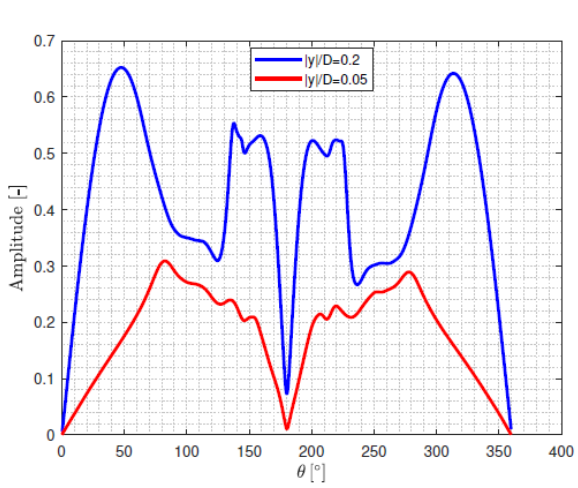

(a) Frequency ratio of 1 [37]

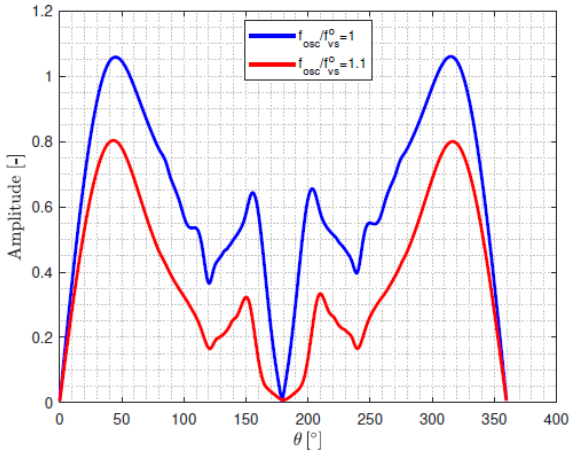

(b) Non-dimensional imposed amplitude of 0.38 [37]

Figure 6.4: Evolution of the amplitude of the main frequency content in the FFT of the 2D pressure coefficient for a frequency ratio of 1 and different imposed amplitudes (left) and for a non-dimensional imposed amplitude of 0.38 and different frequency ratios (right) at $Re = 2.9 \cdot 10^4$ [37]

The above results show a good comparison with the ones obtained in section 5.3; they are all close to be symmetrical and they present the same order of magnitude (slightly lower numerical values characterize the 3D curves). Moreover, the peaks in the 2D and the 3D curves occur at the same locations around the cylinder's section, hence a good resolution of the angles at which the flow separates and reattaches is obtained by both models.

It can be noticed form Figure 6.4a that, like in the 3D case, the increase in the amplitude of the forced oscillations of the cylinder leads to an increase in the amplitude of the main frequency content in the FFT of the pressure coefficient.
On the other hand, as visible in Figure 6.4b, when the amplitude of the forced motion is kept constant and the frequency ratio is increased, the highest values are reached at a frequency ratio of 1. In the latter case, the correspondent 3D results showed an unusual decrease in the amplitude of the curve going from $f/f_s = 0.83$ to $f/f_s = 1$, while a greater curve characterizes the case of $f/f_s = 1.8$. Similar results were also obtained during the lift coefficient analysis.
Due to the lack of 3D simulations in the close neighborhood of $f/f_s = 1$, it is not possible to make any firm conclusion, and the latter case should be probably re-run in order to prove the obtained results, which could have been affected by an undesirable mistake

during the simulation set-up.

Finally, the comparison is made by considering the unlocked cases in Figure 6.5 for the same frequency ratio of 0.667 and two different non-dimensional amplitudes (0.2 and 0.38).
It is shown that vortex shedding frequency (labeled f_{vs}) assumes quite similar curves in both cases, while the increase in the forcing amplitude seems affecting mainly the imposed frequency curve (labeled f_{osc}), which tends to increase with the forcing amplitude. This conclusions recover the ones made in section 5.3 when using the 3D model.
Despite the quite different shape of the forcing frequency curve in the 2D and 3D models (the 2D model captures several more small peaks in the curve), the crossing points between the forcing and the vortex shedding frequency curves occur at very close angles ($\theta \simeq 60^o$ and $\theta \simeq 300^o$).

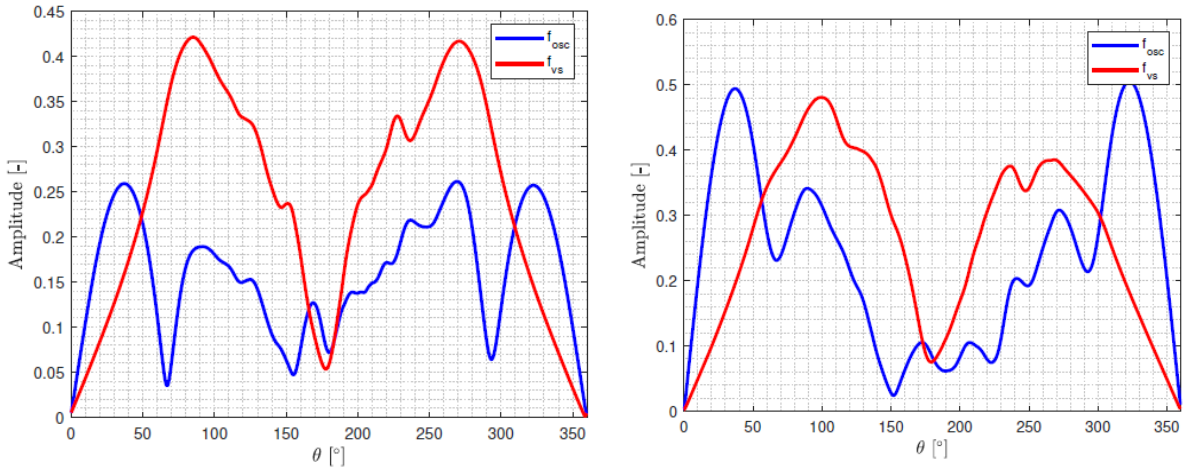

(a) Frequency ratio of 0.667 and non-dimensional amplitude of 0.2 [37]

(b) Frequency ratio of 0.667 and non-dimensional amplitude of 0.38 [37]

Figure 6.5: Evolution of the amplitude of the two main frequency contents (the imposed frequency and the vortex shedding frequency) in the FFT of the 2D pressure coefficient for a frequency ratio of 0.667 and different imposed amplitudes at $Re = 2.9 \cdot 10^4$ [37]

It is then possible to conclude that, despite some discrepancies, mainly related to the numerical values obtained by the two models, the latters both capture quite similar trends in the evolution of the unsteady lift and pressure coefficient for various frequency ratios and amplitude of the cylinder's forced oscillations.
However, a deeper study about the lock-in region boundaries should be conducted, especially in the 3D case, which was lacking of results due to the high cost of the simulations. This would then be able to determine if the 2D model can be used to analyze the evolution of the unsteady pressure around the cylinder or if it consists in a too strong simplification.

Chapter 7
Conclusions

The study conducted in this thesis presented a first approach to evaluate the behavior of the unsteady pressure around a circular cylinder. The main focus was indeed given on understanding how the time-varying pressure coefficient around a cylinder undergoing forced motion changes when the lock-in condition is (or is not) reached.

This project was principally carried out by means of CFD simulations using Ansys Fluent 2019 R2, however, an overview about a possible experimental test rig being designed for use in the Duke University wind tunnel was also presented.

Firstly, the key concepts used in this thesis were introduced in chapter 1, with particular focus on the behavior of the aerodynamic coefficients (lift, drag and pressure coefficients) in the case of a static cylinder, as well as on the vortex shedding mechanism at high Reynolds numbers.
Furthermore, two phenomena were analyzed: the cylinder undergoing aeroelastic and the forced vibrations. The former leads to the well known Vortex Induced Vibrations (or Non-Synchronous Vibration) phenomenon, characterized by an high increase in the amplitude of the cylinder's oscillations within a certain range of free-stream velocities. Hence, the concept of lock-in was introduced in both the aeroelastic and the forced motion case.

Afterwards, in chapter 2, the experimental part of the thesis was presented. It was indeed shown the test rig design created with the purpose of experimentally analyzing the unsteady pressure around a forced and an aeroelastic cylinder. In particular, main focus was first given to the choice of the flow and cylinder parameters (wind tunnel speed, Reynolds number, cylinder's diameter, frequency of the imposed motion) to be considered during the experiments. Then, the test rig design was introduced by considering the supporting structure which holds the cylinder, the transmission system needed in the forced response setup to translate the rotational motion of the motor to a linear motion of the cylinder and the cylinder's design. Moreover, the stepper motor available at Duke University was evaluated basing on its power characteristics, as well as the methods necessary to measure the unsteady pressure around the body.

Finally, the computational part of the thesis, which is also the most extended one, was presented in chapter 3. After a general overview regarding the main CFD concepts, the numerical analysis of the flow investing a circular cylinder was introduced. Firstly, the validation of the computational model was conducted in chapter 4. For this purpose, some experimental results obtained during a VIV experiment in the University of Liège wind tunnel were used as a benchmark to validate the numerical code. Hence, the model of a 3D cylinder was designed in Ansys Workbench to match the experimental cylinder and, consequentially, a diameter of 0.1 m was imposed. The experimental results were also analyzed to set the range of wind speeds and the value of the incoming turbulence level characterizing the simulations. It was found that a Reynolds number lying in the

range $[1.01 \cdot 10^4, 6.2 \cdot 10^4]$ and a turbulence level of 0.2% needed to be enforced. Hence, a fully turbulent flow in the wake region, but with a laminar flow in the boundary layer, is expected.

The validation was then conducted by means of five main steps:

1. Grid quality check
2. Sensitivity analysis of the mesh
3. Choice of the best turbulence model to solve the present case
4. Study of the time-step size to be used
5. Reduction of the spanwise length of the cylinder

They were mostly carried out by simulating a static cylinder at $U_\infty = 1$ m/s ($Re = 6.85 \cdot 10^3$) and 0.2% of incoming turbulence level, and they led to a computational model with the following characteristics (the most reliable model able to accurately solve the flow around and downstream of the cylinder in a reasonable amount of time):

Table 7.1: Characteristics of the validated model

Characteristics	**Values**
Cylinder diameter [m]	0.1
Model dimensions [-]	$30D$x$20D$xπD
Height of the first cell [m]	$8.3 \cdot 10^{-5}$
Total number of elements [-]	4264920
Turbulence model in use	DES & Transition SST model
Time-step size in use [-]	0.05

In particular, the analysis was based on the study of St, $\bar{C}_D$, $C_{L_{rms}}$, θ_{sep} and C_{pb} in comparison with values obtained by other researchers, as well as on correctly capturing the 3D and turbulent nature of the wake region.
Then, the aforementioned model was used to match the experimental data, hence it was run in two conditions: static condition at $U_\infty = 2.4823$ m/s and undergoing forced vibrations with $f = 7.07$ Hz and $A = 0.038$ m at $U_\infty = 4.282$ m/s. The latter case is meant to recreate the strong oscillations observed during the VIV experiment, as the cylinder reached the lock-in condition.

The results showed a good comparison between the mean pressure coefficient curve obtained in the present and in previous researches in the static case, however some discrepancies occurred with respect to the experimental curve. This was justified by the fact that the empirical data do not refer to a perfectly static cylinder, but to a cylinder oscillating at very low amplitude, due to its aeroelastic nature.
On the other hand, a better C_p comparison resulted during the simulation of the cylinder undergoing forced motion, thus the model was considered as validated.

Finally, by means of the validated 3D computational model, the unsteady pressure analysis could be carried out in chapter 5.

The cylinder was forced to oscillate at various frequencies and amplitude with the purpose of reaching the lock-in condition at $Re = 2.9 \cdot 10^4$. Only few simulations could

be run due to their high computational cost; this highly affected the final solution, as firm conclusions could not be made.

Firstly, the unsteady lift coefficient was studied by comparing its $C_{L_{rms}}$ value, its phase lag with respect to the curve of the sinusoidal forced cylinder's motion and the amplitude of the main frequency component in its FFT. The computational model was correctly able to detect the locked or unlocked condition of the cylinder, displaying only one (f_s) or two (f and f_s) main frequency contents in the FFT of the C_L. Moreover, it showed that the lift coefficient (i.e. its rms value and the amplitude of the main frequency contents) has the tendency to increase for higher forcing frequencies and imposed amplitude of the cylinder's oscillations. Only one outlier was found at $f/f_s = 1$, having a slightly smaller lift coefficient with respect to the other cases. This result should then be checked by running more simulations in the lock-in region neighborhood.
On the other hands, the phase lag between $C_L(t)$ and $y(t)/D$ tends to become null for greater frequency ratios and imposed amplitudes.

Furthermore, the spatial variation of the unsteady pressure coefficient around the mid-span section of the cylinder was evaluated by considering the amplitude of the main frequency contents in the FFT of the C_p. It was displayed that the highest values of the vortex shedding frequency content are reached at the separation angles, while the amplitude decreases towards the leading and the trailing edge of the cylinder, at which the minimum values occur. On the other hand, in the unlocked case, the amplitude of the forcing frequency content showed a different trend, being the predominant one close to the cylinder's leading edge. Moreover, the same variations observed during the lift coefficient analysis at different forcing frequencies and amplitudes occurred in the pressure coefficient curves.

The steady component of the FFT of the C_p was also introduced; it is characterized by an higher amplitude with respect to its unsteady counterpart, but it reports no major changes when f/f_s and/or A/D are varied, especially in the unlocked case.

The last step in this project was the comparison with the computational results obtained by the 2D study of Oier Jauntsarats Sacedo [37].

Despite some discrepancies in the numerical values (same order of magnitude, but different values), the 2D and 3D results showed a quite good comparison, as the general trend of the lift and pressure coefficient curves was capture by both models.

Eventually, it must be stated that, due to the low amount of simulations available in chapter 5, this thesis cannot be taken as a benchmark to possible future studies regarding the analysis of the unsteady pressure around a circular cylinder, but it is meant to be used as an input to more specialized works in this field, which could conclude the analysis started in this project.
Not only the computational study could be completed by running more cases with the purpose of accurately predicting the boundaries of the lock-in region and the behavior of the flow inside and outside this area, but also the experimental project presented in chapter 2 could be finalized, comparing the empirical results with the numerical ones. This would then give an accurate and reliable idea about the variation of the unsteady pressure around the cylinder, indicating how well it can be predicted by the 2D and 3D computational models.

Appendix A

MATLAB codes

Code used during the experimental test rig design

Below is the MATLAB code used during the experimental test rig design to calculate all relevant flow parameters based on the minimum number of inputs.

```
clear all
close all
clc

%% NSV project: calculation of the optimum flow parameters

rho = 1.225; % air density [kg/m^3]
ni = 1.5*10^(-5); % kinematic viscosity of air [m^2/s]
D = 0.1016;  % cylinder outer diamater [m] --> PVC Schedule
   40, OD = 4"
L = 0.65;    % length of the cylinder [m]
St = 0.2;    % Strouhal number

% Constraints

U_min = 10;  % minimum wind tunnel flow speed [m/s]
Re_max = 3*10^5; % maximum Reynolds number
f_max = 22.5;  % maximum shedding frequency [Hz]

delta_U = 25;
conv = 0;
U = U_min;
epsilon = 0.96*(L*pi*D^2/4)/((0.508*0.7112)^(3/2));

while U >= U_min && conv == 0

    U = U_min + delta_U;

    U = U*(1 + epsilon);

    Re = U*D/ni;
    f = St*U/D;

    if Re>Re_max || f>f_max

        delta_U = delta_U - 0.5;
```

```
    elseif Re<=Re_max && f<=f_max

        conv = 1;

        U_best = U;

        Re_best = Re;

        f_best = f;

    end

end

dynamic_pressure = 0.5*rho*U_best^2;
```

Code used to study the evolution of the unsteady lift and drag coefficients

```
clear all
close all
clc

%% Study of the lift and drag coefficient

cl = load('lift_coefficient.txt');

cd = load('drag_coefficient.txt');

cl_rms = rms(cl(:,2));

cd_mean = mean(cd(:,2));

figure
plot(cl(:,3),cl(:,2), '-r','LineWidth', 1.01)
hold on
xlabel('Flow time [s]','FontSize', 12, 'Interpreter','latex')
ylabel('$C_L$ [-]','FontSize', 12, 'Interpreter','latex')
grid on

figure
plot(cd(:,3),cd(:,2), '-r','LineWidth', 1.01)
hold on
xlabel('Flow time [s]','FontSize', 12, 'Interpreter','latex')
ylabel('$C_D$ [-]','FontSize', 12, 'Interpreter','latex')
grid on

% FFT of the lift coefficient
```

```
time_step = 0.0011677;  %[s]

Fs = 1/time_step;
N = length(cl(:,2));
df = Fs/N;
freq = 0:df:Fs-df;

FFT = fft(cl(:,2));

figure
plot(freq,abs(FFT/N),'-b','LineWidth', 1.01)
xlabel('Frequency [Hz]', 'FontSize', 12, 'Interpreter','latex
   ')
ylabel('Amplitude [-]','FontSize', 12, 'Interpreter','latex')
grid on
```

Code used to study the evolution of the mean velocity components

```
clear all
close all
clc

%% Validation plots of the mean velocity components

N = 2000;  % number of computational time-steps
D = 0.1;  % cylinder diameter [m]
U_inf = 1;  % free stream velocity [m/s]

file_1 = dir('x_d_1-*');  % data from x/D=1
file_3 = dir('x_d_3-*');  % data from x/D=3
file_wake = dir('wake_center_line-*');  % data from the wake
   center line

for i = 1:N

    data_1 = importdata(file_1(i).name);

    data1_3d(:,:,i) = data_1.data;

    data_3 = importdata(file_3(i).name);

    data3_3d(:,:,i) = data_3.data;

    data_wake = importdata(file_wake(i).name);

    data_wake_3d(:,:,i) = data_wake.data;
```

```
end


for i = 1:N

    y_1(1,:) = data1_3d(:,3,1);
    u_x_1(:,i) = data1_3d(:,6,i);
    u_y_1(:,i) = data1_3d(:,7,i);

    y_3(1,:) = data3_3d(:,3,1);
    u_x_3(:,i) = data3_3d(:,6,i);
    u_y_3(:,i) = data3_3d(:,7,i);

    x_wake(1,:) = data_wake_3d(:,2,1);
    u_x_wake(:,i) = data_wake_3d(:,6,i);

end


figure
plot(y_1./D, mean(u_y_1,2)./U_inf,'-r','LineWidth', 1.1)
xlabel('y/D [-]', 'FontSize', 12, 'Interpreter','latex')
ylabel('$U_y/U_\infty$ [-]','FontSize', 12, 'Interpreter','
   latex')
grid on

figure
plot(y_1./D, mean(u_x_1,2)./U_inf,'-r','LineWidth', 1.1)
xlabel('y/D [-]','FontSize', 12, 'Interpreter','latex')
ylabel('$U_x/U_\infty$ [-]','FontSize', 12, 'Interpreter','
   latex')
grid on

figure
plot(y_3./D, mean(u_y_3,2)./U_inf,'-r','LineWidth', 1.1)
xlabel('y/D [-]', 'FontSize', 12, 'Interpreter','latex')
ylabel('$U_y/U_\infty$ [-]','FontSize', 12, 'Interpreter','
   latex')
grid on

figure
plot(y_3./D, mean(u_x_3,2)./U_inf,'-r','LineWidth', 1.1)
xlabel('y/D [-]','FontSize', 12, 'Interpreter','latex')
ylabel('$U_x/U_\infty$ [-]','FontSize', 12, 'Interpreter','
   latex')
grid on

figure
```

```
plot(x_wake./D, mean(u_x_wake,2)./U_inf,'-r','LineWidth',
   1.1)
xlabel('x/D [-]','FontSize', 12, 'Interpreter','latex')
ylabel('$U_x/U_\infty$ [-]','FontSize', 12, 'Interpreter','
   latex')
grid on
```

Code used to study the evolution of the unsteady pressure coefficient: locked case

```
clear all
close all
clc

%% Cp plot

% Computational Cp

N = 2000;  % number of computational time-steps
rho = 1.225;   % air density [kg/m^3]
U_inf = 4.282;  % free stream velocity [m/s]

file = dir('pressure_mid_span-*');

for i = 1:N

    data = importdata(file(i).name);

    data_3d(:,:,i) = data.data;

end

nodeID = load('nodeID.txt');

cp = zeros(length(nodeID),size(data_3d,3));

for k = 1:length(nodeID)

    for i = 1:size(data_3d,3)

        for j = 1:size(data_3d,1)

            if data_3d(j,1,i) == nodeID(k)

                cp(k,i) = data_3d(j,5,i)./(0.5*rho*U_inf^2);

            end

        end
```

```
    end

end

% Experimental Cp

exp_data = load('datagrid0');

cp_exp = mean(exp_data.data(22).cp,2)';

cp_exp = [flip(cp_exp(1:19)),flip(cp_exp(20:36))];

% Plot for comparison

figure
plot(linspace(0,360,length(nodeID)),mean(cp,2),'-b','
   LineWidth', 1.1)
hold on
plot(0:10:350,cp_exp,'o-r','LineWidth', 1.1)
xlim([0 180])
legend('Computational curve','Experimental curve','FontSize',
    12, 'Interpreter','latex','Location','Best')
xlabel('$\theta$ [$^o$]','FontSize', 12, 'Interpreter','latex
   ')
ylabel('$C_p$ [-]','FontSize', 12,'Interpreter','latex')
grid on


%% FFT of the pressure coefficient

time_step = 0.0011677;  %[s]

Fs = 1/time_step;
df = Fs/N;
freq = 0:df:Fs-df;


for i = 1:length(nodeID)

    FFT(i,:) = fft(cp(i,:));

end

pos = find(abs(FFT(145,2:size(FFT,2)/2))==max(abs(FFT(145,2:
   size(FFT,2)/2))))+1;
f = freq(pos);

for i = 1:length(nodeID)
```

```
    for j = 1:length(freq)

        if freq(j) == f

            amp(i) = abs(FFT(i,j))/N;

        elseif freq(j) == 0

            amp0(i) = abs(FFT(i,j))/N;

        end

    end

end


figure
plot(linspace(0,360,length(nodeID)),amp, '-.b','LineWidth',
   1.1)
xlabel('$\theta$ [$^o$]','FontSize', 12, 'Interpreter','latex
   ')
ylabel('Amplitude [-]','FontSize', 12,'Interpreter','latex')
grid on

figure
plot(linspace(0,360,length(nodeID)),amp0, '-.b','LineWidth',
   1.1)
xlabel('$\theta$ [$^o$]','FontSize', 12, 'Interpreter','latex
   ')
ylabel('Amplitude [-]','FontSize', 12,'Interpreter','latex')
grid on
```

Appendix B

User Defined Function

Below is the `User Defined Function` used to enforce the motion of the cylinder during the simulation set-up in Ansys Fluent 2019 R2.

```
#include "udf.h"


DEFINE_CG_MOTION(cylinder, dt, vel, omega, time, dtime)
{
real A, U, D, pi, w, f;
/*int N_TIME_loc;*/
pi = 3.14159265;


/* Define motion variables */

/* Cylinder diameter [m]*/
D = 0.1;

/* Free-stream velocity [m/s]*/
U = 4.282;

/* Imposed amplitude [m]*/
A = 0.038;

/* Forcing frequency [Hz]*/
f = 7.07;

/* Angular frequency [rad/s]*/
w = 2.0 * pi * f;

/* Angular velocity*/

vel[1] =  A*w*cos(w*time);
}
```

Bibliography

[1] Anagnostopoulos P. and Bearman P.W., *Numerical and Experimental Investigation of vortex-excited oscillations of a circular cylinder*, Proceedings of 4th Conference on Computational Methods and Experimental Measurements, Computational Mechanics Institute, Wessex Institute of Technology, 1989

[2] Andrianne T., *Experimental and Numerical Investigations of the Aeroelastic Stability of Bluff Structures*, PhD dissertation, University of Liège, 2012

[3] Ansys Fluent 2019 R2, *User's Guide*, 2019

[4] Asyikin M.T., *CFD Simulation of Vortex Induced Vibration of a Cylindrical Structure*, Master thesis dissertation, Norwegian University of Science and Technology, Norway, 2012

[5] Beaudan P. and Moin P., *Numerical experiments on the flow past a circular cylinder at sub-critical Reynolds number*, Stanford University, 1994

[6] Berthelsen P.A. and Faltinsen O.M., *A local directional ghost cell approach for incompressible viscous flow problems with irregular boundaries*, Journal of Computational Physic, vol. 227, pp. 4354–4397, 2007

[7] Besem F.M., *Aeroelastic Instabilities due to Unsteady Aerodynamics*, PhD dissertation, Department of Mechanical Engineering and Materials Science, Duke University, 2015

[8] Bishop R.E.D. and Hassan, A.Y., *The lift and drag forces on a circular cylinder in a flowing fluid*, Proceedings Royal Society (London), Series A 277, pp. 32-50, 1964

[9] Blevins R.D., *Flow-Induced Vibration*, Van Nostrand Reinhold, 2nd edn., 1990

[10] Blevins R.D. and Coughran C.S., *Experimental Investigation of Vortex-Induced Vibration in one and two dimension with variable mass, damping, and Reynolds number*, Journal of Fluids Engineering, 2009

[11] Bouris D. and Konstantinidis E., *Bluff Body Aerodynamics and Wake Control*, Department of Mechanical Engineering University of Western Macedonia, 2012

[12] Boussinesq J., *Essai sur la théorie des eaux courantes*, Mémoires présentés par divers savants à l'Académie des Sciences, vol. 23, no. 1, pp. 1-680, 1877

[13] Breuer M., *Large Eddy Simulation of the sub-critical flow past a circular cylinder: numerical and modeling aspects*, International Journal for Numerical Methods in Fluids, vol. 28, pp. 1281-1302, 1998

[14] Carberry B.J., Sheridan J. and Rockwell D., *Controlled oscillations of a cylinder: forces and wake modes*, Journal of Fluids Mechanics, vol. 538, pp. 31–69, 2005

[15] Catalano P., Wang M., Iaccarino G. and Moin P., *Numerical simulation of the flow around a circular cylinder at high Reynolds numbers*, International Journal of Heat and Fluid Flow, vol. 24, pp. 463-469, 2003

[16] Calhoun D., *A Cartesian grid method for solving the two-dimensional stream function-vorticity equations in irregular regions*, Journal of Computational Physic, vol. 176, no. 2, pp. 231-275, 2002

[17] Chell Instruments, *NanoDaq 32 - Sub-Miniature Pressure Scanner*, 2015

[18] D'Agostini Neto A., Lopez J.I.H. and Saltara F., *3D CFD Simulation of Vortex-induced Vibration of Cylinder*, International Journal of Offshore and Polar Engineering, vol. 21, pp. 1-6, 2011

[19] Dervieux, Koobus, Ouvrard, Salvetti and Wornom, *Variational multiscale large-eddy simulations of the flow past a circular cylinder: Reynolds number effects*, Computers & Fluids, vol. 47, no. 2, pp. 44-50, 2011

[20] Dong S. and Karniadakis G.E., *DNS of flow past a stationary and oscillating cylinder at* $Re = 10000$, Division of Applied Mathematics, Center for Fluid Mechanics, Brown University, 2005

[21] Ecklemann, Fay and Konig, *A new Strouhal Reynolds number relationship between the range* $47 < Re < 2 \cdot 10^5$, Physic Fluid, 1998

[22] Egorov Y. and Menter F., *The Scale-Adaptive Simulation Method for Unsteady Turbulent Flow Predictions*, Flow, Turbulence and Combustion, 2010

[23] Fasel H.L. and Linnick M.N., *A high-order immersed interface method for simulating unsteady compressible flows on irregular domains*, Journal of Computational Physic, vol. 204, no. 1, pp. 157-192, 2005

[24] Feng C.C., *The measurements of the vortex induced effects in flow past stationary and oscillating circular and D-section cylinders*, Master Thesis dissertation, The University of British Columbia, 1968

[25] Ferziger J.H. and Peric M., *Computational Methods for Fluid Dynamics*, Springer, Berlin, 1997

[26] Fredsøe J. and Sumer B.M., *Hydrodynamics Around Cylindrical Structure*, World Scientific Publishing, Singapore, 2006

[27] Fujikura Ltd, *Specification Semiconductor Pressure Sensor - Standard Product - APB2 Pressure Sensor*, 2014

[28] Gerrard J.H., *An experimental investigation of the oscillating lift and drag of a circular cylinder shedding turbulent vortices*, Journal of Fluid Mechanics, vol. 11, pp. 244-256, 1961

[29] Gopalkrishnan R., *Vortex-Induced Forces on Oscillating Bluff Cylinders*, PhD dissertation, Massachusetts Institute of Technology, 1993

[30] Griffin O.M. and Skop R.A., *A model for the vortex-excited resonant response of bluff cylinders*, Journal of Sound and Vibration, vol. 27, pp. 395–412, 1973

[31] Grigoriadis D., Kanaris N. and Kassinos S., *Three dimensional flow around a circular cylinder confined in a plane channel*, Department of Mechanical and Manufacturing Engineering, Computational Science Laboratory, University of Cyprus, 2011

[32] Hanson C.E. and Leehey P., *Aeolian tones associated with resonated vibration*, Journal of Sound and Vibration, vol. 13, pp. 465-483, 1971

[33] Hart J., *Comparison of turbulence modeling approaches to the simulation of a dimpled sphere*, Procedia Engineering, vol. 147, pp. 68-73, 2016

[34] Herfjord K., *A study of two-dimensional separated flow by a combination of the finite element method and Navier–Stokes equations*, PhD dissertation, Norwegian Institute of Technology, Norway, 1996

[35] Ibrahim Z., Khan N.B., Nguyen L.T., Javed M.F. and Jameel M., *Numerical investigation of the vortex-induced vibration of an elastically mounted circular cylinder at high Reynolds number ($Re = 10^4$) and low mass ratio using the RANS code*, University of Malaysia, 2017

[36] Incecik A., Wang E. and Xiao Q., *Three-dimensional numerical simulation of two-degree-of-freedom VIV of a circular cylinder with varying natural frequency ratios at* $Re = 500$, Journal of Fluids and Structures, vol. 73, pp. 162-187, 2017

[37] Jauntsarats Sacedo O., *Computational study of the unsteady pressure around a 2D circular cylinder undergoing forced motion*, Master thesis dissertation, Duke University and University of Liège, 2020

[38] Karamanos G.S., Karniadakis G.E. and Ma X., *Dynamic and low-dimensionality of a turbulent near wake*, Journal of Fluid Mechanics, vol. 410, pp. 29-65, 2000

[39] Kefee M.T., *Investigation of the fluctuating forces on a stationary circular cylinder in a subsonic stream and of the associated sound field*, The Journal of the Acoustical Society of America, vol. 34, pp. 1711–1714, 1962

[40] Khalak, A. and Williamson, C.H.K., *Dynamics of a hydroelastic cylinder with very low mass and damping*, Journal of Fluids and Structures, vol. 10, pp. 455-472, 1996

[41] Kravchenko A.G. and Moin P., *Numerical studies of flow over a circular cylinder at* $Re_D = 3900$, Physics of Fluids, vol. 12, no. 2, pp. 403-417, 2000

[42] Mandelli S., *VIV su cilindro: Analisi Sperimentale e Modellazione Numerica*, Master Thesis dissertation, Politecnico di Milano, 2011

[43] Meingast M.B., *Implementation of a Sparse Linear System Solver Utilizing GPU Hardware*, Master Thesis dissertation, Technische Universität Berlin, 2010

[44] Menter F.R., *Two-Equation Eddy-Viscosity Turbulence Models for Engineering Applications*, AIAA Journal, vol. 32, no. 8, pp. 1598-1605, 1994

[45] Moeller M.J., *Measurement of unsteady forces on a circular cylinder in cross flow at subcritical Reynolds numbers*, PhD dissertation, Massachusetts Institute of Technology, 1982

[46] Muggiasca S., *Vibrazioni indotte dal fenomeno di distacco di vortici su corpi cilindrici: dall'analisi sperimentale allo sviluppo di un modello numerico*, PhD dissertation, Politecnico di Milano, 2006

[47] National Instruments, *User Manual NI ISM-7411/7412 Ethernet Integrated Stepper*, 2016

[48] Nguyen V. and Nguyen H.H., *Detached eddy simulations of flow induced vibrations of circular cylinders at high Reynolds numbers*, Journal of Fluids and Structures, vol. 63, pp. 113-119, 2016

[49] Norberg C., *Pressure forces on a circular cylinder in cross flow*, IUTAM Conference on Bluff Bodies Wake Instabilities, Göttingen, 1992

[50] Norberg C., *Fluctuating lift on a circular cylinder: review and new measurements*, Journal of Fluids and Structures, vol. 17, no. 1, pp. 57-96, 2003

[51] Ooi A. and Young M.E., *Comparative assessment of LES and URANS for flow over a cylinder at Reynolds of 3900*, Proceedings of the 16th Australian Fluid Mechanics Conference, Gold Coast, Australia, 2007

[52] Papadonikolaki G. and Stamou A.I., *Modeling the 3-D flow around a cylinder using the SAS Hybrid model*, Global NEST Journal, vol. 16, no. 5, pp. 901-918, 2014

[53] Pope W.H. and Rae A., *Low Speed Wind Tunnel Testing*, 3rd edn., John Wiley & Sons, Ltd, New York, 1999

[54] Reynolds O., *An experimental investigation of the circumstances which determine whether the motion of water shall be direct or sinuous, and of the law of resistance in parallel channels*, Philosophical Transactions of the Royal Society, vol. 174, pp. 935-982, 1883

[55] Roshko A., *On the development of turbulent wakes from vortex streets*, PhD dissertation, California Institute of Technology, 1952

[56] Roshko A. and Williamson C.H.K., *Vortex formation in the wake of an oscillating cylinder*, Journal of Fluids and Structures, vol. 2, no. 4, pp. 355-381, 1988

[57] Russel D. and Wang Z.J., *A Cartesian grid method for modeling multiple moving objects in 2D incompressible viscous flow*, Journal of Computational Physic, vol. 191, no. 1, pp. 177-205, 2003

[58] Srinivasa Mohan L. and Sung-Eun Kim, *Prediction of unsteady loading on a circular cylinder in high Reynolds numbers flows using Large Eddy Simulation*, Proceedings of OMAE 2005, 24th International Conference on Offshore Mechanics and Arctic Engineering, 2005

[59] Strouhal V., *Ueber eine besondere Art der Tonerregung*, Annalen der Physik und Chemie, 3rd edn., vol. 5, no. 10, pp. 215-251, 1878

[60] Techet A., *Lecture notes about Vortex Induced Vibration*, Massachusetts Institute of Technology, 2005

[61] Van Dyke M., *An Album of Fluid Motion*, Stanford, 1982

[62] Wang Z.J. and Xu S., *An immersed interface method for simulating the interaction of a fluid with moving boundaries*, Journal of Computational Physic, vol. 216, no. 2, pp. 454–493, 2006

[63] Williamson C.H.K., *Vortex Dynamics in the Cylinder Wake*, Journal of Fluid Mechanics, vol. 28, pp. 477-539, 1996